MICROSTRUCTURAL EVOLUTION OF CALCIUM DOPED α-Al_2O_3

by

ARZU ALTAY

Submitted to the Graduate School of Engineering and Natural Sciences
in partial fulfillment of
the requirements for the degree of
Master of Science

Sabanci University
July 2002

ABSTRACT

Effects of different calcium doping levels on the microstructure of high purity α-alumina was studied as a function of sintering time and temperature using scanning electron microscope (SEM). Samples were prepared from high purity AKP-500, Sumitomo α-alumina powder that contained maximum 13 ppm total cation impurity initially. Extra pure calcium nitrate tetrahydrate (GR for analysis) were used as the calcium source. Alumina powders with calcium concentrations varying from 0 to 1000 ppm (molar ratio of Ca/Al_2O_3) were dispersed in 2-propanol (analytical reagent) and ball milled for 12 hours with 99.7% pure alumina balls. After drying, powders were pressed first unidirectionally into discs under 28 MPa and then cold isostatically pressed at 250 MPa. Bulk chemical analysis of doped powders were done by ICP-OES. According to ICP results the doped powders contained less than 5 ppm silicon impurity. Sintering of samples were carried out at 1400, 1500 and 1600^0C for 1 and 12 hours. Microstructural evolution under these conditions were related to calcium excess at the grain boundaries (Γ_{Ca}). Γ_{Ca} was calculated using a simplified McLean-Langmuir adsorption model. As expected with increasing sintering time and temperature the average grain size increased. Under all sintering conditions, the grains were uniform in size and equiaxed for low calcium concentrations. The grain morphology became elongated when the calcium concentration at the grain boundaries reached calcium excess of Γ_{Ca}=3-3.5 calcium atoms/nm^2 in all samples. For the samples that were sintered at 1500^0C and 1600^0C, slab like abnormally grown grains appeared between a critical calcium excess concentration of Γ_{Ca}=4.5-8 calcium atoms/nm^2. With abnormally grown grains a dramatic increase in average grain size was observed. However, when the calcium concentration was increased further, above certain calcium excess concentration depending on sintering temperature a significant decrease in grain size was observed. In contrast to samples sintered at 1500^0C and 1600^0C, when the samples sintered at 1400^0C, although the calcium coverage exceeded Γ_{Ca}=11 calcium

atoms/nm^2, only few grains grew abnormally without affecting the average grain size. Observations clearly indicated that calcium atoms cause elongated (slab like) grain morphology when their excess concentrations reach a critical level at the grain boundaries. This is most likely due to the preferential segregation of calcium ions to basal plane in α-alumina as previously shown in literature on alumina with calcium and silicon impurities. In this study, it is indisputably shown that calcium is responsible for the elongated grain morphology observed in polycrystalline alumina. Results obtained in this investigation supported the argument that calcium has an influence on abnormal grain growth (AGG) in α-Al_2O_3. However, it appears that at least one other impurity may be necessary, most likely silicon, to trigger AGG.

ÖZET

Değişik seviyelerdeki kalsiyum katkısının çok saf α-aluminyum oksitin mikroyapısı üzerindeki etkileri sinterleme zamanı ve sıcaklığına bağlı olarak taramalı elektron mikroskopu (SEM) kullanılarak çalışılmıştır. Örnekler başlangıçta maksimum 13 ppm toplam katyon safsızlığı içeren çok saf AKP-500, Sumitomo α-aluminyum oksit tozundan hazırlanmıştır. Kalsiyum kaynağı olarak ekstra saf kalsiyum nitrat tetra-hidrat (GR for analysis) kullanılmıştır. 0 dan 1000 ppm'e kadar değişen kalsiyum konsantrasyonları (Ca/Al_2O_3 mol oranı) içeren aluminyum oksit tozları 2-propil alkol (analytical reagent) içerisinde dağıtılmış ve 12 saat süreyle %99.7 saflıktaki aluminyum oksit toplarıyla öğütülmüşlerdir. Kurutmadan sonra tozlar önce 28 MPa basınç altında tek yönden disk şekline ve daha sonra soğuk eşbasınçlı olarak 250 MPa basıçta sıkıştırılmışlardır. Katkılı tozların kimyasal analizleri ICP-OES yöntemiyle yapılmıştır. ICP sonuçlarına göre katkılı tozlar 5 ppm'den daha az silisyum safsızlığı içermektedirler. Örneklerin sinterlenmesi 1400, 1500 ve 1600^0C'de 1 ve 12 saat süreyle gerçekleştirilmiştir. Bu koşullar altında mikroyapısal gelişim tane sınırlarındaki kalsiyum fazlalığı (Γ_{Ca}) ile ilişkilendirilmiştir. Γ_{Ca} basitleştirilmiş McLean-Langmuir adsorpsyon modeli kullanılarak hesaplanmıştır. Beklendiği üzere sinterleme zamanı ve sıcaklığı arttıkça ortalama tane büyüklükleri de artmıştır. Bütün sinterleme koşulları altında, düşük kalsiyum konsantrasyonlarında taneler homojen büyüklükte ve eş şekillidir. Bütün numunelerde, tane sınırlarındaki kalsiyum fazlalığı Γ_{Ca}=3-3.5 kalsiyum atomları/nm^2'ye ulaştığında tane şekillerinde uzama olmuştur. 1500^0C ve 1600^0C'de sinterlenen numunelerde kritik bir kalsiyum fazlalığı konsantrasyonu Γ_{Ca}=4.5-8 kalsiyum atomları/nm^2 aralığında slab benzeri anormal büyümüş taneler oluşmuştur. Anormal büyüyen tanelerle birlikte ortalama tane büyüklüklerinde belirgin bir artış gözlenmiştir. Fakat, kalsiyum konsantrasyonu arttırılmaya devam ettikçe sinterleme sıcaklığına bağlı olarak, belirli bir kalsiyum fazlalığı konsantrasyonu üzerinde tane büyüklüklerinde farkedilir bir düşüş gözlenmiştir. 1500^0C ve 1600^0C'de sinterlenen

numunelerin aksine 1400^{0}C'de sinterlenen numunelerde kalsiyum dağılımı Γ_{Ca}=11 kalsiyum atomları/nm^2'yi aşmış olmasına rağmen sadece birkaç tane ortalama tane büyüklüğünü değiştirmeden anormal büyümüştür. Gözlemler; tane sınırlarındaki kalsiyum fazlalığı kritik bir seviyeye ulaştığında, bu atomların uzamış (slab benzeri) tane yapısına neden olduğunu açıkça göstermiştir. Bu büyük bir olasılıkla daha öncede kalsiyum ve silisyum katkılı Al_2O_3 ile ilgili literatürde de gösterildiği üzere kalsiyum iyonlarının α-Al_2O_3'in bazal yüzeylerine tercihli ayrışımından kaynaklanmaktadır. Bu çalışmada, kalsiyumun çok kristalli aluminyum oksitte görülen uzamış tane yapısının sorumlusu olduğu kesin olarak gösterilmiştir. Bu araştırmada elde edilen sonuçlar kalsiyumun α-Al_2O_3'deki anormal tane büyümesine (AGG) etkisi olduğu yargısını desteklemektedir. Ancak, anormal tane büyümesini tetikleyecek en az bir başka safsızlığın, büyük bir ihtimalle silisyum, gerekliliği ortaya çıkmıştır.

To Mali...

A beautiful soul has no merit than its existance

Johann Friedrich von Schiller (1759-1805)

ACKNOWLEDGEMENTS

Financial support of this project is provided by TUBITAK as a MISAG research grant numbered MISAG-181.

I wish to express my sincere appreciation to my advisor Dr. Mehmet Ali Gülgün for his continuous support, encouragement and guidance throughout this work. Working with him was the best part of my graduate study at Sabanci University.

I am grateful to BRISA for letting me use their electron microscope facilities and I am thankful to Mr. Alkan for his fruitful scientific collaboration.

I would like to express my special thanks to Fehmiye Gülgün and Fuat Gülgün for being a family to me in Istanbul and making me feel that I am not alone.

I want to acknowledge Nazmiye Zorba for her support throughout my life in Istanbul. She is more than a grandmother to me.

Finally, I want to thank my parents and my brother. By using words, it is impossible to express my love and appreciation to them. Just I want to say I am proud of being a member of such a wonderful family and I cannot even imagine succeeding anything without them.

TABLE OF CONTENTS

1. INTRODUCTION 1
  1.1. A Brief Review of the Crystallography of α-Al_2O_3 1
  1.2. Theory of Sintering 5
    1.2.1. Solid State Sintering 5
  1.3. Grain Growth and Coarsening 8
    1.3.1. Grain Boundary Migration 9
      1.3.1.1. Effect of microstructure and grain boundary chemistry on boundary mobility 10
      1.3.1.2. Impurity Segregation at Grain Boundaries 11
  1.4. Phase Equilibria in CaO-Al_2O_3 System 14
  1.5. Literature Review about the Effects of Various Impurities on the Microstructure of α-Al_2O_3 16
2. EXPERIMENTAL PROCEDURE 25
  2.1. Materials 25
  2.2. Sample Production 28
    2.2.1. Preparation of the Green Bodies 28
    2.2.2. Sintering 29
  2.3. Sample Characterization 30
    2.3.1. Density Measurement 30
    2.3.2. Chemical Analysis 30
    2.3.3. Microstructural Analysis 30
      2.3.3.1. Grain size measurement 32
3. RESULTS & DISCUSSION 33
  3.1. Chemistry 33
  3.2. Densification 34
  3.3. Microstructural Evolution 36

3.3.1. Microstructural Evolution of the Samples Sintered at 1500^0C 42
3.3.2. Microstructural Evolution of the Samples Sintered at 1600^0C 47
3.3.3. Microstructural Evolution of the Samples Sintered at 1400^0C 50
3.3.4. Comparisons of the Microstructural Evolution of the Samples as a Function of Sintering Temperature and Time 53
4. CONCLUSIONS 59

REFERENCES 61

APPENDIX A 64
A.1. Grain Size Measurement 64
A.1a. Average Grain Size Measurement by Mean Linear Intercept Method 64
A.1b. Average Grain Size Measurement of Small and Large Grains 66
A.2. Density Measurement 68
APPENDIX B 70
B.1. Micrographs of the different calcium doped α-Al_2O_3 samples sintered at 1400^0C for 1 hour 70
B.2. Micrographs of the different calcium doped α-Al_2O_3 samples sintered at 1500^0C for 1 hour 73
B.3. Micrographs of the different calcium doped α-Al_2O_3 samples sintered at 1500^0C for 12 hours 76
B.4. Micrographs of the different calcium doped α-Al_2O_3 samples sintered at 1600^0C for 1 hour 79

LIST OF TABLES

Table 1.1. Crystallographic specifications of α-alumina.. 4
Table 1.2. Specifications of the common crystallographic planes in sapphire................ 4
Table 2.1. High purity alumina "AKP-500" (Al_2O_3) analytical data............................. 26
Table 2.2. Calcium nitrate tetrahydrate ($Ca(NO_3)_2.4H_2O$) analytical data.................... 26
Table 2.3. 2-propanol ($CH_3CHOHCH_3$) analytical data.. 27
Table 2.4. Temperature program of sintering.. 29
Table 2.5. Polishing method.. 31
Table 3.1. ICP-OES results of the samples before sintering 33
Table 3.2. Densities of the samples 34
Table 3.3. Average grain sizes.. 37
Table 3.4. Calcium coverage at the grain boundaries.. 41

LIST OF FIGURES

Figure 1.1. The basal plane of sapphire 2

Figure 1.2. The cation sublattice in sapphire 3

Figure 1.3. The two types of unit cell for sapphire 3

Figure 1.4. Common crystallographic planes in sapphire 4

Figure 1.5a. Densification followed by grain growth 6

Figure 1.5b. Coarsening 6

Figure 1.6a. Basic atomic mechanisms that lead to coarsening and change in pore shape 7

Figure 1.6b. Basic atomic mechanisms that lead to densification 7

Figure 1.7. Schematic drawing of two dimensional polycrystalline specimen 10

Figure 1.8. Impurity distribution 12

Figure 1.9. Plot of yttrium grain boundary concentration versus grain size 13

Figure 1.10. Segregation at grain boundaries for different grain boundary densities 14

Figure 1.11. Calculated phase equlibrium diagram of CaO-Al_2O_3 system 15

Figure 3.1. Densification of the samples as a function of sintering temperature 35

Figure 3.2. Undoped α-Al_2O_3 sintered at 1500^0C for 1hour 43

Figure 3.3. 10.8 ppm Ca doped α-Al_2O_3 sintered at 1500^0C for 1 hour 43

Figure 3.4. Undoped α-Al_2O_3 sintered at 1500^0C for 12 hours 44

Figure 3.5. 10.8 ppm Ca doped α-Al_2O_3 sintered at 1500^0C for 12 hours 44

Figure 3.6. 133 ppm Ca doped Al_2O_3 sintered at 1500^0C for 1 hour 45

Figure 3.7. 133 ppm Ca doped Al_2O_3 sintered at 1500^0C for 12 hours 45

Figure 3.8. 344 ppm Ca doped α-Al_2O_3 sintered at 1500^0C for 12 hours 46

Figure 3.9. 650 ppm Ca doped α-Al_2O_3 sintered at 1500^0C for 12 hours 46

Figure 3.10. Undoped α-Al_2O_3 sintered at 1600^0C for 1 hour 48

Figure 3.11. 23 ppm Ca doped α-Al_2O_3 at 1600^0C for 1 hour 48

Figure 3.12. 344 ppm Ca doped α-Al_2O_3 sintered at 1600^0C for 1 hour 49

Figure 3.13. 650 ppm Ca doped α-Al_2O_3 sintered at 1600^0C for 1 hour 49
Figure 3.14. Undoped α-Al_2O_3 sintered at 1400^0C for 1 hour 51
Figure 3.15. 23 ppm Ca doped α-Al_2O_3 sintered at 1400^0C for 1 hour 51
Figure 3.16. 344 ppm Ca doped α-Al_2O_3 sintered at 1400^0C for 1 hour 52
Figure 3.17. 650 ppm Ca doped α-Al_2O_3 sintered at 1400^0C for 1 hour 52
Figure 3.18. Grain size versus Γ_{Ca} 54
Figure A.1a.1. Measurement of the average grain size of 60 ppm Ca doped sample sintered at 1500^0C for 12 hours 65
Figure A.1b.1. Measurement of the average grain sizes of small and large grains in 133 ppm Ca doped sample sintered at 1500^0C for 12 hours 67
Figure B.1.1. a) Undoped α-Al_2O_3 sintered at 1400^0C for 1 hour 70
Figure B.1.1. b) 7.1 ppm Ca doped α-Al_2O_3 sintered at 14000C for 1 hour 70
Figure B.1.2. a) 10.8 ppm Ca doped α-Al_2O_3 sintered at 1400^0C for 1 hour 71
Figure B.1.2. b) 23 ppm Ca doped α-Al_2O_3 sintered at 1400^0C for 1 hour 71
Figure B.1.2. c) 60 ppm Ca doped α-Al_2O_3 sintered at 1400^0C for 1 hour 71
Figure B.1.3. a) 133 ppm Ca doped α-Al_2O_3 sintered at 1400^0C for 1 hour 72
Figure B.1.3. b) 344 ppm Ca doped α-Al_2O_3 sintered at 1400^0C for 1 hour 72
Figure B.1.3. c) 650 ppm Ca doped α-Al_2O_3 sintered at 1400^0C for 1 hour 72
Figure B.2.1. a) Undoped α-Al_2O_3 sintered at 1500^0C for 1 hour 73
Figure B.2.1. b) 7.1 ppm Ca doped α-Al_2O_3 sintered at 1500^0C for 1 hour 73
Figure B.2.1. c) 10.8 ppm Ca doped α-Al_2O_3 sintered at 1500^0C for 1 hour 73
Figure B.2.2. a) 23 ppm Ca doped α-Al_2O_3 sintered at 1500^0C for 1 hour 74
Figure B.2.2. b) 60 ppm Ca doped α-Al_2O_3 sintered at 1500^0C for 1 hour 74
Figure B.2.2. c) 133 ppm Ca doped α-Al_2O_3 sintered at 1500^0C for 1 hour 74
Figure B.2.3. a) 344 ppm Ca doped α-Al_2O_3 sintered at 1500^0C for 1 hour 75
Figure B.2.3. b) 650 ppm Ca doped α-Al_2O_3 sintered at 1500^0C for 1 hour 75
Figure B.3.1. a) Undoped α-Al_2O_3 sintered at 1500^0C for 12 hours 76
Figure B.3.1. b) 7.1 ppm Ca doped α-Al_2O_3 sintered at 1500^0C for 12 hours 76
Figure B.3.1. c) 10.8 ppm Ca doped α-Al_2O_3 sintered at 1500^0C for 12 hours 76
Figure B.3.2. a) 23 ppm Ca doped α-Al_2O_3 sintered at 1500^0C for 12 hours 77
Figure B.3.2. b) 60 ppm Ca doped α-Al_2O_3 sintered at 1500^0C for 12 hours 77
Figure B.3.2. c) 133 ppm Ca doped α-Al_2O_3 sintered at 1500^0C for 12 hours 77

Figure B.3.3. a) 344 ppm Ca doped α-Al_2O_3 sintered at 1500^0C for 12 hours 78

Figure B.3.3. b) 650 ppm Ca doped α-Al_2O_3 sintered at 1500^0C for 12 hours 78

Figure B.4.1. a) Undoped α-Al_2O_3 sintered at 1600^0C for 1 hour.................................. 79

Figure B.4.1. b) 7.1 ppm Ca doped α-Al_2O_3 sintered at 1600^0C for 1 hour................... 79

Figure B.4.1. c) 10.8 ppm Ca doped α-Al_2O_3 sintered at 1600^0C for 1 hour................. 79

Figure B.4.2. a) 23 ppm Ca doped α-Al_2O_3 sintered at 1600^0C for 1 hour.................... 80

Figure B.4.2. b) 60 ppm Ca doped α-Al_2O_3 sintered at 1600^0C for 1 hour.................... 80

Figure B.4.2. c) 133 ppm Ca doped α-Al_2O_3 sintered at 1600^0C for 1 hour.................. 80

Figure B.4.3. a) 344 ppm Ca doped α-Al_2O_3 sintered at 1600^0C for 1 hour.................. 81

Figure B.4.3. b) 650 ppm Ca doped α-Al_2O_3 sintered at 1600^0C for 1 hour................. 81

LIST OF SYMBOLS

T	Temperature
X_t	Total concentration of dopant ion
X_t^*	Bulk solubility limit
S_V	Total grain boundary area
Ω	Volume per cation in α-alumina
D	Mean grain diameter
G	Grain size
C_{GB}	Grain boundary concentration
C_{bulk}	Bulk concentration
K	Partitioning coefficient
ΔG_{seg}	Gibbs free energy change due to segregation
k	Boltzman constant
Γ_c	Critical surface coverage
Γ_o	Planar density of available grain boundary sites for adsorption
Γ_Y	Yttrium excess concentration at the grain boundaries
Γ_{Ca}	Calcium excess concentration at the grain boundaries
Γ_{Si}	Silicon excess concentration at the grain boundaries
$\overline{L}$	Mean linear intercept length
μ	Micron
nm	Nanometer
mm	Millimeter
^0C	Degrees Celsius

LIST OF ABBREVIATIONS

α-Al_2O_3	Alpha alumina
AGG	Abnormal grain growth
YAG	Yttrium alumina garnet
TEM	Transmission electron microscope
STEM	Scanning transmission electron microscope
HRTEM	High resolution transmission electron microscope
AEM	Auger electron microscope
SIMS	Scanning secondary ion mass spectrometry
SEM	Scanning electron microscope
EDS	Energy dispersive spectrometer
ICP-OES	Inductively coupled plasma-optical emission spectroscopy
rpm	Revolution per minute
ppm	Part per million
%TD	Percent theoretical density
wt%	Weight percent

MICROSTRUCTURAL EVOLUTION OF CALCIUM DOPED α-Al_2O_3

by

ARZU ALTAY

Submitted to the Graduate School of Engineering and Natural Sciences
in partial fulfillment of
the requirements for the degree of
Master of Science

Sabanci University
July 2002

ABSTRACT

Effects of different calcium doping levels on the microstructure of high purity α-alumina was studied as a function of sintering time and temperature using scanning electron microscope (SEM). Samples were prepared from high purity AKP-500, Sumitomo α-alumina powder that contained maximum 13 ppm total cation impurity initially. Extra pure calcium nitrate tetrahydrate (GR for analysis) were used as the calcium source. Alumina powders with calcium concentrations varying from 0 to 1000 ppm (molar ratio of Ca/Al_2O_3) were dispersed in 2-propanol (analytical reagent) and ball milled for 12 hours with 99.7% pure alumina balls. After drying, powders were pressed first unidirectionally into discs under 28 MPa and then cold isostatically pressed at 250 MPa. Bulk chemical analysis of doped powders were done by ICP-OES. According to ICP results the doped powders contained less than 5 ppm silicon impurity. Sintering of samples were carried out at 1400, 1500 and 1600^0C for 1 and 12 hours. Microstructural evolution under these conditions were related to calcium excess at the grain boundaries (Γ_{Ca}). Γ_{Ca} was calculated using a simplified McLean-Langmuir adsorption model. As expected with increasing sintering time and temperature the average grain size increased. Under all sintering conditions, the grains were uniform in size and equiaxed for low calcium concentrations. The grain morphology became elongated when the calcium concentration at the grain boundaries reached calcium excess of Γ_{Ca}=3-3.5 calcium atoms/nm^2 in all samples. For the samples that were sintered at 1500^0C and 1600^0C, slab like abnormally grown grains appeared between a critical calcium excess concentration of Γ_{Ca}=4.5-8 calcium atoms/nm^2. With abnormally grown grains a dramatic increase in average grain size was observed. However, when the calcium concentration was increased further, above certain calcium excess concentration depending on sintering temperature a significant decrease in grain size was observed. In contrast to samples sintered at 1500^0C and 1600^0C, when the samples sintered at 1400^0C, although the calcium coverage exceeded Γ_{Ca}=11 calcium

atoms/nm^2, only few grains grew abnormally without affecting the average grain size. Observations clearly indicated that calcium atoms cause elongated (slab like) grain morphology when their excess concentrations reach a critical level at the grain boundaries. This is most likely due to the preferential segregation of calcium ions to basal plane in α-alumina as previously shown in literature on alumina with calcium and silicon impurities. In this study, it is indisputably shown that calcium is responsible for the elongated grain morphology observed in polycrystalline alumina. Results obtained in this investigation supported the argument that calcium has an influence on abnormal grain growth (AGG) in α-Al_2O_3. However, it appears that at least one other impurity may be necessary, most likely silicon, to trigger AGG.

ÖZET

Değişik seviyelerdeki kalsiyum katkısının çok saf α-aluminyum oksitin mikroyapısı üzerindeki etkileri sinterleme zamanı ve sıcaklığına bağlı olarak taramalı elektron mikroskopu (SEM) kullanılarak çalışılmıştır. Örnekler başlangıçta maksimum 13 ppm toplam katyon safsızlığı içeren çok saf AKP-500, Sumitomo α-aluminyum oksit tozundan hazırlanmıştır. Kalsiyum kaynağı olarak ekstra saf kalsiyum nitrat tetra-hidrat (GR for analysis) kullanılmıştır. 0 dan 1000 ppm'e kadar değişen kalsiyum konsantrasyonları (Ca/Al_2O_3 mol oranı) içeren aluminyum oksit tozları 2-propil alkol (analytical reagent) içerisinde dağıtılmış ve 12 saat süreyle %99.7 saflıktaki aluminyum oksit toplarıyla öğütülmüşlerdir. Kurutmadan sonra tozlar önce 28 MPa basınç altında tek yönden disk şekline ve daha sonra soğuk eşbasınçlı olarak 250 MPa basıçta sıkıştırılmışlardır. Katkılı tozların kimyasal analizleri ICP-OES yöntemiyle yapılmıştır. ICP sonuçlarına göre katkılı tozlar 5 ppm'den daha az silisyum safsızlığı içermektedirler. Örneklerin sinterlenmesi 1400, 1500 ve 1600^0C'de 1 ve 12 saat süreyle gerçekleştirilmiştir. Bu koşullar altında mikroyapısal gelişim tane sınırlarındaki kalsiyum fazlalığı (Γ_{Ca}) ile ilişkilendirilmiştir. Γ_{Ca} basitleştirilmiş McLean-Langmuir adsorpsyon modeli kullanılarak hesaplanmıştır. Beklendiği üzere sinterleme zamanı ve sıcaklığı arttıkça ortalama tane büyüklükleri de artmıştır. Bütün sinterleme koşulları altında, düşük kalsiyum konsantrasyonlarında taneler homojen büyüklükte ve eş şekillidir. Bütün numunelerde, tane sınırlarındaki kalsiyum fazlalığı Γ_{Ca}=3-3.5 kalsiyum atomları/nm^2'ye ulaştığında tane şekillerinde uzama olmuştur. 1500^0C ve 1600^0C'de sinterlenen numunelerde kritik bir kalsiyum fazlalığı konsantrasyonu Γ_{Ca}=4.5-8 kalsiyum atomları/nm^2 aralığında slab benzeri anormal büyümüş taneler oluşmuştur. Anormal büyüyen tanelerle birlikte ortalama tane büyüklüklerinde belirgin bir artış gözlenmiştir. Fakat, kalsiyum konsantrasyonu arttırılmaya devam ettikçe sinterleme sıcaklığına bağlı olarak, belirli bir kalsiyum fazlalığı konsantrasyonu üzerinde tane büyüklüklerinde farkedilir bir düşüş gözlenmiştir. 1500^0C ve 1600^0C'de sinterlenen

numunelerin aksine 1400^{0}C'de sinterlenen numunelerde kalsiyum dağılımı Γ_{Ca}=11 kalsiyum atomları/nm^2'yi aşmış olmasına rağmen sadece birkaç tane ortalama tane büyüklüğünü değiştirmeden anormal büyümüştür. Gözlemler; tane sınırlarındaki kalsiyum fazlalığı kritik bir seviyeye ulaştığında, bu atomların uzamış (slab benzeri) tane yapısına neden olduğunu açıkça göstermiştir. Bu büyük bir olasılıkla daha öncede kalsiyum ve silisyum katkılı Al_2O_3 ile ilgili literatürde de gösterildiği üzere kalsiyum iyonlarının α-Al_2O_3'in bazal yüzeylerine tercihli ayrışımından kaynaklanmaktadır. Bu çalışmada, kalsiyumun çok kristalli aluminyum oksitte görülen uzamış tane yapısının sorumlusu olduğu kesin olarak gösterilmiştir. Bu araştırmada elde edilen sonuçlar kalsiyumun α-Al_2O_3'deki anormal tane büyümesine (AGG) etkisi olduğu yargısını desteklemektedir. Ancak, anormal tane büyümesini tetikleyecek en az bir başka safsızlığın, büyük bir ihtimalle silisyum, gerekliliği ortaya çıkmıştır.

To Mali...

A beautiful soul has no merit than its existance

Johann Friedrich von Schiller (1759-1805)

ACKNOWLEDGEMENTS

Financial support of this project is provided by TUBITAK as a MISAG research grant numbered MISAG-181.

I wish to express my sincere appreciation to my advisor Dr. Mehmet Ali Gülgün for his continuous support, encouragement and guidance throughout this work. Working with him was the best part of my graduate study at Sabanci University.

I am grateful to BRISA for letting me use their electron microscope facilities and I am thankful to Mr. Alkan for his fruitful scientific collaboration.

I would like to express my special thanks to Fehmiye Gülgün and Fuat Gülgün for being a family to me in Istanbul and making me feel that I am not alone.

I want to acknowledge Nazmiye Zorba for her support throughout my life in Istanbul. She is more than a grandmother to me.

Finally, I want to thank my parents and my brother. By using words, it is impossible to express my love and appreciation to them. Just I want to say I am proud of being a member of such a wonderful family and I cannot even imagine succeeding anything without them.

TABLE OF CONTENTS

1. INTRODUCTION 1
  1.1. A Brief Review of the Crystallography of α-Al_2O_3 1
  1.2. Theory of Sintering 5
    1.2.1. Solid State Sintering 5
  1.3. Grain Growth and Coarsening 8
    1.3.1. Grain Boundary Migration 9
      1.3.1.1. Effect of microstructure and grain boundary chemistry on boundary mobility 10
      1.3.1.2. Impurity Segregation at Grain Boundaries 11
  1.4. Phase Equilibria in CaO-Al_2O_3 System 14
  1.5. Literature Review about the Effects of Various Impurities on the Microstructure of α-Al_2O_3 16
2. EXPERIMENTAL PROCEDURE 25
  2.1. Materials 25
  2.2. Sample Production 28
    2.2.1. Preparation of the Green Bodies 28
    2.2.2. Sintering 29
  2.3. Sample Characterization 30
    2.3.1. Density Measurement 30
    2.3.2. Chemical Analysis 30
    2.3.3. Microstructural Analysis 30
      2.3.3.1. Grain size measurement 32
3. RESULTS & DISCUSSION 33
  3.1. Chemistry 33
  3.2. Densification 34
  3.3. Microstructural Evolution 36

3.3.1. Microstructural Evolution of the Samples Sintered at 1500^0C 42
3.3.2. Microstructural Evolution of the Samples Sintered at 1600^0C 47
3.3.3. Microstructural Evolution of the Samples Sintered at 1400^0C 50
3.3.4. Comparisons of the Microstructural Evolution of the Samples as a Function of Sintering Temperature and Time 53
4. CONCLUSIONS 59

REFERENCES 61

APPENDIX A.. 64
A.1. Grain Size Measurement 64
A.1a. Average Grain Size Measurement by Mean Linear Intercept Method........... 64
A.1b. Average Grain Size Measurement of Small and Large Grains 66
A.2. Density Measurement 68
APPENDIX B 70
B.1. Micrographs of the different calcium doped α-Al_2O_3 samples sintered at 1400^0C for 1 hour 70
B.2. Micrographs of the different calcium doped α-Al_2O_3 samples sintered at 1500^0C for 1 hour 73
B.3. Micrographs of the different calcium doped α-Al_2O_3 samples sintered at 1500^0C for 12 hours 76
B.4. Micrographs of the different calcium doped α-Al_2O_3 samples sintered at 1600^0C for 1 hour 79

LIST OF TABLES

Table 1.1. Crystallographic specifications of α-alumina.... 4
Table 1.2. Specifications of the common crystallographic planes in sapphire.... 4
Table 2.1. High purity alumina "AKP-500" (Al_2O_3) analytical data.... 26
Table 2.2. Calcium nitrate tetrahydrate ($Ca(NO_3)_2.4H_2O$) analytical data.... 26
Table 2.3. 2-propanol ($CH_3CHOHCH_3$) analytical data.... 27
Table 2.4. Temperature program of sintering.... 29
Table 2.5. Polishing method.... 31
Table 3.1. ICP-OES results of the samples before sintering.... 33
Table 3.2. Densities of the samples.... 34
Table 3.3. Average grain sizes.... 37
Table 3.4. Calcium coverage at the grain boundaries.... 41

LIST OF FIGURES

Figure 1.1. The basal plane of sapphire ... 2
Figure 1.2. The cation sublattice in sapphire ... 3
Figure 1.3. The two types of unit cell for sapphire ... 3
Figure 1.4. Common crystallographic planes in sapphire ... 4
Figure 1.5a. Densification followed by grain growth ... 6
Figure 1.5b. Coarsening ... 6
Figure 1.6a. Basic atomic mechanisms that lead to coarsening and change in pore shape ... 7
Figure 1.6b. Basic atomic mechanisms that lead to densification ... 7
Figure 1.7. Schematic drawing of two dimensional polycrystalline specimen ... 10
Figure 1.8. Impurity distribution ... 12
Figure 1.9. Plot of yttrium grain boundary concentration versus grain size ... 13
Figure 1.10. Segregation at grain boundaries for different grain boundary densities ... 14
Figure 1.11. Calculated phase equlibrium diagram of CaO-Al_2O_3 system ... 15
Figure 3.1. Densification of the samples as a function of sintering temperature ... 35
Figure 3.2. Undoped α-Al_2O_3 sintered at 1500^0C for 1hour ... 43
Figure 3.3. 10.8 ppm Ca doped α-Al_2O_3 sintered at 1500^0C for 1 hour ... 43
Figure 3.4. Undoped α-Al_2O_3 sintered at 1500^0C for 12 hours ... 44
Figure 3.5. 10.8 ppm Ca doped α-Al_2O_3 sintered at 1500^0C for 12 hours ... 44
Figure 3.6. 133 ppm Ca doped Al_2O_3 sintered at 1500^0C for 1 hour ... 45
Figure 3.7. 133 ppm Ca doped Al_2O_3 sintered at 1500^0C for 12 hours ... 45
Figure 3.8. 344 ppm Ca doped α-Al_2O_3 sintered at 1500^0C for 12 hours ... 46
Figure 3.9. 650 ppm Ca doped α-Al_2O_3 sintered at 1500^0C for 12 hours ... 46
Figure 3.10. Undoped α-Al_2O_3 sintered at 1600^0C for 1 hour ... 48
Figure 3.11. 23 ppm Ca doped α-Al_2O_3 at 1600^0C for 1 hour ... 48
Figure 3.12. 344 ppm Ca doped α-Al_2O_3 sintered at 1600^0C for 1 hour ... 49

Figure 3.13. 650 ppm Ca doped α-Al_2O_3 sintered at 1600^0C for 1 hour........................ 49
Figure 3.14. Undoped α-Al_2O_3 sintered at 1400^0C for 1 hour 51
Figure 3.15. 23 ppm Ca doped α-Al_2O_3 sintered at 1400^0C for 1 hour.......................... 51
Figure 3.16. 344 ppm Ca doped α-Al_2O_3 sintered at 1400^0C for 1 hour........................ 52
Figure 3.17. 650 ppm Ca doped α-Al_2O_3 sintered at 1400^0C for 1 hour........................ 52
Figure 3.18. Grain size versus Γ_{Ca} 54
Figure A.1a.1. Measurement of the average grain size of 60 ppm Ca doped sample sintered at 1500^0C for 12 hours 65
Figure A.1b.1. Measurement of the average grain sizes of small and large grains in 133 ppm Ca doped sample sintered at 1500^0C for 12 hours.. 67
Figure B.1.1. a) Undoped α-Al_2O_3 sintered at 1400^0C for 1 hour.................................. 70
Figure B.1.1. b) 7.1 ppm Ca doped α-Al_2O_3 sintered at 14000C for 1 hour 70
Figure B.1.2. a) 10.8 ppm Ca doped α-Al_2O_3 sintered at 1400^0C for 1 hour................ 71
Figure B.1.2. b) 23 ppm Ca doped α-Al_2O_3 sintered at 1400^0C for 1 hour.................... 71
Figure B.1.2. c) 60 ppm Ca doped α-Al_2O_3 sintered at 1400^0C for 1 hour.................... 71
Figure B.1.3. a) 133 ppm Ca doped α-Al_2O_3 sintered at 1400^0C for 1 hour.................. 72
Figure B.1.3. b) 344 ppm Ca doped α-Al_2O_3 sintered at 1400^0C for 1 hour.................. 72
Figure B.1.3. c) 650 ppm Ca doped α-Al_2O_3 sintered at 1400^0C for 1 hour.................. 72
Figure B.2.1. a) Undoped α-Al_2O_3 sintered at 1500^0C for 1 hour.................................. 73
Figure B.2.1. b) 7.1 ppm Ca doped α-Al_2O_3 sintered at 1500^0C for 1 hour.................. 73
Figure B.2.1. c) 10.8 ppm Ca doped α-Al_2O_3 sintered at 1500^0C for 1 hour................ 73
Figure B.2.2. a) 23 ppm Ca doped α-Al_2O_3 sintered at 1500^0C for 1 hour.................... 74
Figure B.2.2. b) 60 ppm Ca doped α-Al_2O_3 sintered at 1500^0C for 1 hour.................... 74
Figure B.2.2. c) 133 ppm Ca doped α-Al_2O_3 sintered at 1500^0C for 1 hour.................. 74
Figure B.2.3. a) 344 ppm Ca doped α-Al_2O_3 sintered at 1500^0C for 1 hour.................. 75
Figure B.2.3. b) 650 ppm Ca doped α-Al_2O_3 sintered at 1500^0C for 1 hour.................. 75
Figure B.3.1. a) Undoped α-Al_2O_3 sintered at 1500^0C for 12 hours 76
Figure B.3.1. b) 7.1 ppm Ca doped α-Al_2O_3 sintered at 1500^0C for 12 hours 76
Figure B.3.1. c) 10.8 ppm Ca doped α-Al_2O_3 sintered at 1500^0C for 12 hours 76
Figure B.3.2. a) 23 ppm Ca doped α-Al_2O_3 sintered at 1500^0C for 12 hours 77
Figure B.3.2. b) 60 ppm Ca doped α-Al_2O_3 sintered at 1500^0C for 12 hours 77
Figure B.3.2. c) 133 ppm Ca doped α-Al_2O_3 sintered at 1500^0C for 12 hours 77

Figure B.3.3. a) 344 ppm Ca doped α-Al_2O_3 sintered at 1500^0C for 12 hours 78
Figure B.3.3. b) 650 ppm Ca doped α-Al_2O_3 sintered at 1500^0C for 12 hours 78
Figure B.4.1. a) Undoped α-Al_2O_3 sintered at 1600^0C for 1 hour.................................. 79
Figure B.4.1. b) 7.1 ppm Ca doped α-Al_2O_3 sintered at 1600^0C for 1 hour................... 79
Figure B.4.1. c) 10.8 ppm Ca doped α-Al_2O_3 sintered at 1600^0C for 1 hour................. 79
Figure B.4.2. a) 23 ppm Ca doped α-Al_2O_3 sintered at 1600^0C for 1 hour..................... 80
Figure B.4.2. b) 60 ppm Ca doped α-Al_2O_3 sintered at 1600^0C for 1 hour..................... 80
Figure B.4.2. c) 133 ppm Ca doped α-Al_2O_3 sintered at 1600^0C for 1 hour................... 80
Figure B.4.3. a) 344 ppm Ca doped α-Al_2O_3 sintered at 1600^0C for 1 hour................... 81
Figure B.4.3. b) 650 ppm Ca doped α-Al_2O_3 sintered at 1600^0C for 1 hour.................. 81

LIST OF SYMBOLS

T	Temperature
X_t	Total concentration of dopant ion
X_t^*	Bulk solubility limit
S_V	Total grain boundary area
Ω	Volume per cation in α-alumina
D	Mean grain diameter
G	Grain size
C_{GB}	Grain boundary concentration
C_{bulk}	Bulk concentration
K	Partitioning coefficient
ΔG_{seg}	Gibbs free energy change due to segregation
k	Boltzman constant
Γ_c	Critical surface coverage
Γ_o	Planar density of available grain boundary sites for adsorption
Γ_Y	Yttrium excess concentration at the grain boundaries
Γ_{Ca}	Calcium excess concentration at the grain boundaries
Γ_{Si}	Silicon excess concentration at the grain boundaries
$\overline{L}$	Mean linear intercept length
μ	Micron
nm	Nanometer
mm	Millimeter
^0C	Degrees Celsius

LIST OF ABBREVIATIONS

α-Al_2O_3	Alpha alumina
AGG	Abnormal grain growth
YAG	Yttrium alumina garnet
TEM	Transmission electron microscope
STEM	Scanning transmission electron microscope
HRTEM	High resolution transmission electron microscope
AEM	Auger electron microscope
SIMS	Scanning secondary ion mass spectrometry
SEM	Scanning electron microscope
EDS	Energy dispersive spectrometer
ICP-OES	Inductively coupled plasma-optical emission spectroscopy
rpm	Revolution per minute
ppm	Part per million
%TD	Percent theoretical density
wt%	Weight percent

1. INTRODUCTION

Microstructure of materials plays a significant role in determining their properties. Creation and control of optimal grain structures is one of the primary concerns in designing a material. The presence of small amounts of impurities in the starting material can strongly influence their mechanical, optical electrical and dielectric properties. In the scope of this thesis, the effects of calcium impurities on the α-Al_2O_3 microstructure during sintering was investigated

Aluminium oxide is the most widely used oxide ceramic either in pure form or as raw material to be mixed with other oxides. Alumina (α-Al_2O_3) has mechanical and physical properties particularly suitable for electrical and thermal insulation, for cutting tools and abrasives. It also has very good anti-corrosion properties. It can be found in different degrees of purity and crystal structures, with different properties. Transparent alumina, used for optical applications, can also be manufactured.

For many years the effects of various impurities such as Ca, Si, Mg and Y on the microstructure of alumina (α-Al_2O_3) and related properties have been studied extensively by various scientists. Calcium is one of the most common impurities in alumina that is believed to affect the interface related phenomena such as sintering, grain growth, creep, intergranular fracture and morphology.

1.1. A Brief Review of the Crystallography of α-Al_2O_3

The crystal structure of α-Al_2O_3 is often described as having O^{2-} anions in an approximately hcp arrangement with Al^{3+} cations occupying two-thirds of the octahedral interstices, as shown in Figure 1.1. The empty sites of the cation sublattice are used to define the corners of the unit cell (Figure 1.2). The crystallography of sapphire, α-Al_2O_3, can be considered in terms of morphological unit cell, as defined by mineralogists, or a structural unit cell, as defined by X-ray crystallographers, using rhombohedral Miller indices or hexagonal Miller-Bravais indices [1]. The structural hexagonal unit cell, which properly accounts for the combined anion and cation sublattices, is twice the volume of the morphological unit cell and rotated by 180^0 around the c-axis. The relationship between the two cells is shown in Figure 1.3 [1].

The crystallographic specifications are given in Table 1.1. for both rhombohedral and hexagonal structural unit cells [1].

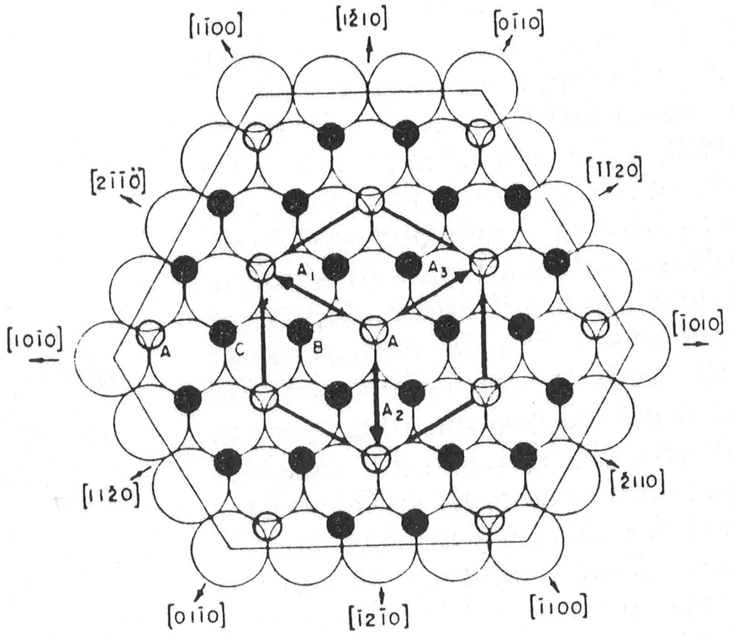

Figure 1.1. The basal plane of sapphire, showing the hexagonal close-packed anion sublattice and the cations occupying two-thirds of the octahedral interstices [1]

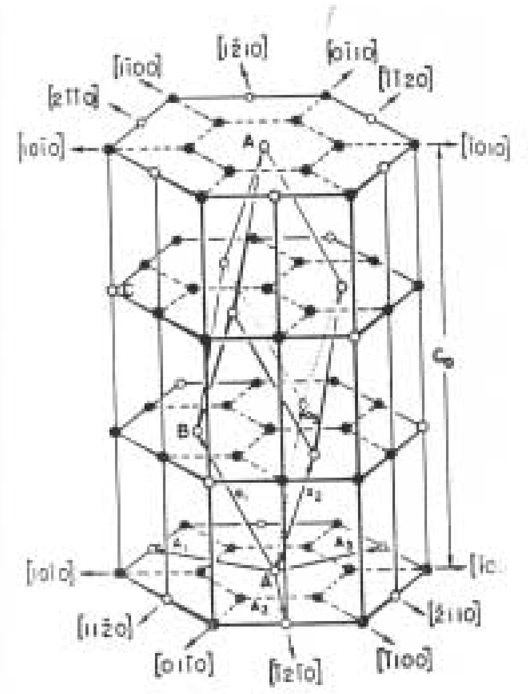

Figure 1.2. The cation sublattice in sapphire. The vacant octahedral sites define the corners of a morphological unit cell [1]

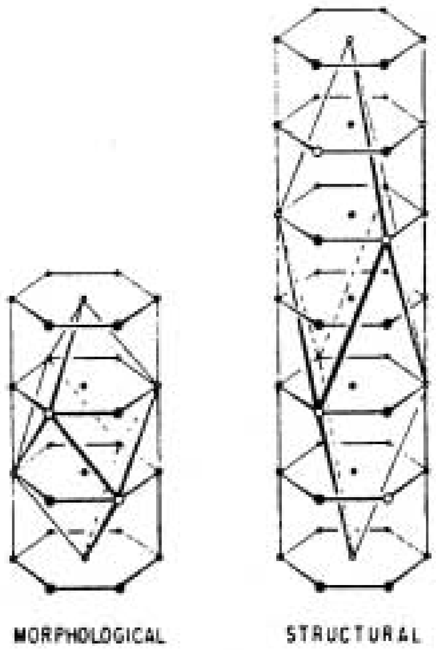

Figure 1.3. The two types of unit cell for sapphire: (a) the morphological unit cell and (b) the structural unit cell [1]

Table 1.1. Crystallographic specifications of α-Al_2O_3

	Rhombohedral Structural Unit Cell	*Hexagonal Structural Unit Cell*
Lattice Parameters	a = 5.1284 Å $\alpha = 55.28^0$	a_0 = 4.7589 Å c_0 = 12.991 Å
Cell Volume	V = 84.929 Å^3	V = 254.792 Å^3
Formula units per cell	n = 2	n = 6

As it will be presented in the following sections, impurities segregate preferentially to different planes in alumina. Thus, it is also important to define the common crystallographic planes in sapphire. In Figure 1.4., planes in sapphire were shown with respect to each other and in Table 1.2. names and Miller indices of these planes were given.

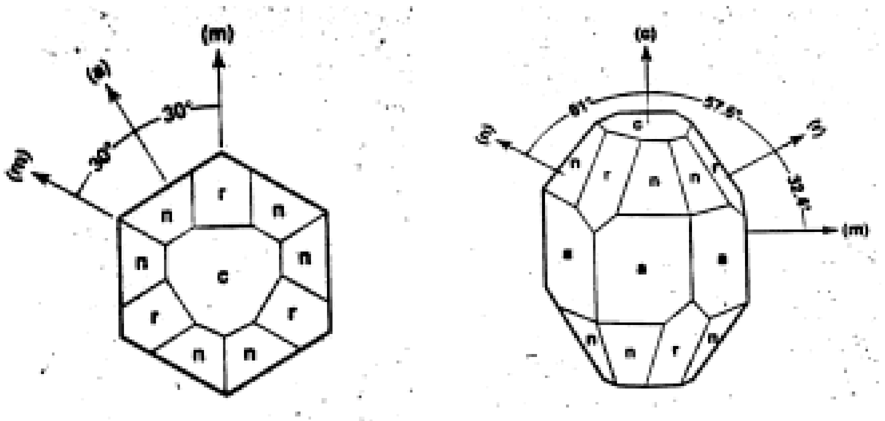

Figure 1.4. Common crystallographic planes in sapphire

Table 1.2. Specifications of the common crystallographic planes in sapphire

Plane “name”	**Miller Index**
a, prismatic	$(11\bar{2}0)$
m, prismatic	$(10\bar{1}0)$
c, basal	(0001)
r, rhombohedral	$(1\bar{1}02)$
n	$(11\bar{2}3)$
s, pyramidal	$(10\bar{1}1)$

1.2. Theory of Sintering

While metals and polymers are usually molten, cast, and, when necessary machined or forged into the final desired shape, the processing of ceramics poses considerable difficulty. In ceramics the starting point is usually fine powders that are milled, mixed and molded into the desired shape by a variety of processes and subsequently heat treated or fired to convert them to dense solids. Sintering is the process by which a powder compact is transformed to a strong, dense ceramic body upon heating. It is a complex phenomenon in which several processes are occurring simultaneously. The driving force for sintering is quite small that it is hard to achieve full density during the process.

Sintering can occur in the presence or absence of a liquid phase. In the liquid phase sintering the compositions and firing temperatures are chosen such that some liquid is formed during processing. In the absence of a liquid phase, the process is referred to as solid state sintering.

1.2.1. Solid State Sintering

The macroscopic driving force during sintering is the reduction of the excess energy associated with surfaces. This can happen by (1) reduction of the total surface area by an increase in the average size of particles, leads to coarsening (Figure 1.5b), and/or (2) the elimination of solid/vapor interfaces and the creation of grain boundary area, followed by grain growth, which leads to densification (Figure 1.5a) [2]. If the atomic processes that lead to densification dominate, the pores get smaller and disappear with time and the compact shrinks. But if the atomic processes that lead to coarsening are faster, both the pores and grains coarsen and get larger with time. Full density is thus obtained only when the atomic processes associated with coarsening are suppressed, while those associated with densification are enhanced.

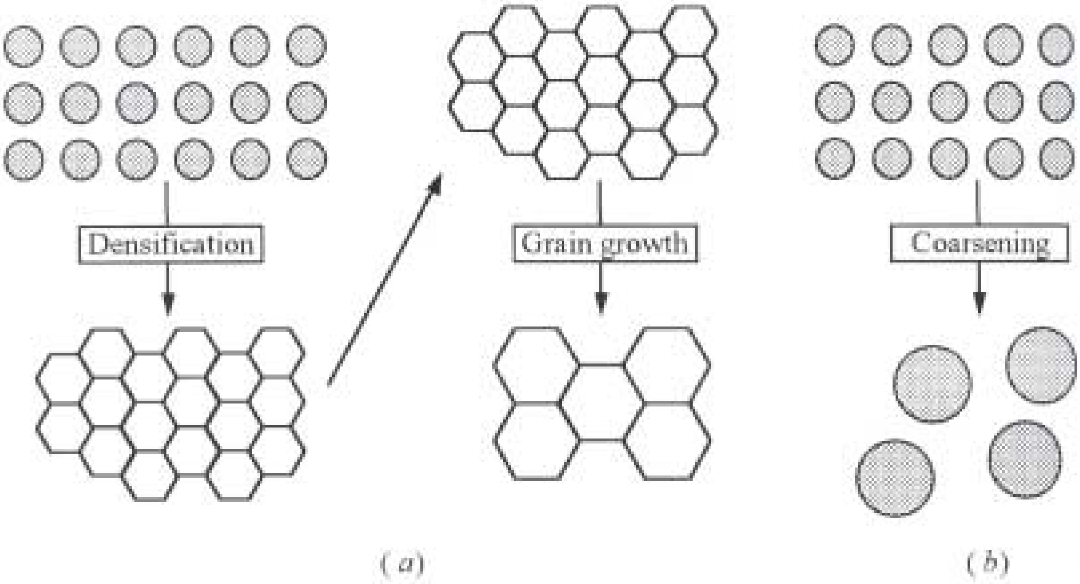

Figure 1.5. Schematic of two possible paths by which a collection of particles can lower its energy. (a) Densification followed by grain growth. (b) Coarsening where the large grains grow at the expense of the smaller ones [2].

There are basically five atomic mechanisms by which mass can be transferred in a powder compact [2]:

1. Evaporation-condensation, depicted as path 1 in Figure 1.6a.
2. Surface diffusion, or path 2 in Figure 1.6a.
3. Volume diffusion. Here are the two paths. The mass can be transferred from the surface to the neck area (path 3 in Figure 1.6a) or from the grain boundary area to the neck area (path 5 in Figure 1.6b).
4. Grain boundary diffusion from the grain boundary area to the neck area (path 4 in Figure 1.6b).
5. Viscous or creep flow. This mechanism entails either the plastic deformation or viscous flow of particles from areas of high stress to low stress and can lead to densification.

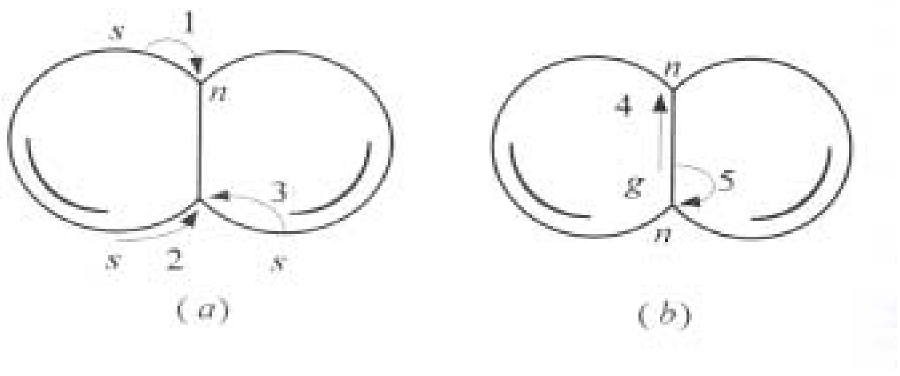

Figure 1.6. Basic atomic mechanisms that lead to (a) Coarsening and change in pore shape and (b) densification [2]

Typically a solid state sintered ceramic is an opaque material containing some residual porosity and grains that are much larger than the starting particle sizes. The important factors that control the solid state sintering were summarized by Barsoum as follows [2]:

1. *Temperature:* Since diffusion is responsible for sintering, increasing temperature will greatly enhance the sintering kinetics. The activation energies for bulk diffusion are usually higher than those for surface and grain boundary diffusion. Therefore, increasing the temperature usually enhances the bulk diffusion mechanisms which lead to densification.
2. *Green density:* Usually a correlation exists between the green (prior to sintering) density and the final density, since the higher the density, the less pore volume that has to be eliminated.
3. *Uniformity of green microstructure:* More important than the green density is the uniformity of the green microstructure and the lack of agglomerates.
4. *Atmosphere:* The effect of atmosphere can be critical to the densification of a powder compact. In some cases, the atmosphere can enhance the diffusivity of a rate controlling species. In other cases, the presence of a certain gas can promote coarsening by enhancing the vapor pressure and totally suppressing densification.
5. *Impurities:* The roles of impurities have been studied extensively and their effects were summarized as follows:
   a. Sintering aids: They are purposefully added to form a liquid phase.

    b. Suppress coarsening by reducing the evaporation rate and lowering surface diffusion.
    c. Suppress grain growth and lower grain boundary mobility.
    d. Enhance diffusion rate.
6. *Size distribution:* Narrow size distributions will decrease the propensity for abnormal grain growth (AGG).
7. *Particle size:* Since the driving force for densification is the reduction in surface area, the larger the initial surface area, the greater the driving force. However to use very fine particles pose some serious problems. As the surface/volume ratio of the particles increases, electrostatic and other surface forces become dominant, which leads to agglomeration. Upon heating agglomerates have a tendency to sinter together into larger particles, which not only dissipates the driving force for densification but also creates large pores between the partially sintered agglomerates which are subsequently difficult to eliminate.

1.3. Grain Growth and Coarsening

During the final stages of sintering, in addition to the elimination of pores, a general coarsening of the microstructure by grain growth occurs. During this process the average grain size increases with time as the smaller grains are consumed by larger grains. Controlling and understanding the processes that lead to grain growth are important for two reasons. The first is related to the fact that grain size is a major factor determining many of the electrical, magnetic, optical, and mechanical properties of ceramics. The second is related to suppressing what is known as abnormal growth, which is the process whereby a small number of grains grow very rapidly to sizes that are more than an order of magnitude larger than average in the population. In addition to the detrimental effect that the large grains have on the mechanical properties, the walls of these large grains can pull away from porosities, leaving them trapped within them, which in turn limits the possibility of obtaining theoretical densities in reasonable times [2].

1.3.1. Grain Boundary Migration

Since the average grain size increases during grain growth, the total number of grains must decrease in order to conserve volume. An equivalent way of looking at grain growth is to evaluate the rate of grain disappearance. The change in chemical potential of atoms across a curved grain boundary is the driving force that makes the boundary move towards its center of curvature [3].

One result of the pressure difference across a curved surface is a change in solubility or vapor pressure as compared to a planar surface. The pressure applied to the liquid or solid by the curved surface increases the chemical potential of its constitutes and the pressure of the vapor phase in equilibrium with it. A convex surface (positive r) has a greater equilibrium vapor pressure than a planar surface (infinite r), which in turn has a greater vapor pressure than the convex surface (negative r). The amount of this increase can be derived by considering the transfer of one mole of material from the flat surface, through a liquid or vapor, to the spherical surface. With temperature, external pressure and overall composition held constant, the work done is equal to the change in chemical potential ($\mu=\mu^{o} + RT \ln a$, where μ^0 is the standard chemical potential and a the activity). Assuming a constant activity coefficient, the chemical potential difference is given by

$$\Delta\mu=(RT \ln c - RT \ln c_0) \text{ or } \Delta\mu=(RT \ln p - RT \ln p_0) \qquad (1.1)$$

where c is the solubility and p is the vapor pressure, and c_0 and p_0 are the equilibrium solubility and vapor pressure over a flat surface [3].

Grain boundaries which are equal in energy meet at three grain junctions to form angles of 120^0. As illustrated in Figure1.7, if all boundaries are required to meet with an angle of 120^0, grain boundaries without curvature only occur for six sided grains. Grains with fewer sides have boundaries that are concave when observed from the center of the grain. These are the grains that shrink and eventually disappear as grain boundaries migrate toward their center of curvature. Grains with more than six sides have convex boundaries that migrate outward and tend to grow larger. In three dimensions, the net curvature determines the direction of migration [3].

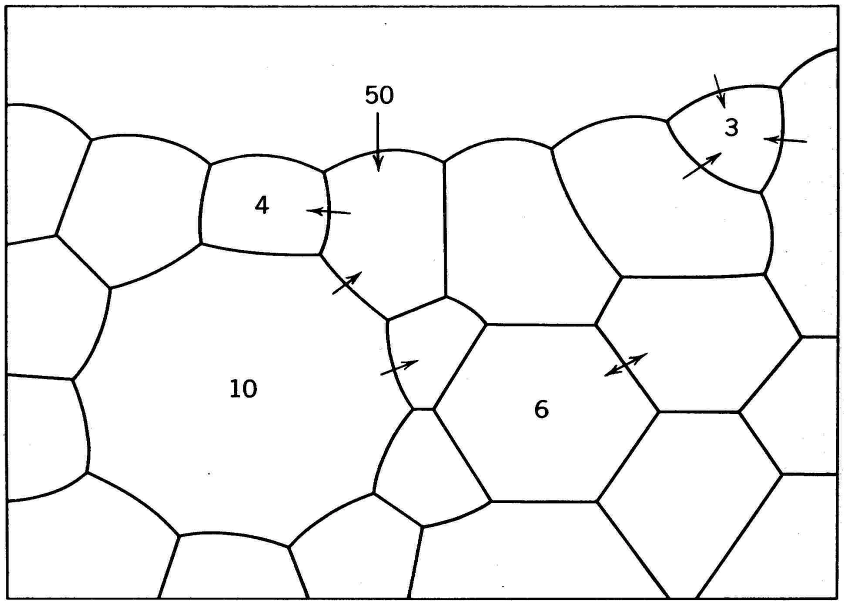

Figure 1.7. Schematic drawing of two-dimensional polycrystalline specimen [3]

1.3.1.1. Effect of microstructure and grain boundary chemistry on boundary mobility

The presence of "second phases" or solutes at the boundaries can have a dramatic effect on their mobility, and from a practical point of view it is usually the mobility of these phases that is rate-limiting. To illustrate the complexity of the problem, it can be considered just a few possible rate-limiting processes [2]:

1. Intrinsic grain boundary mobility.
2. Extrinsic or solute drag. If the diffusion of the solute segregated at the grain boundaries is slower than the intrinsic grain boundary mobility, it becomes rate limiting. In other words, if the moving grain boundary must drag the solute along, that tends to slow it down.
3. The presence of inclusions (basically second phases) at the grain boundaries. It can be shown that larger inclusions have lower mobilities than smaller ones, and that the

higher the volume fraction of a given inclusion, the larger the resistance to boundary migration.

4. Material transfer across a continuous boundary phase. For instance, in Si_3N_4 boundary movement can occur only if both silicon and oxygen diffuse through the thin, glassy film that usually exists between grains.
5. In some cases, the redissolution of the boundary anchoring second phase inclusions into the matrix can be rate limiting.

In addition to these, the following interactions, between pores and grain boundaries can occur [2]

1. What is true of second phases is also true of pores. Pores cannot enhance boundary mobility; they only leave it unaffected or reduce it. During the final stages of sintering as the pores shrink, the mobility of the boundaries will increase.
2. The pores do not always shrink. They can also coarsen as they move along or intersect a moving grain boundary.
3. The pores can grow by the Ostwald ripening mechanism.
4. Pores can grow by reactive gas evolution and sample bloating.

As the grains get larger and the pores fewer, the grain mobility increases accordingly. In some cases, at a combination of grain size and density, the mobility of the grain boundaries becomes large enough that the pores can no longer keep up with them; the boundaries simply move too fast for the pores to follow and consequently unpin themselves.

1.3.1.2. Impurity Segregation at Grain Boundaries

Impurities exist in a material in different configurations as shown in Figure 1.8. They can be a solute in the bulk, or an adsorbate at the grain boundaries. After reaching solubility limit, they can precipitate as second phase particles at multigrain junctions. They can also exist in grain boundary films (amorphous or crystalline) or in amorphous triple point pockets.

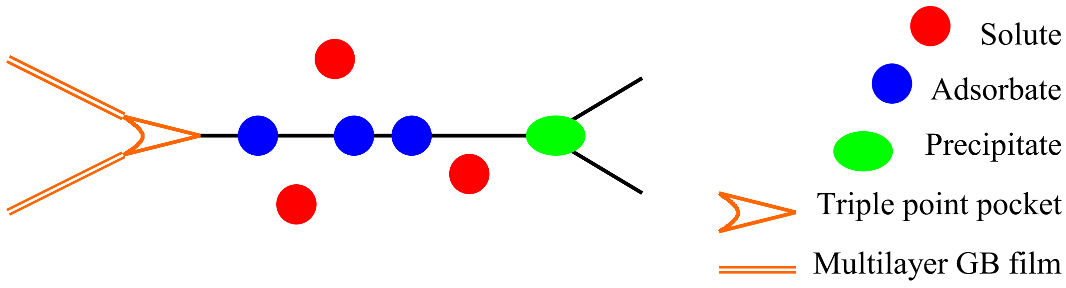

Figure 1.8. Impurity distribution

Impurities at any concentration will exist in the bulk as a solute and segregate at grain boundaries. In dilute solutions, i.e, if the concentration of solute in the bulk is lower than the bulk solubility limit, ($X_t<X_t^*$), the ratio of the grain boundary concentration C_{GB} to bulk concentration C_{bulk} (K, partitioning coefficient) depends on the free energy change due to segregation ΔG_{seg} and is given by

$$C_{gb}/C_{bulk} = K = \exp(\Delta G_{seg}/kT) \qquad (1.2)$$

One of the contributions to the decrease in free energy comes from the reduction in strain energy resulting from segregation of the solute that is a misfit in the lattice. It can be shown that this decrease in strain energy scales as $[(r_2-r_1)/r_1]^2$, where r_1 and r_2 are the ionic radii of the solvent and solute ions, respectively. Hence, the larger the radii differences, the greater the driving force for segregation. It should be noted that it is the absolute size difference that is important; i.e., both smaller and larger ions will segregate to the grain boundary. The reason is obvious. Grain boundaries are regions of disorder that can easily accommodate different sized ions as compared to the bulk. Consequently, if ΔG_{seg} is large, the grain boundary chemistry can be quite different from that of the bulk, magnifying the effect of impurities [2].

Impurity segregation at the grain boundaries can be modelled by using simplified Langmuir-Mc Lean relation. This model was also used by Gulgun et al. [31] in calculating the grain boundary coverage of yttrium in α-alumina for low yttrium concentrations. In Figure 1.9., it was shown that surface coverage of an impurity (Γ) is a function of impurity content and grain size. For low yttrium concentrations the measured Γ_Y followed the Langmuir-Mc Lean model quite well [31]. However, when the yttrium content increases to 100 ppm the concentration of yttrium reaches the bulk solubility limit ($X_L = X_L^*$) at about a grain size of 5-7µ and it precipitates as yttrium alumina garnet (YAG). After precipitation, Γ deviates strongly from the Langmuir-Mc Lean model that is depicted by the dashed line in the plot.

Γ_c is the critical surface coverage that defines the level of segregation that will be in equilibrium with the second phase precipitates. The transient (non-equilibrium) surface coverage could exceed this critical value of Γ_c, if there is an effective nucleation barrier to the second phase precipitation. In yttrium's case, a supersaturation of Γ_Y was observed prior to second phase appearance [31].

Same model was adapted as the basis for this thesis in order to calculate the calcium coverage at grain boundaries. The detailed calculations and discussions were given in Section 3.3.

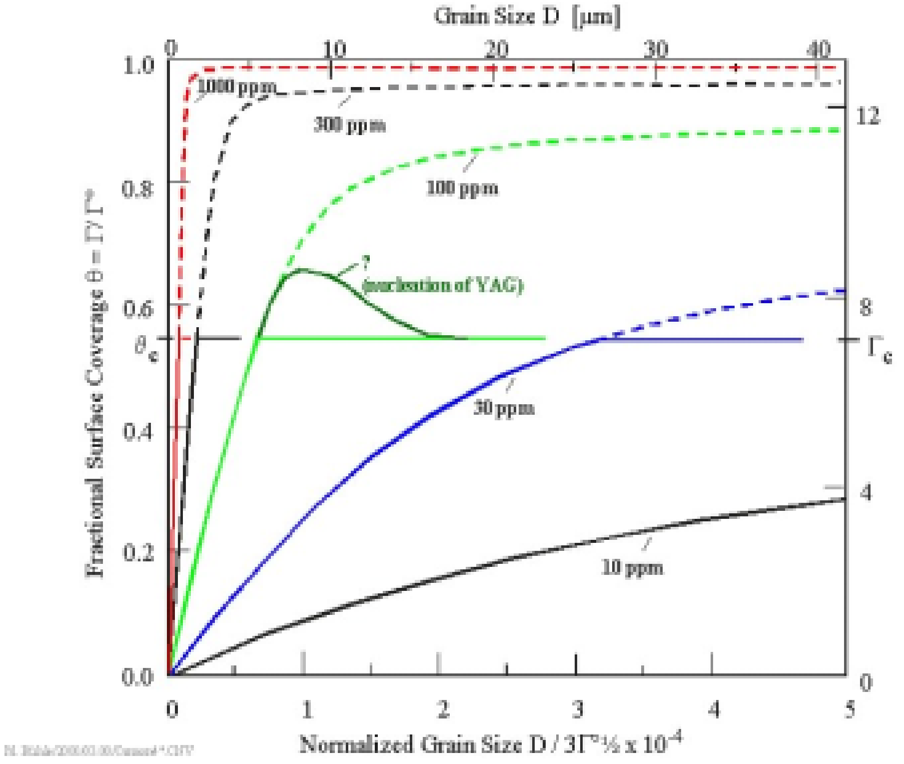

Figure 1.9. Plot of yttrium grain boundary concentration versus grain size [Rowland Cannon]

As mentioned above grain boundary segregation strongly depends on the grain size. Figure 1.10. which is after M. Ruehle shows that when the grain size doubled the concentration of the segregant at the grain boundaries increases twice the original value. In this figure the number of impurity atoms are exactly same for both drawings and the grain size of the second drawing is exactly twice of the first one.

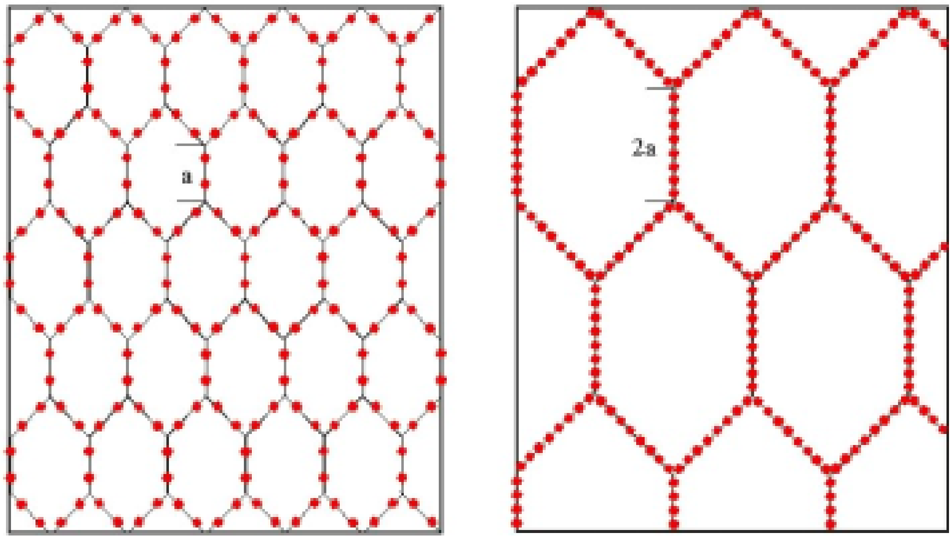

Figure 1.10. Segregation at grain boundaries for different grain boundary densities [Manfred Ruehle]

1.4. Phase Equilibria in CaO-Al_2O_3 System

Phase diagrams are graphical representations of what equilibrium phases are present in a material system at various temperatures, compositions, and pressures given the system is allowed to reach equilibrium.

In principle, phase diagrams provide the following information [2]:

1. The phases present at equilibrium
2. The composition of the phases present at any time during heating or cooling
3. The fraction of each phase present
4. The range of solid solubility of one element or compound in another

In Figure 1.11. it is shown that the calculated phase equilibrium diagram of CaO-Al_2O_3 system [6]. “Calculation was performed based on the experimentally determined thermodynamic properties of all intermediate phases and melts. Gibbs energies of the phase transitions for Al_2O_3 and CaO were chosen from the All-Union databank of thermodynamic values, IVTANTERMO. Coordinates of the phase boundaries were determined by solving sets of equations expressing equality of chemical potentials of the components in coexisting phases. All the phases in this system were taken into consideration. The nature and quantity of the coexisting phases were established by a search for the Gibbs energy minimum of this system."[6]

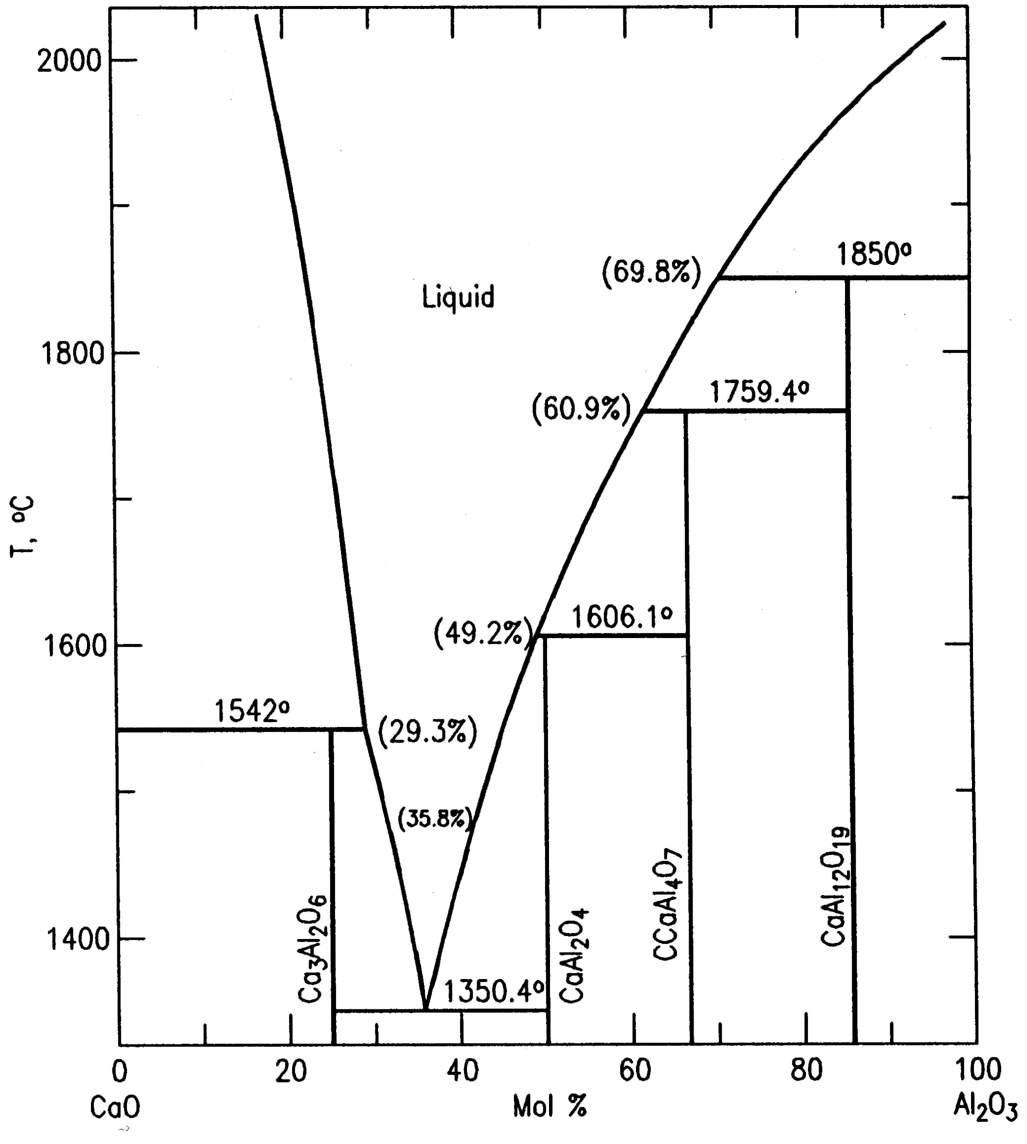

Figure 1.11. System CaO-Al2O3. Calculated phase equilibrium diagram.

- I. Zaitsev, N. V. Korolyev, and B. M. Mogutnov, J. Mater. Sci., 26 [6] 1588-1600 (1991)
- I. Zaitsev, N. V. Korolyev, and B. M. Mogutnov, High. Temp. Sci., 28, 351-377 (1989)

Al_2O_3-CaO binary is one of the systems where the calculated and experimentally established phase diagrams agree reasonably well.

1.5. Literature Review about the Effects of Various Impurities on the Microstructure of α-Al_2O_3

For many years the effects of various impurities such as Ca, Si, Mg and Y on the microstructure of Al_2O_3 and related properties have been studied extensively by various groups.

Although commercially available α-Al_2O_3 contains many impurities in it, it has very limited solubility for most of them. This results in strong segregation of impurities (and/or dopants) to the grain boundaries, which affects the sintering and microstructural development of the material. The role of grain boundaries in the sintering process is essential for the formation of dense ceramics since grain boundaries act as sinks for the vacancies.

Grain boundary microstructures in a commercial 99.8% alumina ceramic were analyzed by Hansen and Phillips [7]. In their study, transmission electron microscopy revealed that all grain boundaries were wetted by an amorphous film. In the microstructure, both ledged boundaries and annealing twins were present. They examined several glass pockets by energy dispersive X-ray microanalysis in the STEM. Estimated composition of glass phase that reported was 39 wt% Al_2O_3, 30 wt% SiO_2, 29 wt% CaO and 1 wt% TiO_2. They also reported facets of widely differing sizes primarily on basal {0001}, rhombohedral $\{\bar{1}012\}$, and prism $\{11\bar{2}0\}$ planes.

Similarly, Brydson et al. [8] studied the structure and chemistry of two-grain boundaries and three-grain junctions with analytical and high resolution transmission electron microscopes (HRTEM) in polycrystalline alumina sintered with additions of calcium silicate between 0 and 10 wt%. They observed a continuous amorphous grain boundary film at the majority of the two-grain boundaries. The thickness of the grain boundary film was measured as 1.2-2 nm which was independent of the bulk level additive. One significant result of this study was that the chemistry of the glass at the grain boundaries and the three-grain junctions were different. Triple point pockets were predominantly silicon rich and typically within the primary phase field of anorthite ($CaO-Al_2O_3-2SiO_2$, CAS_2). The grain boundaries on the other hand showed strong segregation of calcium. It was reported that analysis of two-grain boundaries in the 10 wt% sample gave an excess calcium concentration of Γ_{Ca}=6.1 atoms/nm^2. Generally, the level of calcium segregation was between 0.5 and 1 monolayer and spread over a grain boundary thickness of 2 nm (6-7 cation planes). This value gave an average [Ca]:[Al] atomic ratio of 0.07-0.14 which corresponds to the nominal composition in the primary phase field of calcium hexa-aluminate ($CaO.6Al_2O_3$, CA_6).

Most of the studies on the Ca doped α-Al_2O_3 was focused on the anisotropic segregation of calcium to the surfaces and grain boundaries of alumina and abnormal grain growth which has been related with the formation of glassy films on the grain boundaries when the amount of calcium and silica content together exceeded a critical concentration.

In order to understand the effects of calcium in alumina, it is crucial to understand the segregation behavior of calcium. However, there are still some disagreements among the scientists on this subject.

Baik *et al.* [9] have measured the surface enrichment of Ca on various crystallographic planes of CaO doped sapphire as a function of annealing temperature using Auger electron spectroscopy. In this study, no Ca segregation was observed to the (0001) basal plane in the temperature range 800° to 1500°C. However, the surface phase transformation was seen above 1300°C without any evidence of impurity presence on the surface. On the other hand, strong enrichment of Ca on the $(10\bar{1}0)$ plane was observed between 1300°-1500°C and small but noticeable amount of Ca was detected even below 1300°C. The segregation of Ca on this prism plane was found to be uniform and limited to the surface monolayer and was concurrent with a 2D phase transformation. Such anisotropy in Ca segregation was thought to be the probable reason of the formation of nonuniform microstructures often observed in sintered alumina which typically contains a small amount of Ca as an impurity.

Similar experiments were done by Mukhopadhyay and Baik [10] on the segregation of magnesium and calcium to the $(10\bar{1}0)$ prismatic plane of magnesium doped sapphire. It was observed that segregation behavior depended strongly upon the annealing atmosphere. Mg segregation to the free surface was only detected in air annealing whereas there was no observable Mg segregation in vacuum annealing.

Instead, strong Ca segregation was detected in the absence of Mg on the surface which was attributed to the excessive vaporization of MgO at low oxygen pressures. The fact that Ca segregation did not occur while annealing in air was explained as the effectiveness of Mg on the surface in repelling Ca. By the comparison of the surface-to-bulk ratios of Ca and Mg concentrations and also the greater size mismatch between Ca^{+2} and Al^{+3} than between Mg^{+2} and Al^{+3}, it was expected that Ca should be the more effective segregant. However, the authors suggested that the mobility of the Mg^{+2} containing defect was much greater than that for the corresponding Ca^{+2} defect so that the Mg established its surface concentration much more rapidly.

In contradiction with the results of these mentioned studies, Kaplan *et al.* [11] observed Ca segregation to basal surfaces of alumina in melt-infiltrated polycrystalline alumina-aluminum composites. The presence of Ca at the embedded basal surfaces of α-Al_2O_3 was shown by high-resolution transmission electron microscopy (HRTEM) combined with analytical electron microscopy (AEM). In the study, measurements were taken from more than seven different basal α-Al_2O_3/Al interfaces, and the structural width was found to be 0.8±0.2 nm. It was observed that calcium excess at the same interfaces was Γ_{Ca}=2.5±0.5 Ca atoms/nm^2 and Ca existed not only at the surface, but rather was spread over four cation layers, which resulted in a surface phase having the nominal composition of $CaO.6Al_2O_3$. It was also found that Ca segregated to basal twin boundaries, but with total excess less than at the free basal surfaces. Kaplan et al. also showed the elongated morphology of alumina grains with Ca segregation.

In order to understand the segregation behavior of Ca to the grain boundaries Cook *et al.* [12] examined the fracture surfaces of a series of CaO-doped polycrystalline alumina by Auger electron spectroscopy and scanning electron microscopy. In order to determine the grain boundary concentrations from spectroscopy on the fracture surfaces, as-fractured and sputtered surface spectra were measured as well as the proportion of transgranular failure exposed to the probe beam. Relative to that of single crystal sapphire, polycrystalline alumina spectra were characterized by the appearance of Ca^{LMM} signal and a diminished low energy Al^{LMM} signal. Sputtering of the polycrystalline surface resulted in the disappearance of the Ca^{LMM} signal and restoration of the Al^{LMM} signal to that observed for sapphire. This result implied that Ca atoms were substitutionally segregating to Al_2O_3 grain boundaries [12]. It was also mentioned that the segregation of Ca to the grain boundaries exposed by the fracture process was quickly saturated. Study suggests that the proportion of transgranular failure increased strongly with increasing grain boundary Ca segregation with adverse influences on fracture properties such as toughness. However, the direct proportionality between the transgranular fracture and grain boundary Ca segregation, suggested by Cook *et al.* [12] appears to be premature. Dependence of the fracture behavior of the material on the grain size has to be included into consideration before a firm conclusion can be drawn. Abnormal grain growth related to the Ca addition into alumina can be a more logical explanation for the occurrence of transgranular failure instead of intergranular failure.

The combined effect of some impurities such as silicon and calcium on the microstructure of alumina is dramatic. The phenomenon of strong abnormal grain growth is observed due to the presence of these impurities.

Abnormal grain growth in alumina is not an intrinsic property but rather controlled by certain impurities that enter the ceramic during powder synthesis, processing or sintering. It in turn affects various interfacial properties in sintering, densification, creep, intergranular fracture, etc. Its control or prevention is of utmost importance. Various mechanisms have been proposed to explain abnormal grain growth in alumina. For instance, a wide initial particle size distribution, separation of grain boundary from pinning particles, pore-boundary separation, inhomogeneous packing and densification, anisotropic grain boundary mobilities, presence of certain fluxing impurities such as sodium and potassium in alumina, uneven distribution of impurities such as Ca and Si, or formation of liquid phase during sintering have been considered previously. However, it is now generally believed that regardless of particle size, size distribution or packing, the presence of impurities, notably of CaO and SiO_2 in the starting powder, plays a decisive role for triggering abnormal grain growth in the final stage of sintering. Such impurities are believed to form glassy films in grain boundaries. These glassy films have long been regarded to catalyze abnormal grain growth by some yet unknown mechanism. Besides understanding the causes, it is also very important to control abnormal grain growth in the final stage of densification for attaining high density in alumina by sintering. It was found that addition of a small amount of MgO was a key step to control abnormal grain growth and to fabricate fully dense, translucent alumina (Lucalox^{TM} process by R. L. Coble, U.S. Patent 3,026,210).

S. I. Bae and Baik [13] have determined minimum amounts of SiO_2 and CaO required for inducing abnormal grain growth using ultra-pure alumina (>99.999%) and sintering at 1900°C for 1h in a contamination free condition. The critical concentrations of silicon in cationic mole fractions in alumina was found 300 ppm without calcium, 200 ppm with 10 ppm calcium and 150 ppm with 20 ppm calcium. The critical concentration of calcium alone was observed as 30 ppm. It was also suggested that the abnormal grain growth in commercially pure alumina is related to formation of a small amount of liquid phase during sintering. In this study, only total impurity content to trigger abnormal grain growth was regarded. However, both Si and Ca have limited solubility in Al_2O_3 and will strongly segregate to grain boundaries in polycrystalline alumina. Using the reported grain sizes, the amount of Si excess at grain boundaries to trigger abnormal grain growth in the absence of Ca impurities was calculated to be around 60 Si atoms/nm^2. This value would correspond to about 5 layers of silicon-oxygen layers at the grain boundaries. In regard of high propensity for silicon, aluminum, oxygen system to form glass, it is conceivable that amorphous films may exist at grain boundaries at these high doping levels.

I. J. Bae and Baik [14] have measured final densities and grain sizes after sintering ultrapure alumina using different environments. As a result of sintering in a contamination-free sapphire tube furnace no evidence of abnormal grain growth was observed. When the average grain sizes were plotted as a function of sintering time at various sintering temperatures, it was shown that the grain growth followed a normal grain growth behavior. It was also seen that grain growth accelerated continuously without abnormal grain growth as densification proceeded in the clean sintering condition. On the contrary, under the normal sintering condition using a commercial alumina crucible (99.8%), abnormal grain growth has occurred as the grain size became 15-20 μm and the relative density has reached around 92%, even though its trajectory has followed smaller grain sizes for given densities. The microstructural condition for abnormal grain growth was also studied and it was concluded that the critical average grain sizes were always inversely related with the doping concentration except very high doping levels [14].

In a study that was performed by Park and Yoon [15], 99.98% pure α-alumina powder was mixed with pure $Si(OC_2H_5)_4$ and pure $Ca(NO_3)_2.xH_2O$ in ethyl alcohol. They observed large, elongated grains with faceted grain boundaries and they did not find any frozen liquid at the triple point junctions and grain boundaries. Addition of MgO suppressed the AGG and the grain boundaries became curved. According to these results they correlated the occurrence of AGG in alumina with the formation of faceted and straight grain boundaries. It was proposed that these grain boundaries have singular ordered structures with low boundary energies and their growth by lateral step movement can cause AGG. The addition of MgO causes grain boundary roughening and, thus, normal grain growth.

Segregation behavior of TiO_2 and SiO_2 doping and their effects on the microstructure of alumina were studied by Kim and Kebbede et al. [16, 17]. It was shown that TiO_2 promoted grain growth but there were no abnormally grown grains. Co-doping of TiO_2 and SiO_2 resulted in a duplex microstructure consisting of large platelike grains [16]. Ti was found to segregate preferentially to the faceted or curved edge boundaries of platelets [17].

The Lucalox^{TM} process (for transLUCent ALuminum OXide) was a discovery by Robert L. Coble (U.S. Patent 3,026,210). Magnesia was a critical additive which allowed alumina to be sintered to theoretical density. P. D. S. St. Pierre and A. Gatti at General Electric had developed a firing process (U .S. Patent 3,026, 177), which resulted in translucent material. Its long life as a topic of scientific interest has been largely due to the elusiveness of an adequate explanation for the effect of magnesia. According to S. J. Bennison and M. P. Harmer [18] by 1989 sixty papers related to the sintering of this one system had been published. Here only some of the studies that were done on the subject of MgO doped alumina is mentioned [18-30].

Small additions of MgO greatly improve the sinterability of Al_2O_3 powders, enabling the fabrication of ceramics with high densities and controlled grain sizes. In the absence of magnesia, pores become entrapped within the alumina grains as abnormal grain growth takes place during sintering. These pores are impossible to remove in a reasonable firing time since the lattice transport required is extremely slow. Pores scatter light and render the alumina opaque. Coble showed that by using about 0,25 weight % magnesia, and firing at ~1900°C in hydrogen atmosphere, a completely dense alumina with no entrapped pores could be obtained. (Lucalox^{TM} is actually not completely transparent, but somewhat translucent since the refractive index of corundum is anisotropic (birefringent), and some light scattering takes place in the randomly oriented polycrystal even if it is fully dense.) It was later shown that firing in vacuum or a soluble gas such as hydrogen or oxygen yields similar results, while firing in an insoluble gas such as nitrogen, air (which is mostly nitrogen), helium or argon prevents full densification due to internal gas pressure building to equilibrium with the capillary pressure of the pore.

While the effect of magnesia was easily demonstrated, understanding the mechanism by which it acts took much longer. Densification occurs when pores located at grain boundaries are removed by lattice or grain boundary diffusional processes. Once a pore becomes entrapped within the grain, however, lattice diffusion (in corundum as well as most other ceramics) is prohibitively slow for much further densification. Thus, the key to achieving transparency is the prevention of pore-grain boundary separation. Coble [19] outlined several specific mechanisms by which this could be accomplished:

1. Second phase particles of $MgAl_2O_4$ spinel, resulting from an excess of magnesia beyond the solid solution limit, pin grain boundaries and prevent abnormal grain growth.
2. Magnesia in solution segregates to grain boundaries and lowers grain boundary mobility by solid solution-drag. The pores then remain attached to boundaries and can be removed by the usual densification processes.
3. Magnesia changes the equilibrium pore shape by changing the relative values of surface energy and grain boundary energy. For a pore of constant volume, a lowering of the dihedral angle causes a greater area of the grain boundary to be intersected by the pore, and results in a larger drag force.
4. The rate of densification is increased relative to the rate of grain growth by magnesia in solid solution. Coble believed that the lattice diffusion of aluminum was rate limiting, while oxygen was more rapidly transported along the grain boundaries.

A. H. Heuer [20, 21] later added a fifth possibility:

5. Magnesia increases the rate of surface diffusion in alumina, thereby increasing the mobility of pores and allowing them to keep up with migrating boundaries.

It is of course possible for more than one of these mechanisms to be acting at the same time. During the 1970s and 1980s, much effort was expended in model experiments and measuring fundamental parameters necessary to support or exclude particular mechanisms. In the case of both grain boundary segregation of magnesia (necessary for solid solution drag) and the enhancement of surface diffusion by magnesia, opinions were reversed as new studies appeared [18]. Only mechanism 1 was completely ruled out; this by an ingenious experiment by W. C. Johnson and R. L. Coble [22] in which a two phase mixture of $MgAl_2O_4$ and Al_2O_3 was used as the source of magnesia vapor to dope an undoped alumina powder compact. By using a two-phase equilibrium mixture the thermodynamic activity of MgO is pinned at a constant value (at constant firing temperature). The undoped alumina, held at the same temperature, may be doped by the magnesia vapor up to, but not in excess of, the solid solution concentration limit. Thus the supersaturation of magnesia necessary to precipitate spinel particles cannot occur in this experiment. Johnson and Coble nonetheless observed the same dense, equiaxed microstructure characteristic of Lucalox in the surface of their alumina sample, while the undoped interior showed the usual abnormal grain growth and entrapped porosity. This clever experiment proved that a second phase was not necessary to achieve theoretical densities.

The current understanding is that mechanisms 2-5 are all to some degree influenced by magnesia additions. The single most affected parameter seems to be the grain boundary mobility [23]. From considerations of simultaneous densification and grain growth, it appears that while the measured changes in surface diffusivity or densification rate are by themselves not sufficient for the avoidance of pore-boundary separation, the combined effects of a slight increase in the densification rate and pore mobility (factors of 3-4) and a substantial decrease in grain boundary mobility (by a factor of 25 or more) are adequate [24].

It is also recognized that an important role of magnesia is to lessen anisotropies in surface and grain boundary energies and mobilities. Pore entrapment does not require the separation of pores uniformly from all boundaries; a few high mobility grain boundaries can lead to local pore separation and discontinuous grain growth. Magnesia has been found to narrow the distribution of dihedral angles at the alumina free surface [24] reflecting a homogenization of surface energies, and/or grain boundary energies, which should reduce the local variation in pore and grain boundary velocity.

In 1999 Gavrilov et al. [26] made an extensive work by scanning secondary ion mass spectrometry (SIMS) to investigate the distributions of SiO_2 and MgO in sintered alumina. They showed that when alumina codoped both with SiO_2 and MgO, segregation of both ions to grain boundaries is reduced by a factor of 5 or more over single doping. Then it was concluded that codoping with SiO_2 and MgO additives increases the bulk solubility in alumina and decreases their interfacial segregation over single doping. According to their results the beneficial effect of MgO additions in controlling microstructure development in alumina based on the ability of MgO in redistributing silicon ions from grain boundaries into the bulk.

Besides the dramatic effects of MgO on the sintering behavior and microstructure of alumina, it was discovered that doping of rare earth elements such as yttrium and lanthanum has a tremendous influence on the microstructure and creep properties of the ceramic [31-38]. The beneficial effect of yttrium in alumina is closely related to the segregation and/or precipitation behavior of the dopant.

Gülgün [31] and Wang et al. [32] showed that yttrium segregates to the grain boundaries of alumina in three distinct regimes: (1) dilute or saturated; (2) supersaturated; (3) equilibrium with YAG precipitates. Gülgün et al. modeled the adsorption of yttrium to grain boundaries by using a simple McLean-Langmuir type adsorption isotherm in the dilute regime. At very low yttrium content they calculated the yttrium excess at the grain boundary according to

$$\Gamma \approx X_t / S_v \Omega = X_t G / 3\Omega \qquad (1.9)$$

where Γ is the planar density of yttrium at the boundary, X_t is the total concentration of dopant ion, S_v is the total grain boundary area per unit volume, Ω is the volume per cation in α-alumina (0.0212 nm^3/cat), and G is the grain size. In the supersaturation regime a noticeable deviation from this isotherm was observed and the grain boundary excess reached a maximum of 9 yttrium cation/nm^2. This supersaturation prior to precipitation was linked to a nucleation barrier for YAG precipitate formation. In the third regime Y-excess concentration at the grain boundaries settled down at a constant value of about 6-7 yttrium cation/nm^2 accompanied by the precipitation of YAG.

Gülgün and Voytovych et al. [35, 36] also investigated the effects of yttrium doping on the densification and grain growth of α-alumina. It was observed that the samples had a bimodal grain size distribution that was strongly correlated to the frequency and distribution of $Y_3Al_5O_{12}$ (YAG) precipitates in the microstructure [35]. It was also shown that yttrium doping inhibited densification and coarsening at 1450^0C, but had very little effect at 1550^0C and no effect at 1650^0C. The change in densification behavior was suggested to be related to the transition with increasing temperature from grain boundary diffusion to lattice diffusion controlled densification [36].

2. EXPERIMENTAL PROCEDURE

Samples with various amounts of calcium doping were prepared from ultrapure α-Al_2O_3 powders by pressing them prior to sintering. After chemical analysis sintered samples were cut in half perpendicular to the axial direction and inner surfaces were polished for analysis. Microstructural analysis was performed by a scanning electron microscope (SEM).

2.1. Materials

One of the main objectives of this study was to prepare alumina ceramic with a closely controlled chemistry. The aim was to have only controlled amounts of calcium as the only detectable and insoluble impurity in the polycrystalline material. To this purpose, very high purity starting materials were used in the experiments. The starting powder was ultra-high purity AKP 500 α-Al_2O_3 (Sumitomo Chemical Company, Ltd., Osaka, Japan). Calcium doping was achieved by the addition of ACS grade $Ca(NO_3)_2.4H_2O$ (MERCK). In order to disperse and dope the powders homogeneously, ACS grade 2-propanol (J.T. Baker) were used as the mixing media. During the uniaxial pressing of powders, hardened steel die was lubricated with pure liquid paraffin (Atabay Kimya, Istanbul, Turkey) to avoid sticking of powders to die surfaces. Initial chemical compositions of the chemicals used are given in Tables 2.1-2.3 as reported by the manufacturers.

Pure alumina milling balls (99.7%, Friatec, Germany) and agate mortar and pestle were used for milling and grinding the powders, respectively. The green compacts were sintered inside high purity alumina crucibles (Halden-Wanger, Germany)

Table 2.1. High purity alumina "AKP-500" (Al_2O_3) analytical data
Sumitomo Chemical Company, Ltd.

B.E.T. Specific Surface Area	12.3 m^2/g
Loose Bulk Density	0.7 g/cm^3
Tapped Bulk Density	1.1 g/cm^3
Impurity Analysis	
Fe	8 ppm
Si	8 ppm
Cu	< 1 ppm

Table 2.2. Calcium nitrate tetrahydrate ($Ca(NO_3)_2.4H_2O$) analytical data
MERCK, GR for analysis, ACS

Assay (complexometric)	99.0-103.0%
Insoluble matter and precipitate by Ammonium Hydroxide	max 0.005 %
pH-value (5%;water)	5.0-7.0
Chloride (Cl)	max 0.002%
Nitrite (NO_2)	max 0.001%
Sulphate (SO_4)	max 0.002%
Heavy Metals (as Pb)	max 0.0005%
Barium (Ba)	max 0.005%
Copper (Cu)	max 0.0002%
Iron (Fe)	max 0.0005%
Potassium (K)	max 0.005%
Magnesium (Mg)	max 0.01%
Sodium (Na)	max 0.01%
Lead (Pb)	max 0.0002%
Strontium (Sr)	max 0.01 %
Magnesium and Alcali Salts (as sulphate)	max 0.2%

Table 2.3. 2-propanol ($CH_3CHOHCH_3$) analytical data
J.T. BAKER, Baker analyzed, ACS

Assay	min 99.5%
Color (APHA)	max 10
Residue after Evaporation	max 0.001%
Solubility in Water	passes test
Titrable Acid or Base (meq/g)	max 0.0001
Water (H_2O)	max 0.1%
Trace Impurities (in ppm)	
Al (Aluminium)	max 0.5
Ba (Barium)	max 0.1
B (Boron)	max 0.02
Cadmium (Cd)	max 0.05
Calcium (Ca)	max 0.5
Chromium (Cr)	max 0.02
Cobalt (Co)	max 0.02
Copper (Cu)	max 0.02
Iron (Fe)	max 0.1
Lead (Pb)	max 0.1
Magnesium (Mg)	max 0.1
Manganese (Mn)	max 0.02
Nickel (Ni)	max 0.02
Tin (Sn)	max 0.1
Zinc (Zn)	max 0.1

2.2. Sample Production

2.2.1. Preparation of the Green Bodies

Necessary calculations were performed in order to dope 100 grams of alumina with 10, 20, 30, 50, 100, 200, 500 and 1000 ppm calcium. All calculations were based on calcium/alumina ratio in weight ppm as shown:

$\text{MW}_{\text{Ca(NO3)2.4H2O}}$=236.15 gr/mole

To dope 10 ppm Ca in the 100 gr of Al_2O_3*:*

$$\begin{array}{rr} 236.15 \text{ gr } Ca(NO_3)_2.4H_2O & 40.08 \text{ gr Ca} \\ \chi \text{ gr } Ca(NO_3)_2.4H_2O & 10/100\times10^6 \text{ gr Ca} \\ \hline \multicolumn{2}{c}{\chi = 5.892 \times 10^{-3} \text{ gr}} \end{array}$$

For each calcium doping level, 100 grams of Al_2O_3 powder and calculated amount of $Ca(NO_3)_2.4H_2O$ were weighed with a high precision balance (+0.0001gr) and put in a pre-cleaned 1-l HDPE bottle. 2-propanol was poured into the bottle until the half of it became filled. After putting approximately half a kilogram of alumina balls into the bottles, the lids were closed and sealed with first teflon and then with parafilm. Powders were milled inside these bottles for 12 hours.

After ball milling, calcium doped alumina slurries were poured into several small evaporating dishes and dried in the low temperature furnace at 60^0C (Memmert). It took about 24 hours to dry the powders. Dried powders were slightly crashed into small pieces and stored the pre-cleaned small HDPE sealed bottles.

In order to reach higher densities after sintering, powders were ground into smaller particle sizes in an agate mortar. From each calcium doping level, 6 pellets each weighing around 1.5 grams were pressed. For comparison undoped powders were also subjected to the same procedures as the doped ones. At this stage powders were sent to chemical analysis.

Ground powders were uni-axially pressed in a hardened steel die at 28 MPa for 1 minute (Marmara Makine Sanayi, Istanbul, Turkey). The green compacts were discs of 13 mm in diameter. During pressing to avoid sticking of powders and pressed samples to the die, paraffin liquid was used as a lubricant.

Cold isostatic pressing of the samples were performed at the Department of Ceramic Engineering, Anadolu University, Eskisehir. Samples were put inside the fingers of powder free latex gloves and then inserted in the high pressure resistant qualetex balloons (Aldrich). The pressure balloons were evacuated with a vacuum pump before pressing. Samples were isostatically pressed at 250 MPa for 1 minute.

2.2.2. Sintering

A new high temperature furnace was bought and only used for sintering the samples of this research (Thermal Technologies, Tel Aviv, Israel). In order to define a proper heating schedule during sintering, thermal analysis of 100 ppm calcium doped powders was done from room temperature to 1400^0C. According to the result of this analysis, the following temperature program of the furnace as given in Table 2.4 was used.

Table 2.4. Temperature program of sintering

Temperature Range	Heating Rate	Duration
40^0C-800^0C	5^0C/min	
@800^0C		6 hours
800^0C-1100^0C	10^0C/min	
@1100^0C		2 hours
1100^0C-Sintering T	10^0C/min	
@ Sintering T		1, 2 and 12 hours

Pressureless sintering was performed at 1400^0C, 1500^0C and 1600^0C under air atmosphere using $MoSi_2$ heating elements. In order to protect the samples from impurities such as Si, they were embedded into their native powders in high purity alumina crucibles. At 1400^0C and 1600^0C pellets were sintered for 1 hour and at 1500^0C samples were sintered for 1 and 12 hours.

2.3. Sample Characterization

2.3.1. Density Measurement

Densities of the samples were measured by Archimedes' method using distilled water. The details of the density measurement were given in Appendix A.2.

2.3.2. Chemical Analysis

Bulk chemical analyses of the powders were done by inductively coupled plasma-optical emission spectroscopy (ICP-OES) (Perkin Elmer) before and after sintering. Powders were sent to three independent laboratories for chemical analysis but the results did not confirm each other and only one could explain the variation in the microstructures. All same powders were sent to SISECAM Analytical Chemistry Analysis Laboratories. The accuracy and repeatability of the results were quite satisfactory (Table 3.1). Maximum silicon content were determined by using the blue indicator color of molybdenum containing compounds of silicon.

2.3.3. Microstructural Analysis

All the sintered samples have to be polished and etched before microstructural analysis. The samples were cut in half perpendicular to the axial direction with a low speed diamond saw (Metkon, Bursa, Turkey). Due to the risk of Si contamination at the outer surfaces during sintering, only inner surfaces of the samples were polished. Polishing was performed in two steps using an automatic polisher (Metkon, Bursa, Turkey). First SiC emery papers with various grit sizes (120, 240, 400, 600, 1000, and

1200) and then diamond pastes with 9, 6, 3, 1 and 0.25μ grain sizes were used. The method that was employed for polishing is given in Table 2.5

Table 2.5. Polishing method

	Step 1	**Step 2**
Abrasive	SiC	Diamond paste
Grit / Grain Size	120C, 240C, 400C, 600C, 1000C, 1200C	9μ, 6μ, 3μ, 1μ, 0.25μ
Lubricant	Water	Diamond lubricant (METKON)
Speed (rpm)	300	150

After polishing, samples were thermally etched to reveal the grain boundaries. Samples that were sintered at 1500^0C and 1600^0C were etched at 1400^0C and samples that were sintered at 1400^0C were etched at 1300^0C for 8 hours inside the covered alumina crucibles.

All samples were cleaned with 2-propanol in an ultrasonic cleaner before mounting them on the specimen stage. Double-sticking adhesive carbon tapes were used to stick the samples to the SEM stubs and the upper surfaces of the samples were linked to the conductive stubs by carbon dag suspension. In order to avoid charging during SEM analysis carbon coating was done by a sputter coater (Bio-Rad, England) using carbon filaments.

Microstructural analysis were carried out by SEM (JSM 840A, JEOL, Tokyo Japan) at BRISA and X-ray spectral measurements were done by an attached EDS system (Oxford Link, England). All the micrographs were taken at 10 KV and 8 mm working distance. From each individual samples several micrographs were taken at various magnifications (1 kX, 3 kX, and 5 kX) for 1500^0C and 1600^0C sintered samples and additional 9 kX for samples sintered at 1400^0C to see the overall morphology. Grain sizes were accurately measured from the micrographs in all samples. Particles/grains with a possible precipitate morphology were analyzed for their chemistry using the EDS. Back scattered electron imaging were used to detect possible second phase precipitates or pockets.

2.3.3.1. Grain size measurement

Grain size was measured by determining the number of grains (or grain boundaries) that intersect a given length of randomly oriented straight line. Most grain size measurements invoke assumptions relative to the shape and size distribution of the grains [4].

Measurement of the grain boundary area per unit volume S_V (total grain boundary area) is a useful parameter. S_V can be calculated without assumptions concerning grain shape and size distribution from measurements of the mean number of intercepts of random test lines with grain boundaries per unit length of test line N_L.

$$S_V = 2N_L \qquad (2.1)$$

If a mean grain diameter D is required from S_V, this can be obtained by assuming constant-size spherical grains and noting that each grain boundary is shared by two adjacent grains [4]

$$2S_V=(4\pi\,(D/2)^2)\,/\,(4\pi\,/3\,(D/2)^3) \qquad (2.2)$$

or

$$D=3/S_V=3/(2N_L) \qquad (2.3)$$

In summary, this method is known as grain size measurement by the mean linear intercept method. Mean linear intercept length, $\overline{L}$, is the length of the line divided by the average number of grains intersected. Therefore,

$$\overline{L}=1/N_L \qquad (2.4)$$

$$\text{Grain Size (G)} = D = 1.5\ \overline{L} = 3/S_V \qquad (2.5)$$

All the grain size calculations were done according to this method in this thesis.

3. RESULTS & DISCUSSION

3.1. Chemistry

One of the major accomplishments of this study is to dope alumina powders with controlled amounts of calcium without any significant amounts of co-doping or any other contamination. After the preparation of the calcium doped alumina powders, bulk chemical analysis of the powders were done by ICP-OES. The results of the analysis are shown in Table 3.1.

Table 3.1. ICP-OES results of the samples before sintering

Doping Level	**Ca (µg/g)**	**Si (µg/g)**[*]
Undoped	0	< 5
10 ppm	7.1	< 5
20 ppm	10.8	< 5
30 ppm	9.7	< 5
50 ppm	23	< 5
100 ppm	60	< 5
200 ppm	133	< 5
500 ppm	344	< 5
1000 ppm	650	< 5

[*] *Detection limit of the instrument*

In this table the left column contains the intended amounts of calcium doping. In the central column the actual experimentally determined amounts of calcium concentrations present in the powders are shown. Although the reason is not clear, all the measured calcium levels are less than intended. The trends in the observed microstructures confirmed the results of chemical analysis, thus, all the calculations and comparisons are based on the experimentally determined concentrations. The bulk concentrations of calcium present in 20 and 30 ppm doped samples were approximately equal and SEM analysis of these samples revealed almost identical microstructures at the end of each heat treatment. Therefore, only one sample that contained 10.8 ppm calcium was discussed further. The right column exhibits the bulk concentration of silicon contamination which is estimated to be less than 5 ppm for all doping levels. A molybdenum blue indicator method was used with samples that were intentionally doped with 5 ppm silicon. Those intentionally 5 ppm silicon doped specimens showed blue color although the powders prepared in this study did not show any coloration. From these data it was concluded that the samples were prepared with a very closely controlled chemistry.

3.2. Densification

Densities of the sintered samples were measured by Archimedes' method as described in Appendix A.2.

%TD of the samples were given in Table 3.2. for different sintering temperatures and calcium contents.

Table 3.2. Densities of the samples

	1400^0C, 1h (%TD)	**1500^0C, 1h (%TD)**	**1500^0C, 12 h (%TD)**	**1600^0C, 1h (%TD)**
Undoped	96,68	97,86	98,45	98,34
7.1 ppm	96,57	96,58	98,11	98,06
10.8 ppm	96,83	97,26	98,31	98,26
23 ppm	96,09	97,57	98,40	98,08
60 ppm	95,40	97,79	98,63	98,31
133 ppm	96,33	97,85	98,38	98,19
344 ppm	97,69	98,56	98,36	98,47
650 ppm	97,66	97,66	97,91	97,77

In order to observe the densification behavior of the samples clearly, %TD of the samples were plotted as a function of sintering temperature.

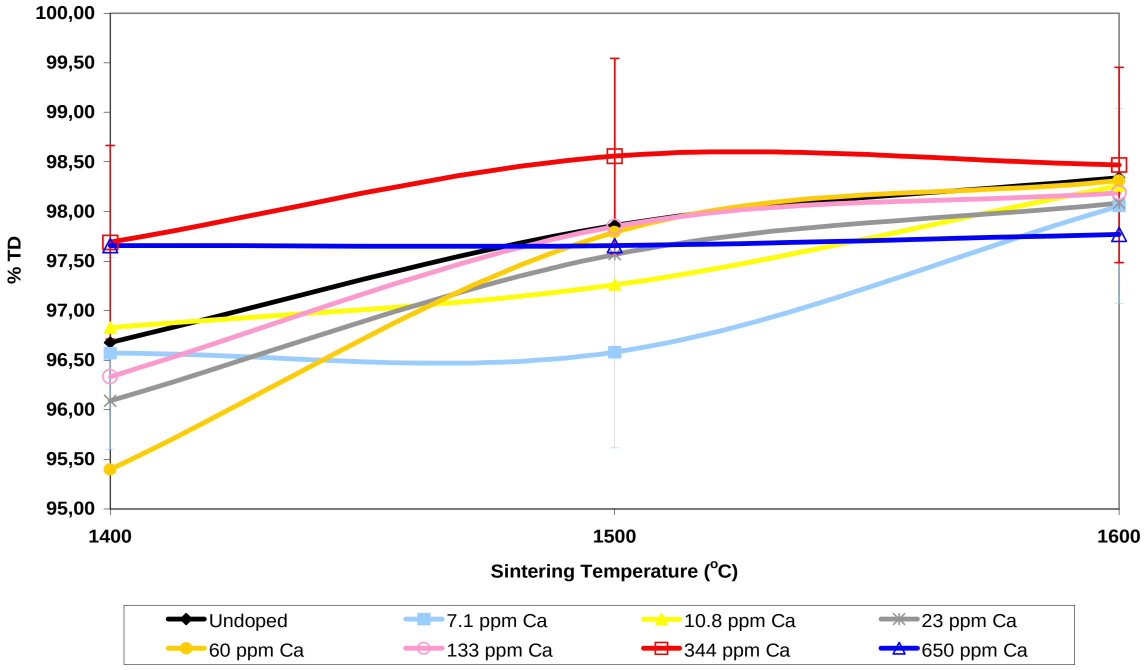

Figure 3.1. Densification of the samples as a function of sintering temperature

As can be seen from the graph almost all the samples with various doping levels densified slightly by increasing the sintering temperature. The variation observed in the densification behavior of 7.1 ppm calcium doped sample was within the limit of 1% experimental error. No noticeable change was observed in the densification behavior of 650 ppm calcium containing sample by increasing temperature.

It was not possible to reach 100% density in these samples during sintering. All densities varied between 96.5% to 98.5% theoretical density of α-alumina (3.986 gr/cm^3). Several facts about the ultraclean processing of the samples can be listed as possible reasons for relatively low final densities:

(i) The powders were ultra pure and no sintering aids were added to the powders. Thus, liquid phase sintering to enhance densification was not employed in this study.

(ii) In order to avoid the further contamination of the powders, no lubricants were used to facilitate particle packing. Most of the commercially available organic lubricants contain silicon impurities. Only pure liquid paraffin was used to lubricate the die walls during uniaxial pressing.

(iii) The pressure of the cold isostatic pressing was not high enough to pack the "dry" compacts to higher green densities before sintering.

Although it is very well-known that porosity can affect the microstructural development dramatically, the results that are reported in this thesis are considered as a comparison between the microstructures of the samples with various calcium doping levels for a specific sintering temperature and time. Other parameters in all of the experiments such as the amount of porosity for all samples after sintering were approximately same. Therefore, the presence of ~3% porosity did not receive a special emphasis while discussing the results. However, the absolute grain growth rates may have been reduced by the presence of that much porosity. The pore surfaces may have been locations where excess calcium could be accumulated. However, X-ray mapping affords with EDS/SEM could not confirm this suspicion. Finer scale detailed TEM analysis is necessary to clarify this point.

3.3. Microstructural Evolution

The microstructural characterization of the samples was carried out by scanning electron microscope (SEM). In order not to miss crucial information about the microstructure, samples were observed at low (~1000X) and medium range (3000X-9000X) magnifications. The micrographs shown in this section are truly representative of the actual microstructures in the samples. Some of these representative micrographs are given in Figures 3.2.-3.17. With the help of these micrographs, average grain sizes of the samples were calculated by using mean linear intercept method as described in Section 2.3.3.1 and an example is shown in Appendix A.1a. More than 400 grains in 3-4 micrographs were counted for each sample and the mean linear intercept lengths were multiplied by 1.5 to find the average grain sizes. The average grain sizes of the samples are given in Table 3.3.

Table 3.3. Average grain sizes of the samples

	1400^{0}C 1h			**1500^{0}C 1h**			**1500^{0}C 12h**			**1600^{0}C 1h**		
	Av. G of Small Grains	***Av. G***	***Av. G of Large Grains***	***Av. G of Small Grains***	***Av. G***	***Av. G of Large Grains***	***Av. G of Small Grains***	***Av. G***	***Av. G of Large Grains***	***Av. G of Small Grains***	***Av. G***	***Av. G of Large Grains***
0 ppm	-	0,90±0,02	-	-	2,14±0,07	-	-	2,76±0,1	-	-	2,90±0,07	-
7,1 ppm	-	0,93±0,02	-	-	1,74±0,05	-	-	2,52±0,08	-	-	2,95±0,07	-
10,8 ppm	-	0,89±0,02	-	-	1,73±0,05	-	-	2,46±0,07	-	-	2,89±0,07	-
23 ppm	-	0,85±0,01	-	-	1,74±0,06	-	-	2,53±0,09	-	-	2,60±0,06	-
60 ppm	-	0,73±0,01	-	-	1,65±0,05	-	-	2,53±0,09	-	-	2,70±0,06	-
133 ppm	-	0,71±0,01	-	-	1,68±0,02	-	1,53±0,09	3,03±0,11	6,82±0,38	1,56±0,09	3,04±0,09	8,42±0,46
344 ppm	-	0,81±0,01	-	1,26±0,05	2,74±0,09	7,61±0,32	1,58±0,08	3,27±0,14	7,89±0,43	2,03±0,11	4,79±0,22	9,84±0,74
650 ppm	-	0,87±0,01	-	1,26±0,09	2,36±0,05	6,91±0,34	1,54±0,05	3,02±0,11	7,31±0,58	1,65±0,09	3,63±0,17	6,43±0,82

For the samples that showed significant abnormal grain growth, it is important to report more information in addition to the overall average grain size. For this reason, Table 3.3. contains three columns for the grain sizes. In samples that showed abnormal grain growth (AGG), besides the overall average, the average size of the small grains as well as average size of the large (abnormally grown, elongated) grains are also reported. These values along with the corresponding micrographs help understand the influence of calcium segregation much better. Appendix A.1. contains the procedures that were used to determine the different average grain sizes.

It was known that most of the impurity ions such as calcium strongly segregate to grain boundaries in α-Al_2O_3. Therefore, it is believed that it is more meaningful that changes in the microstructure of alumina with the addition of calcium should be related to calcium excess at the grain boundaries instead of bulk concentrations of calcium which will be partitioned between the lattice and the grain boundaries; at least at dilute concentrations i.e. $X_t<X_t^*$

As introduced in section 1.5 segregation of calcium in polycrystalline α-alumina at least in the dilute regime can be modeled by simple adsorption isotherm of Langmuir and McLean like most of the surface active impurities with very low bulk solubility [31]. This model is based on the following equation:

$$\frac{\Gamma}{\Gamma_0 - \Gamma} = K\left(X_t - \Gamma S_v \Omega\right) \tag{3.1}$$

where Γ is the planar density of calcium at the boundary, Γ_0 is the planar density of available grain boundary sites for adsorption, K is the partition coefficient, X_t is the total atomic concentration of calcium in the sample, S_v is the total grain boundary area per unit volume, and Ω is the volume per cation in α-alumina (0.0212 nm^3/cat).

During the calculations it was assumed that the calcium coverage increases with increasing total atomic concentration of calcium in the alumina (X_t) and there were no second phase precipitate formation. Thus, most of the calcium could adsorbed at the grain boundaries without saturation and it was possible to obtain Γ_{Ca} values that would correspond to multiple layer coverage at the boundaries. Therefore, by using the approximations for the dilute concentrations:

$\Gamma_0 >> \Gamma$ and

K>>1

$$\Gamma \approx \frac{X_t}{S_v\Omega} = \frac{X_t G}{3\Omega} = \frac{X_t \overline{L}}{2\Omega} \tag{3.2}$$

where G is the grain size and $\overline{L}$ is the mean linear intercept length [31].

Gulgun et al. [31] used these approximations only for the calculations of Γ_Y at very low yttrium doping levels. However, this relation was also used for high calcium doping levels in this thesis. The main reason for this extrapolation is that the exact amounts of calcium at the grain boundaries could not be measured yet. However, the author is well aware of the possibility of precipitation of a second phase or formation amorphous triple point pocket phases. These will be discussed further in this section of the thesis. Thus, at the moment it was assumed that all calcium could be accommodated at the grain boundaries as multilayer grain boundary film without reaching the saturation point.

As mentioned previously, X_t for the samples were determined from the values determined experimentally by ICP-OES analysis. Then Γ_{Ca} values were calculated from these X_t values and measured mean linear intercepts as shown below:

AW_{Ca}=40.08 gr/mole
AW_{Al}=26.98 gr/mole
MW_{Al2O3}=101.96 gr/mole

X_t of the sample that contains 7.1 ppm (μg/g) calcium according to the chemical analysis results is:

$$X_t = \frac{\text{Ca atoms}}{\text{Al atoms}} = \frac{\dfrac{6.02\times10^{23}\ \text{Ca atoms/mole}\times 7.1\ \text{gr Ca}}{40.08\ \text{gr/mole Ca}}}{\dfrac{2\times6.02\times10^{23}\ \text{Al atoms/mole}\times10^{6}\ \text{gr Al}_2\text{O}_3}{101.96\ \text{gr/mole Al}_2\text{O}_3}} = 9.03\times10^{-6}$$

from Table 3.3 for 7.1 ppm Ca doped sample that was sintered at 1500^{0}C for 12 h:

Av. G=2,52±0,08µ

then

$$\Gamma_{\mathrm{Ca}} = \frac{\mathrm{GX_t}}{3\Omega} = \frac{2.52\times10^{3}\times9.03\times10^{-6}}{3\times2.12\times10^{-2}} = 0.358\,\mathrm{Ca/nm^2}$$

Calcium excess at the grain boundaries were calculated for all the samples and given in Table 3.4. For all calculations the overall average grain size was used as this is the true indicator of the available specific surface area for impurity segregation. In this investigations the influence of the strong anisotropy observed with high calcium excess concentration at the grain boundaries on the S_v (total grain boundary area) was not taken into account on the calculations.

Table 3.4. Calcium coverage at the grain boundaries

	Γ_{Ca} @ 1400^{0}C 1h (Ca atoms/nm^2)	**Γ_{Ca} @ 1500^{0}C 1h (Ca atoms/nm^2)**	**Γ_{Ca} @ 1500^{0}C 12h (Ca atoms/nm^2)**	**Γ_{Ca} @ 1600^{0}C 1h (Ca atoms/nm^2)**
0 ppm	0,018*	0,043*	0,055*	0,058*
7,1 ppm	0,131	0,248	0,358	0,418
10,8 ppm	0,179	0,348	0,497	0,582
23 ppm	0,390	0,801	1,167	1,197
60 ppm	0,875	1,977	3,037	3,242
133 ppm	1,891	4,455	8,051**	8,075**
344 ppm	5,553**	18,837**	22,519**	32,921**
650 ppm	11,352**	30,736**	39,229**	47,161**

* In order to plot the data for undoped samples an approximate impurity level of 1 ppm calcium was assumed and Γ_{Ca} values were calculated accordingly

** These are the samples where abnormal grain growth (AGG) was observed

3.3.1. Microstructural Evolution of the Samples Sintered at 1500^0C

In undoped and low calcium doped samples grains were equiaxed with 2 and 2.5 microns average grain sizes for sintering times 1 and 12 hours, respectively. The average grain sizes of undoped samples were approximately 10% larger than the average grain sizes of low calcium doped samples. This decrease is believed to be due to solute drag that occurs through the interaction of grain boundaries and segregated impurities. These microstructures can be seen in Figures 3.2., 3.3., 3.4. and 3.5.

It can be seen in Table 3.3.and Figures 3.2.-3.4. and 3.3.-3.5. that by increasing sintering time the grains became coarser as it was expected. However, when one tried to relate the grain sizes and morphologies to bulk calcium concentrations, no clear trends could be seen as a function of bulk calcium concentrations for different sintering conditions. For example, 133 ppm calcium doped samples had small grains when sintered at 1500^0C for 1 hour. However, another sample with same amount of calcium had large elongated grains when sintered at 1500^0C for 12 hours (Figures 3.6., 3.7). As described previously, what controlled the morphology and grain sizes were not the bulk calcium concentrations alone.

When the calcium concentration exceeded a certain limit, first the grain morphology started to change from equiaxial to elongated without any change in the average grain size. With a further increase in calcium concentration, abnormal grain growth was observed with again elongated morphology (Figures 3.6., 3.8.). However, if the calcium concentration was increased even further, average grain size decreased again when the calcium excess concentration at grain boundaries reached around $\Gamma_{Ca} \cong 20$ Ca/nm^2 (Figure 3.9.). These above mentioned phenomena will be discussed in detail in later sections of this thesis.

It was also observed that in abnormally grown samples there were regions with small grains between large grains where the average grain size was smaller than the average grain size in low calcium doped samples (Figure 3.8.). The average grain sizes of these small grain regions were seperately determined by the mean linear intercept method and were found to be around 1.5μ. The grain sizes of large grains were measured one by one as the largest dimension and then the arithmetic average was taken. Average grain sizes of large grains and small grains are also given in Table 3.3

An example for the grain size measurements in samples containing small and large grains are given in Appendix A.1b.

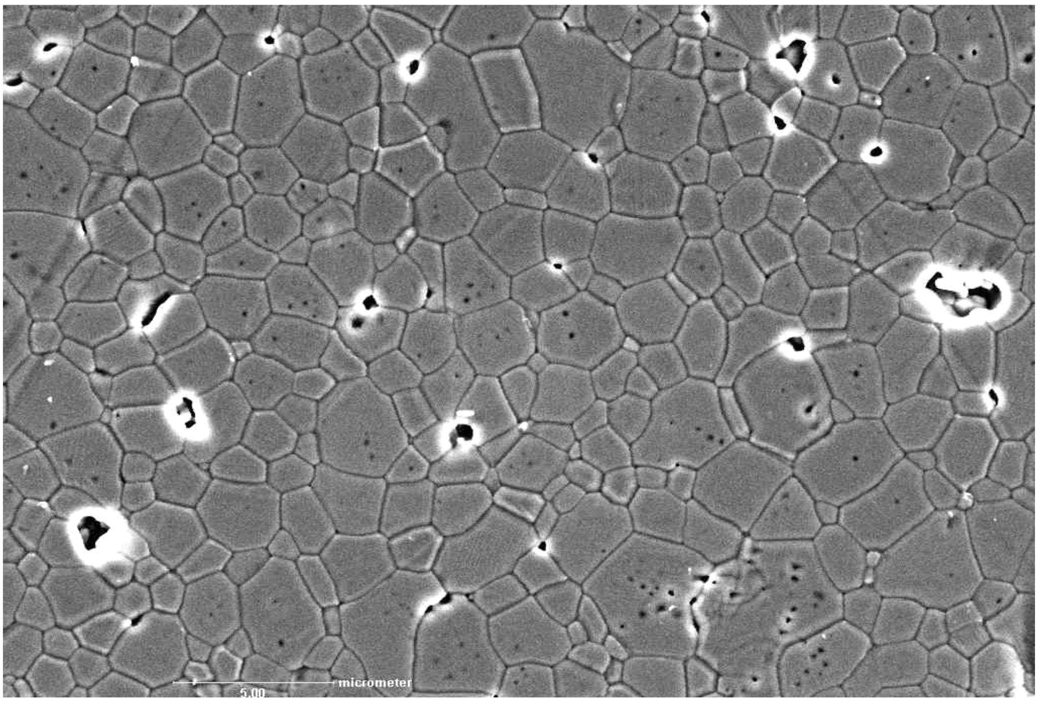

Figure 3.2. Undoped α-Al_2O_3 sintered at 1500^0C for 1 hour

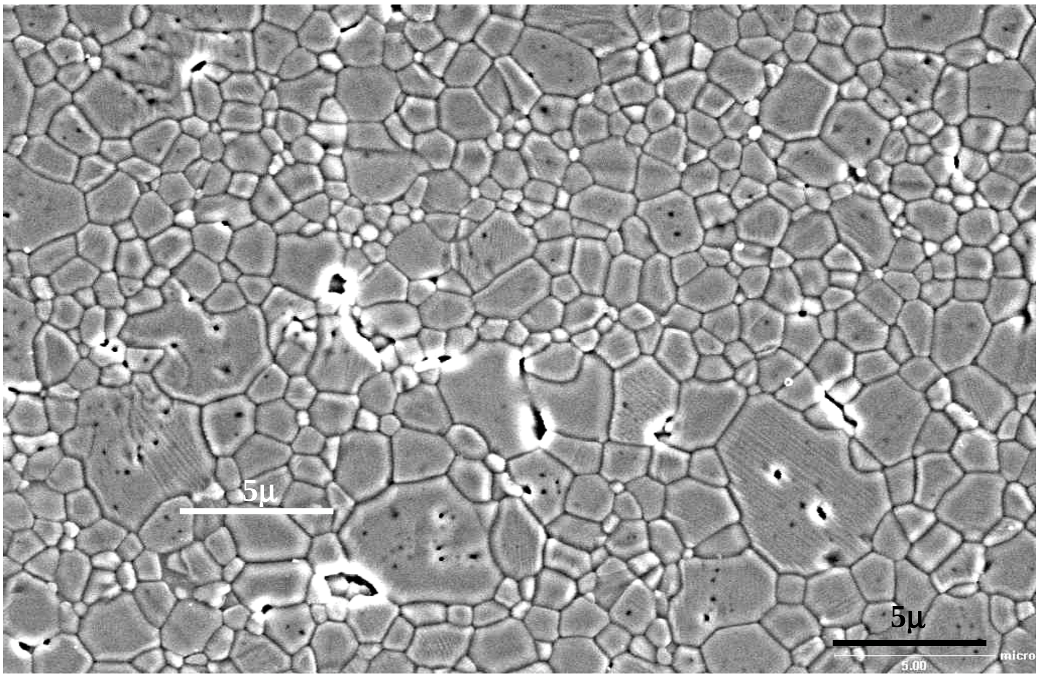

Figure 3.3. 10.8 ppm Ca doped α-Al_2O_3 sintered at 1500^0C for 1 hour

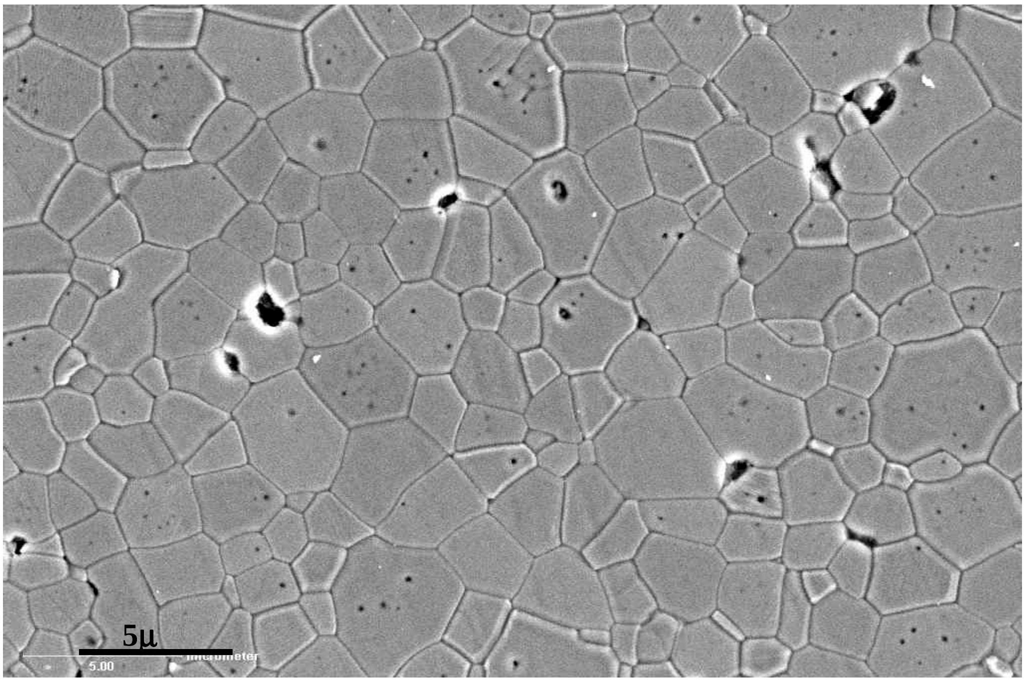

Figure 3.4. Undoped α-Al_2O_3 sintered at 1500^0 for 12 hours

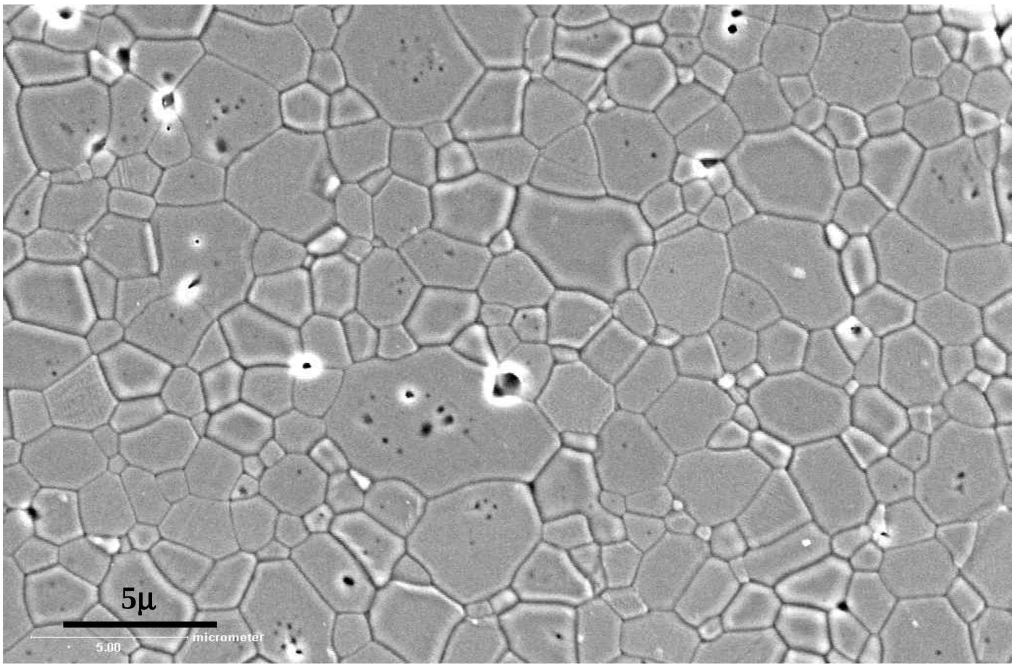

Figure 3.5. 10.8 ppm Ca doped α-Al_2O_3 sintered at 1500^0C for 12 hours

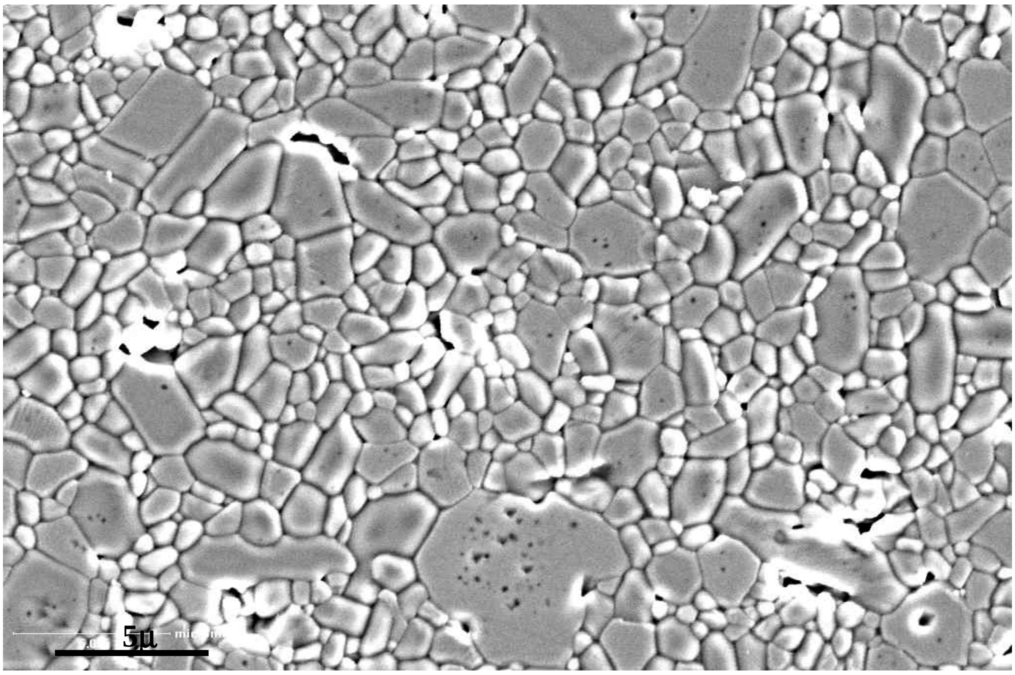

Figure 3.6. 133 ppm Ca doped Al_2O_3 sintered at 1500^0C for 1 hour

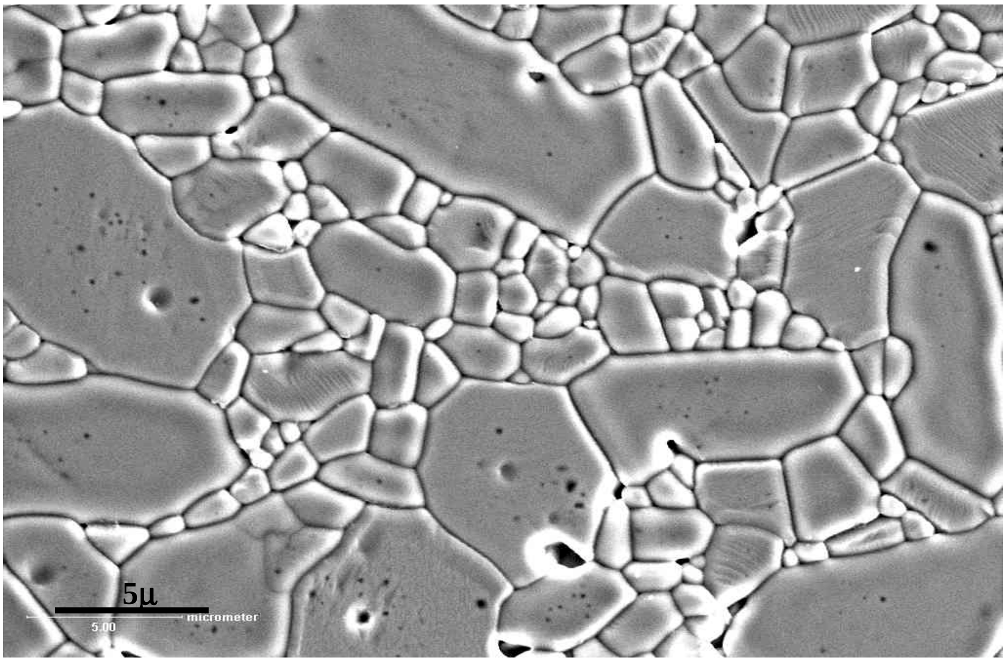

Figure 3.7. 133 ppm Ca doped Al_2O_3 sintered at 1500^0C for 12 hours

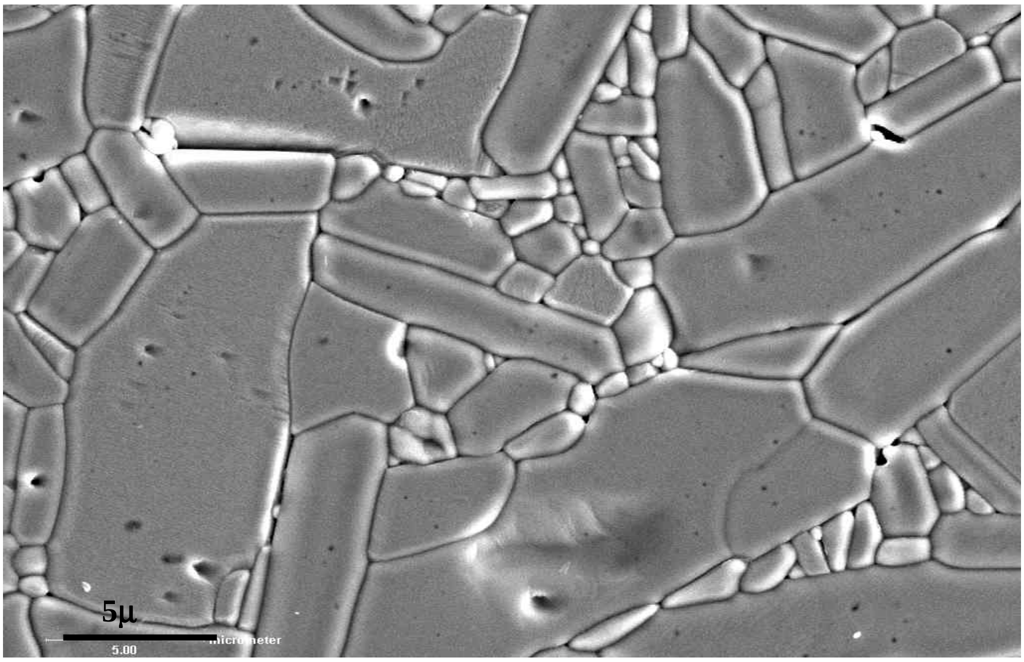

Figure 3.8. 344 ppm Ca doped α-Al_2O_3 sintered at 1500^0C for 12 hours

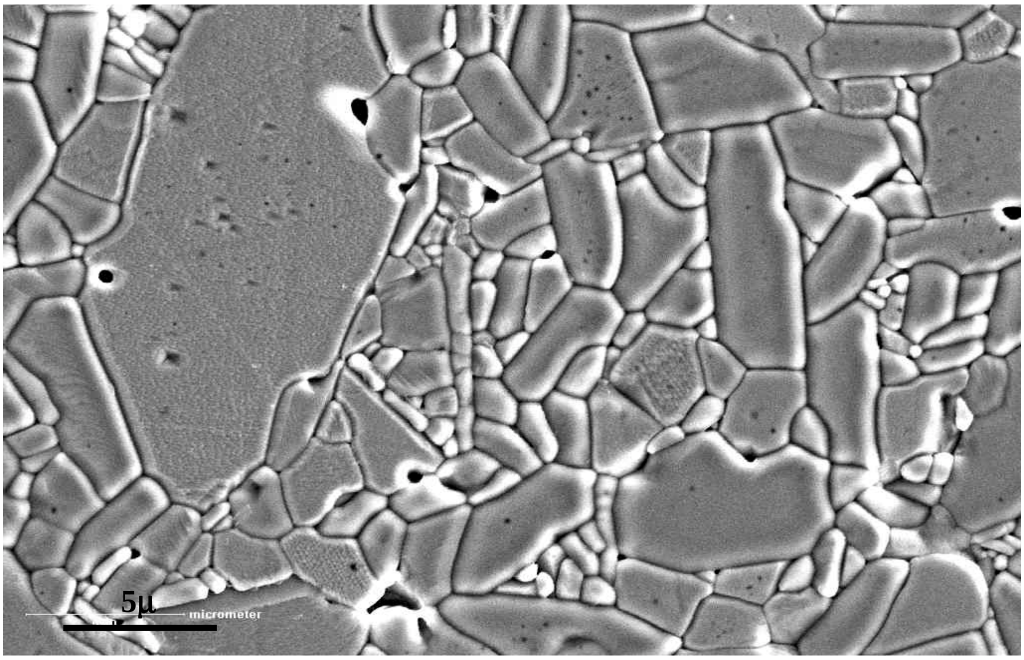

Figure 3.9. 650 ppm Ca doped α-Al_2O_3 sintered at 1500^0C for 12 hours

3.3.2. Microstructural Evolution of the Samples Sintered at 1600^0C

The samples that were sintered at 1600^0C for 1 hour, grains were equiaxed and the average grain size was around 2.9 microns for undoped and low calcium doped samples. 10% decrease in the average grain size which was suggested to be due to solute drag was first observed with 23 ppm calcium doped sample and the average grain size dropped to 2.6 microns (Figures 3.10., 3.11.).

After a critical calcium concentration grains again became elongated and abnormally grew up to an average grain size of 4.8 μ. With a further increase in the calcium dopant concentration a similar decrease in the average grain size, that was observed with samples sintered at 1500^0C, was observed when the calcium excess concentration at grain boundaries reached a value of $\Gamma_{Ca} \cong 33$ Ca/nm^2 (Figures 3.12., 3.13.).

Bimodal grain size distribution can be seen clearly in the abnormally grown samples (Figure 3.12.). The average grain size of the small grains was approximately 2.03 μ, while the average grain size of large grains was around 9.84 μ (Table 3.3.). Again the average grain size in small grain regions in AGG samples was smaller than the average grain size in equiaxed low calcium doped morphologies.

For the samples that were sintered at this temperature, the grains were coarser and a large number of pores were trapped inside the grains as shown in Figure 3.10. Thus, as described in Section 1.2. and 1.3., it is impossible to achieve 100% theoretical density in these samples unless prohibitively long sintering times were used at high temperatures.

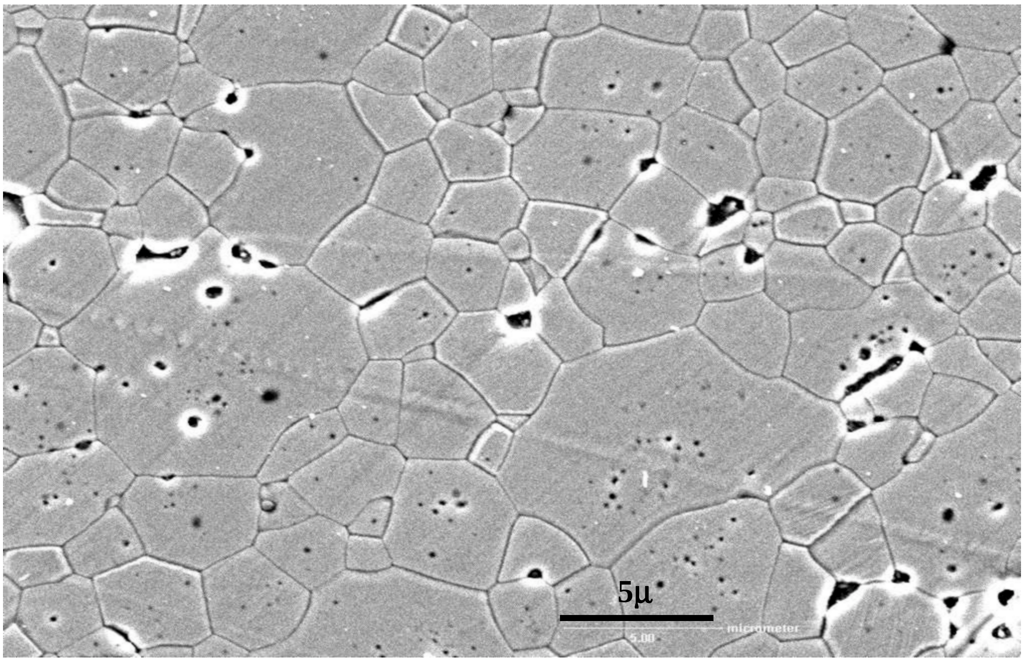

Figure 3.10. Undoped α-Al_2O_3 sintered at 1600^0C for 1 hour

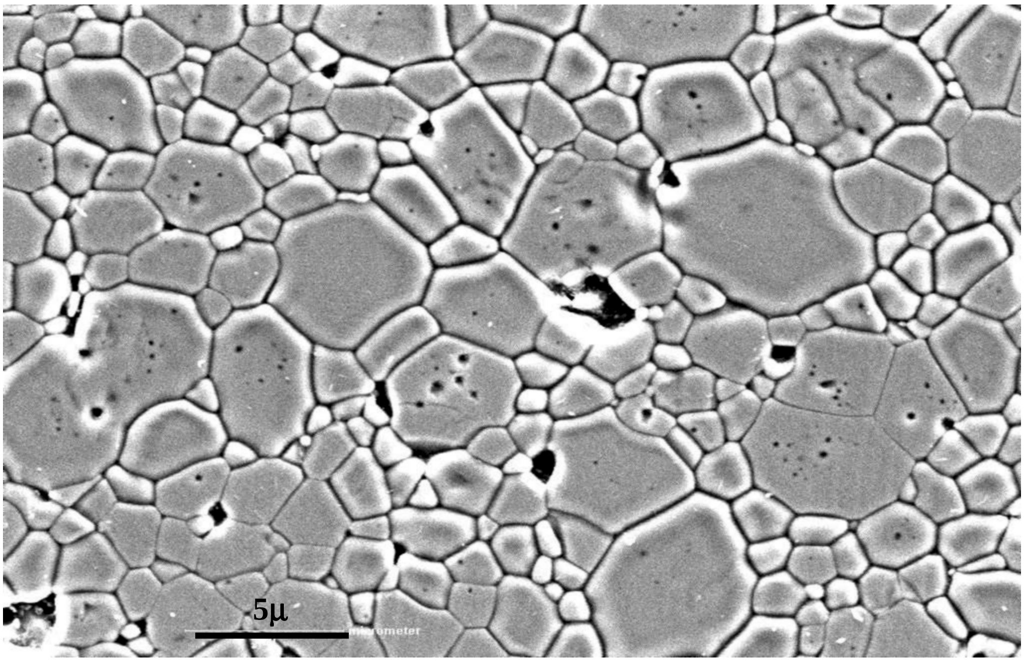

Figure 3.11. 23 ppm Ca doped α-Al_2O_3 at 1600^0C for 1 hour

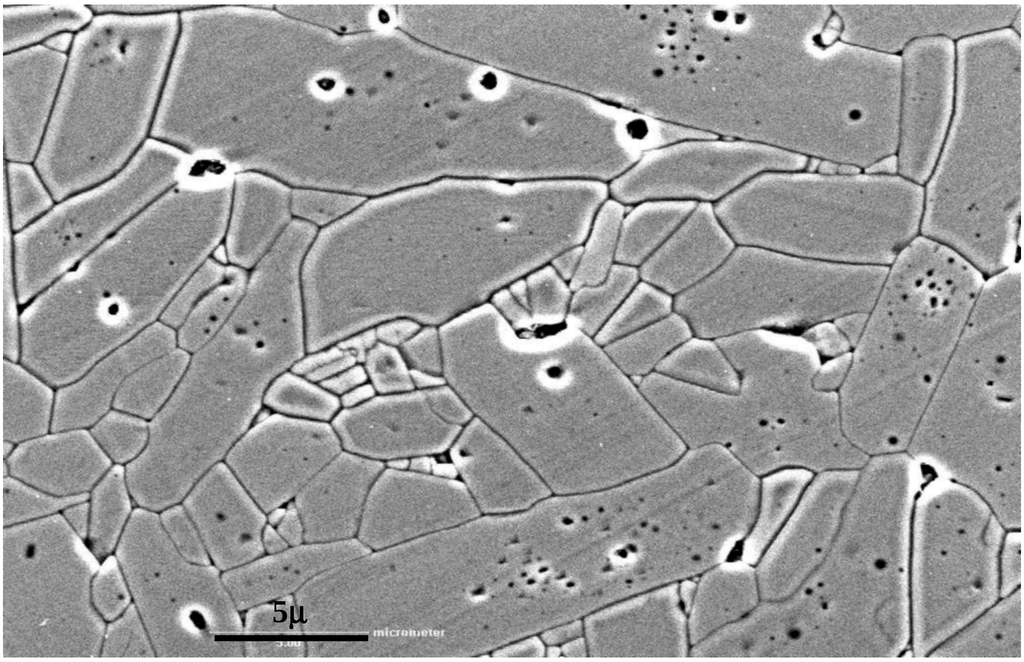

Figure 3.12. 344 ppm Ca doped α-Al_2O_3 sintered at 1600^0C for 1 hour

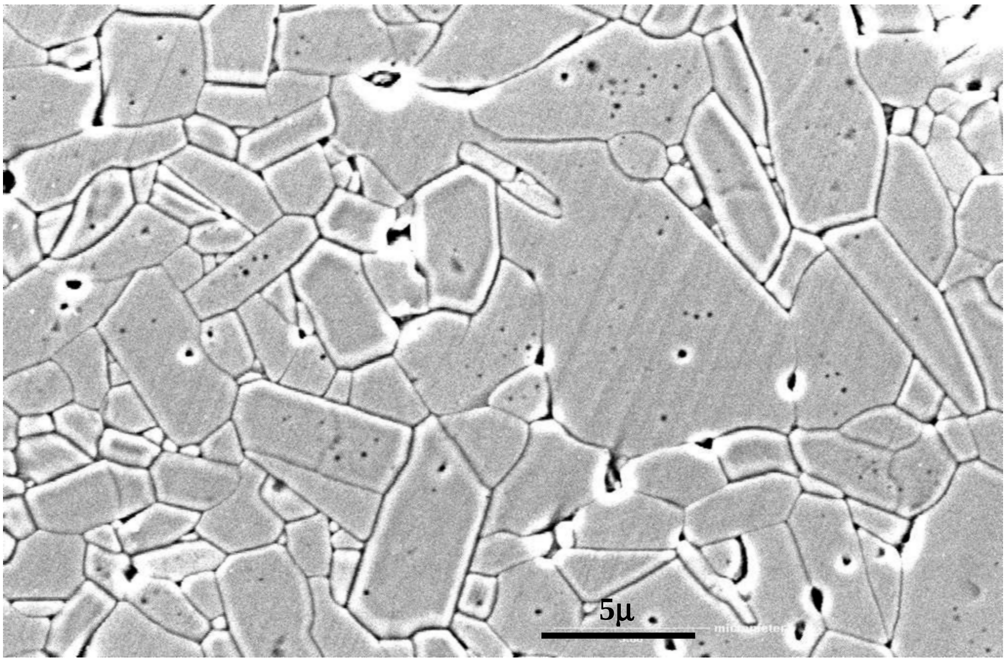

Figure 3.13. 650 ppm Ca doped α-Al_2O_3 sintered at 1600^0C for 1 hour

3.3.3. Microstructural Evolution of the Samples Sintered at 1400^0C

The microstructural evolution was rather different for the samples that were sintered at 1400^0C for 1 hour. All the samples had almost same overall average grain sizes around 0.8 microns. No significant drop in the average grain size was observed due to solute drag at low calcium doping levels (Figures 3.14., 3.15.).

Grains were mostly equiaxed up to a certain calcium doping level. When the calcium concentration at the grain boundaries reached a critical value of about 3-5 calcium atoms/nm^2 grains started to become elongated.

It was surprising to observe that although the calcium level at the grain boundaries exceeded a rather high concentration of 11 calcium atoms/nm^2 only few grains grew abnormally without any change on the average grain size (Figure3.16., 3.17.) The possible reasons for this behavior will be discussed later in this section with the results from sintering experiments at 1500^0C and 1600^0C.

In the samples sintered at 1400^0C, existence of elongated grains with facetted grain boundaries without abnormal grain growth showed that occurrence of abnormal grain growth in alumina cannot be directly correlated with the formation of facetted and straight grain boundaries as Park and Yoon claimed [15]. Although facetted and straight boundaries formed with a 3 calcium atoms/nm^2 calcium excess concentration at grain boundaries, no abnormal grain growth occurred.

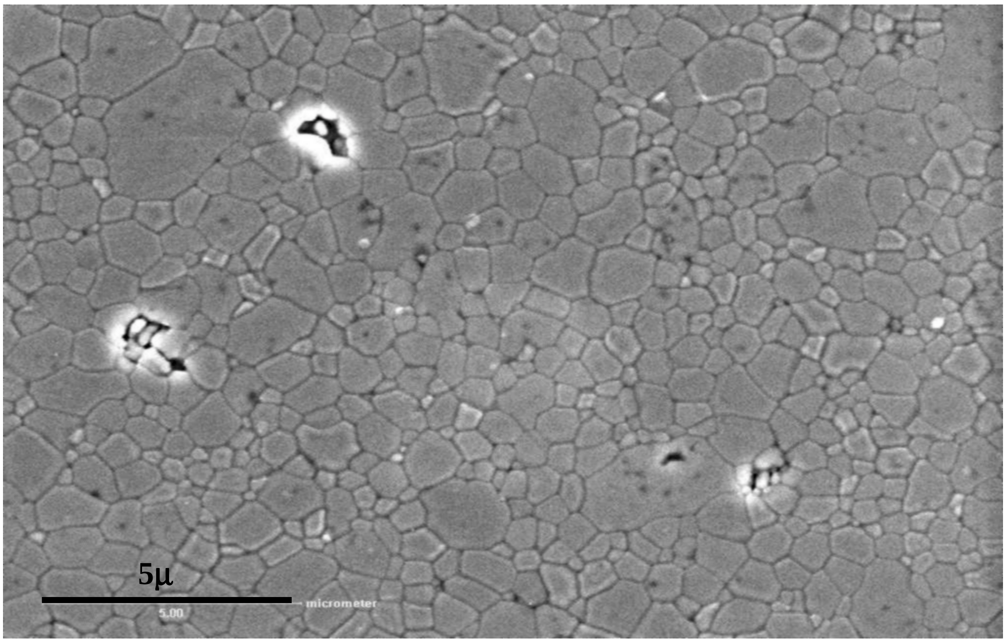

Figure 3.14. Undoped α-Al_2O_3 sintered at 1400^0C for 1 hour

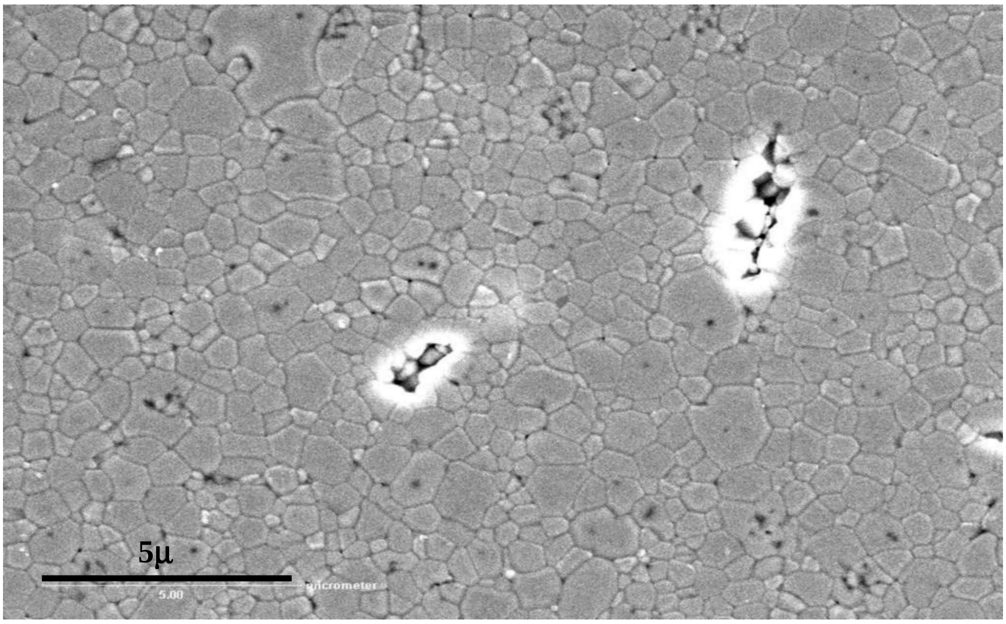

Figure 3.15. 23 ppm Ca doped α-Al_2O_3 sintered at 1400^0C for 1 hour

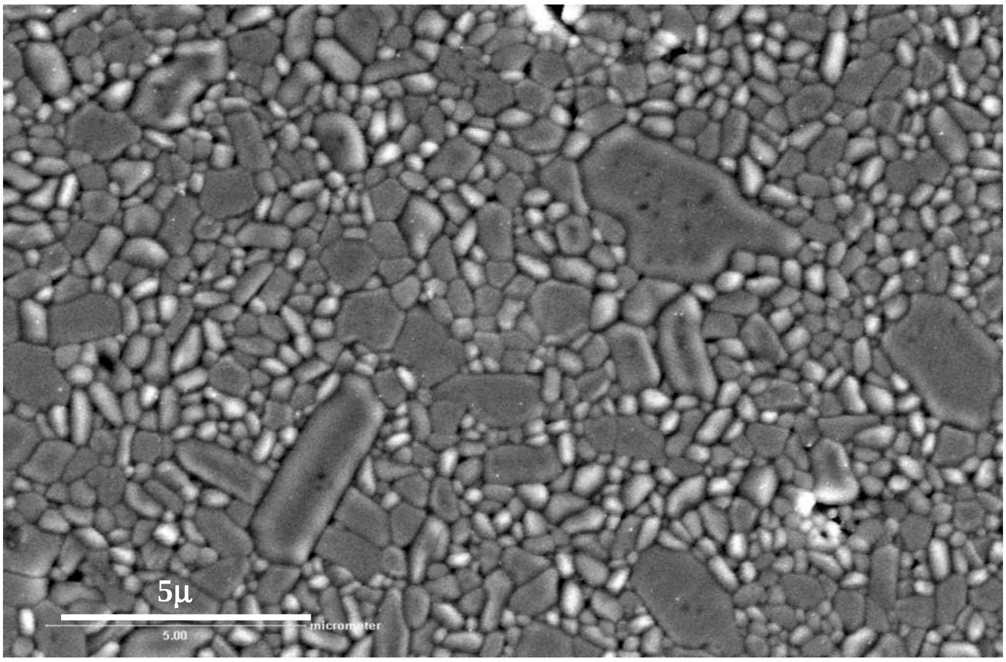

Figure 3.16. 344 ppm Ca doped α-Al_2O_3 sintered at 1400^0C for 1 hour

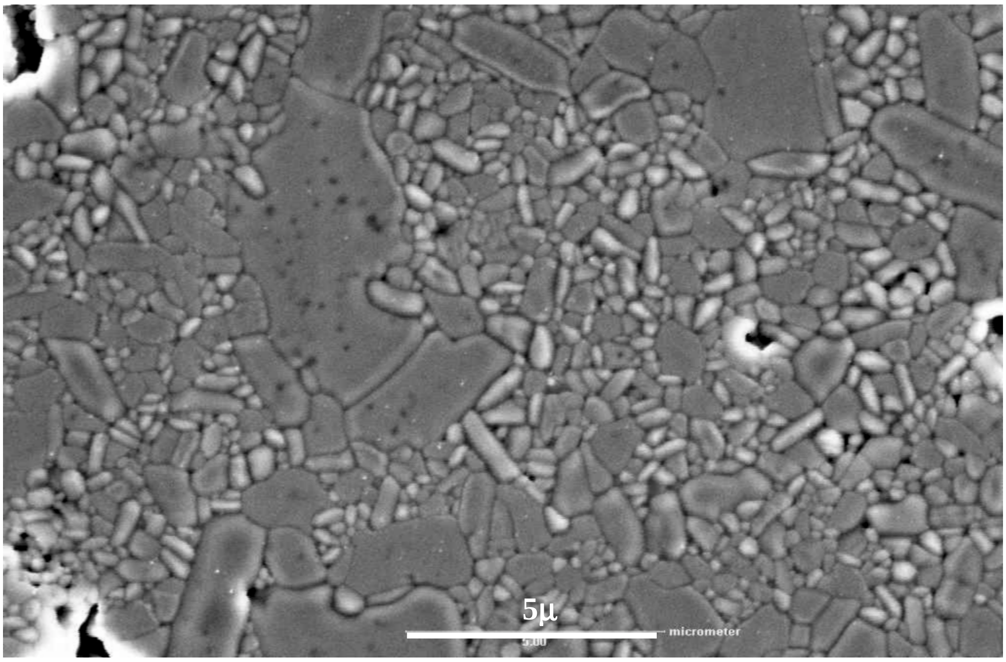

Figure 3.17. 650 ppm Ca doped α-Al_2O_3 sintered at 1400^0C for 1 hour

3.3.4. Comparisons of the Microstructural Evolution of the Samples as a Function of Sintering Temperature and Time

In order to compare the samples sintered at different temperatures and predict the critical Γ_{Ca} values where the grain size changed, grain size versus Γ_{Ca} curves were plotted (Figure 3.18.). These curves together with the micrographs were used to determine the critical calcium excess concentrations for elongated grain morphology and accelerated grain growth rate to set in.

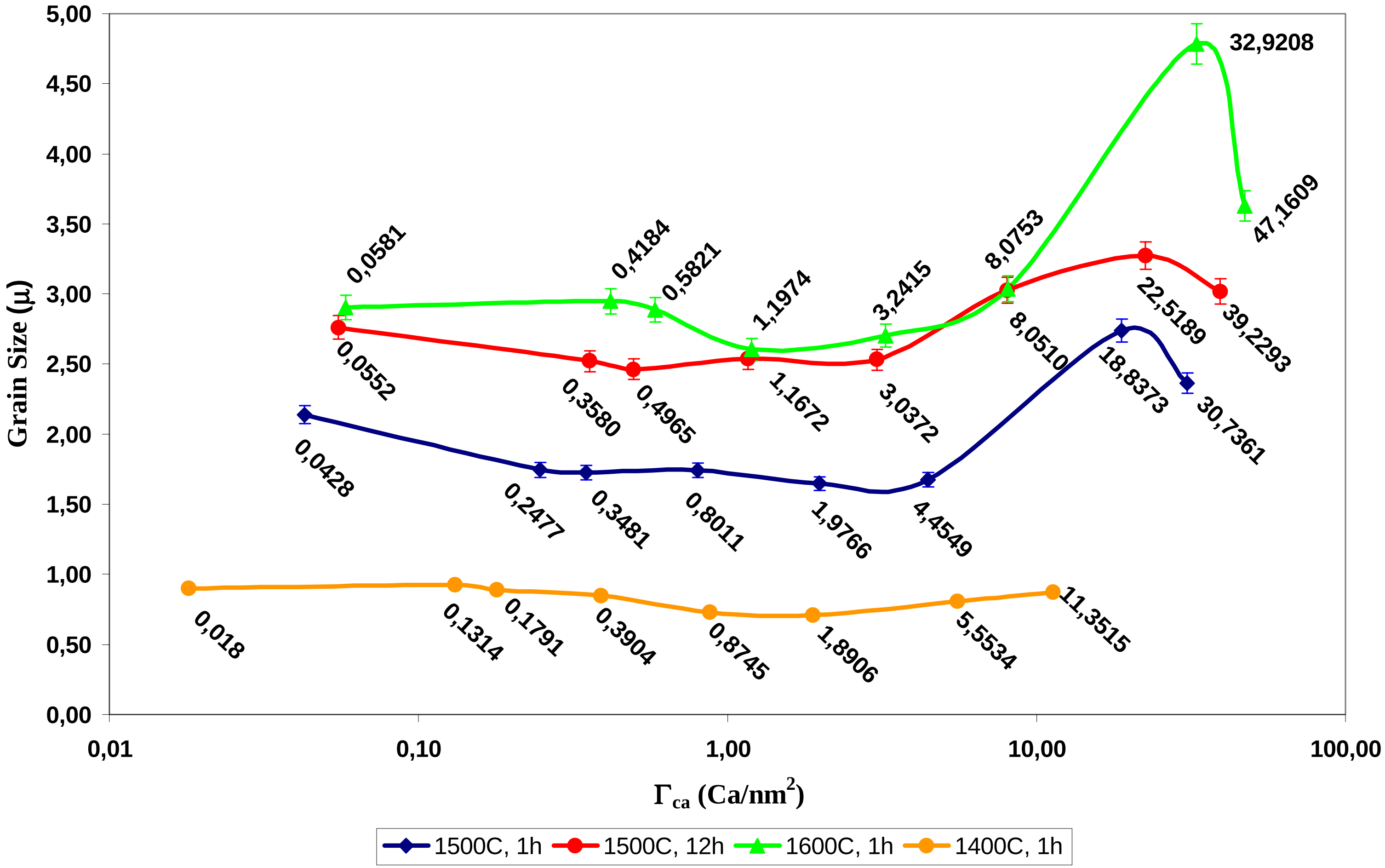

Figure 3.18. Grain size versus Γ_{Ca} semi-log plot sharing the changes in the overall average grain sizes as a function of calcium excess concentrations at the grain boundaries three different temperatures and two different sintering times at 1500^0C

When the curves in Figure 3.18. were examined from top to bottom, the green curve belongs to the set of samples sintered at 1600^0C for 1 hour. Red and blue lines are for the samples sintered at 1500^0C for 12 hours and 1 hour, respectively. Orange line at bottom of the figure represents samples sintered at 1400^0C for 1 hour. This order of the curves also confirmed that as the sintering temperature and time increased, grains became coarser. The grain size played a key role to determine the calcium segregation at the grain boundaries. Calcium concentration at the grain boundaries increased sharply as the grain size increased.

With the help of these curves and the corresponding micrographs, one of the most significant observations was that below certain calcium excess concentration depending on temperature, equiaxed, small grain morphology was obtained. Although the average grain size remained the same, when the calcium excess at the grain boundaries was around Γ_{Ca}=3 calcium atoms/nm^2 the grain morphology started to change from equaxial to elongated for all sintering temperatures (Figure 3.6.). In all these samples with elongated morphology sintered at three different temperatures, the grain sizes were 0.8, 1.6, 2.5 and 2.7μ. It was shown that the threshold Γ_{Ca} for this slab like morphology in commercial (i.e. not very pure) alumina is due to the existence of critical level of calcium in the system. If any other trace impurity (i.e. perhaps silicon) were responsible for this morphology besides calcium, for these four different grain sizes the only common denominator would not have been the 3-4 calcium atoms/nm^2 Γ_{Ca}. For example to eliminate silicon impurity as the responsible agent, it is safe to assume that all samples would have similar amounts of silicon trace impurity. Then the Γ_{Si} for 1400^0 C samples will be 1/3 of the Γ_{Si} in 1600^0C samples where elongated morphology was observed. Thus, a critical Γ_{Si} as a possible trigger for elongated morphology can be ruled out by this observation.

Then as it can be observed from green, red and blue curves, in samples that were sintered at 1500^0C and 1600^0C when the calcium at the grain boundaries reached a critical concentration between Γ_{Ca}=4.5-8 calcium atoms/nm^2, abnormal grain growth occurred with elongated morphology (Figure 3.7., 3.8. and 3.12.). If it was assumed that calcium cations substitute for the aluminum cations, this critical concentration corresponded approximately to 0.5 monolayer of calcium coverage at the grain boundaries. An additional assumption made here is that all calcium atoms were confined to one plane in the grain boundary.

The orange curve in Figure 3.18. showed that all samples sintered at 1400^0C for 1 hour had almost same average grain sizes. Although the average calcium excess at the grain boundaries exceeded Γ_{Ca}=11 calcium atoms/nm^2, only few grains grew abnormally without any change on the average grain size. This behavior can be observed easily in Figure 3.16. One of the possible reason for the constancy in the overall average grain size is that the small grains in these highly calcium doped samples had a lower average grain size than the average grain size of low calcium doped samples and the number of these small grains were much higher than the abnormally grown grains. The fact that the overall average grain size remained almost constant and that only few grains grew abnormally although the Γ_{Ca} reached 11 calcium atoms/nm^2 may be indicative that for the abnormal grain growth to occur the condition Γ_{Ca} ~ 4-8 calcium atoms/nm^2 is not enough. This condition can be a necessary but not a sufficient condition for abnormal grain growth. Most likely, an additional necessary condition is the certain concentration of a trace impurity whose excess becomes critical as the grain size reaches certain values. Most likely candidate for this trace impurity is silicon which may have been there in the powders below 5 ppm concentration. Silicon may have contaminated samples during sintering in a furnace with $MoSi_2$ heating elements despite the fact that all possible precautions are taken against this contamination possibility. It should be mentioned here again that all the observed microstructures are from the center of samples that were 10-11mm in diameter and 8mm in height.

The existence of small grains with average grain size smaller than the average grain size of the low calcium doped samples were also observed in abnormally grown samples sintered at 1500^0C and 1600^0C. The mechanisms that were responsible for the abnormal grain growth of these samples are still elusive.

When the calcium doping level was increased above Γ_{Ca} ~ 20 calcium atoms/nm^2 for 1500^0C sintered samples and above Γ_{Ca} ~ 30 calcium atoms/nm^2 for 1600^0C sintered samples, the average grain size started to decrease again (Figures 3.9., 3.13.). This drop on the average grain size after a certain calcium excess at the grain boundaries could be indicative of the formation of some second phase precipitates and/or some calcium rich film and phases at the grain boundaries and triple point pockets, respectively. However, with SEM/EDS point analysis and EDS calcium mapping no second phase precipitates or calcium rich phases at triple point pockets were observed. In order to clarify the reason of this behavior, it is necessary to perform conventional TEM analysis to observe possible precipitates and multigrain junction phases.

Given the fact that the system is at the Al_2O_3 rich end of the phase diagram (Figure 1.7.), the expected composition of the precipitates or phases was $CaO.6Al_2O_3$ (CA_6). The studies that were done by Brydson and Kaplan et al. [8, 11] on similar alumina systems also suggested indirectly the formation of CA_6 like phases although it was never observed as a second phase precipitate. Brydson et al. claimed that in their α-alumina/ calcium silicate system there was an amorphous grain boundary film with a nominal composition of CA_6 in the samples sintered at 1400^0C. However, the phase diagram indicates that the melting point of CA_6 is 1850^0C. Thus, it may seem unlikely to have an amorphous CA_6 grain boundary film in calcium doped samples sintered below 1850^0C. But it should be considered that Brydson et al. had also anorthite phase ($CaO.Al_2O_3.2SiO_2$) in the system they studied. Anorthite, CA_6 and alumina phase mixture has a liquidus temperature at 1380^0C [8]. In the system that was studied in this thesis, if there were any CA_6 precipitate or phase, it is expected to be crystalline. The highly co-only doped samples here are the best candidates to verify these amorphous, calcium rich grain boundary films.

All the calcium excess values given here were the calculated data as described before. However, in order to interpret the results more effectively the actual calcium excess values at the grain boundaries should be determined. According to the results of the calculations, calcium coverage increased up to Γ_{Ca}=33 calcium atoms/nm^2 at the point where the average grain size reached a maximum on the green curve in Figure 3.18. It is believed that this value was higher than the alumina grain boundaries can accommodate as a segregant. Therefore, it is also important to predict the structure of highly calcium doped grain boundaries. The question is if there were a submonolayer segregant and second phase precipitates/pockets or a multilayer grain boundary film. According to Brydson et al. [8] calcium segregation of Γ_{ca}=6.1 calcium atoms/nm^2 spread over 6-7 cation planes and Kaplan et al. [11] observed that Γ_{ca}=2.5 calcium atoms/nm^2 distributed over 4±1 cation planes. If what is claimed in the previous work in the literature is correct, this Γ_{Ca}=33 calcium atoms/nm^2 should spread over 30-40 cation planes which shall be easily detectable with an analytical TEM.

When the grain size versus Γ_{Ca} plot (Figure3.18.) was examined more closely, it was recognized that there were some interesting variations between the behavior of

1500^0C and 1600^0C sintered samples although the curves belonging to them look similar. One of the clearest differences was that when the calcium excess values were compared at the point where the average grain size reached its maximum. For 1500^0C sintered samples this point corresponded to calcium excess of Γ_{Ca}=18-22 calcium atoms/nm^2, however, this value increased up to 33 calcium atoms/nm^2 for the samples sintered at 1600^0C. Furthermore, as discussed before for these temperatures there was also a difference at the calcium excess level where the 10% decrease in grain size was observed on the average grain size. The 10% decrease in grain size came at a higher Γ_{ca} value at 1600^0C. Based on these two facts it may be possible that the solubility of calcium in the bulk α-alumina may be different at 1500^0C and 1600^0C. However, the solubility experiments for calcium in bulk alumina are best preformed with a single crystal sapphire. Such experiments will establish the solubility of calcium in α-alumina at different temperatures. The other possibility for different Γ_{Ca} values at the maximum of grain size versus Γ_{Ca} curve is that at these two temperatures the equilibrium thickness of the calcium rich grain boundary film could be different.

4. CONCLUSIONS

Microstructural development of a material is one of the key concerns in developing the desired properties. In order to control the grain structure, it is crucial to control the effects of impurities in a material. This thesis investigated the effects of calcium impurities on the microstructure of alumina that is believed to cause abnormal grain growth.

For all sintering conditions, the grains were small and equiaxed for low calcium concentrations. Only when the calcium excess at the grain boundaries exceeded the critical concentration of Γ_{Ca}=3-4 calcium atoms/nm^2, the grains became elongated. Calcium ions at the grain boundaries at these levels, i.e. between 0.2-4 calcium atoms/nm^2 cause solute drag on the grain boundary motion. The elongated morphology is believed to be due to preferential segregation of calcium to basal planes (0001) in alumina grain boundaries.

Abnormal grain growth with elongated morphology was observed in the samples that were sintered at 1500^{0}C and 1600^{0}C above a critical calcium coverage of Γ_{Ca}=4.5 calcium atoms/nm^2. In these samples the calcium concentrations exceeding a value of Γ_{Ca}=20 calcium atoms/nm^2 and Γ_{Ca}=30 calcium atoms/nm^2 for the sintering temperatures 1500^{0}C and 1600^{0}C, respectively, caused a significant decrease in grain size. Precipitation of a second phase or formation of triple point pockets were suspected for this behavior. However, SEM/EDS studies of the microstructure showed no evidence of a second phase precipitate or calcium rich triple point pockets phases.

For the samples that were sintered at 1400^{0}C, despite the existence of elongated grains, there was no abnormal grain growth at the calcium excess concentration of Γ_{Ca}=11 calcium atoms/nm^2. Only few grains grew abnormally without affecting the overall average grain size. Thus, it can be concluded that above a certain grain boundary concentration calcium is responsible for elongated grain morphology in α-alumina. It is suggested that for the occurrence of abnormal grain growth, presence of calcium as the only impurity in alumina is not a sufficient condition. It appears that the influence of an additional impurity that reaches a critical concentration at grain boundaries for grain growth is necessary. This impurity is suspected to be silicon that could have been introduced in small amounts during sintering.

REFERENCES

1. W. E. Lee, K.P.D. Lagerlof "Structural and Electron Diffraction Data for Sapphire (α-Al_2O_3)," J. of Electron Microscopy Technique, 2:247-258 (1985)
2. M. Barsoum, "Fundamentals of Ceramics," The McGraw-Hill Companies, Inc.,USA, 1997
3. Y.-M. Chiang, D. Birnie III, W. D. Kingery, "Physical Ceramics," John Wiley & Sons, Inc., 1997
4. G. E. Dieter, "Mechanical Metallurgy, " The McGraw-Hill Companies, Inc., USA 1988
5. W. D. Kingery, H. K. Bowen, D. R. Uhlmann, "Introduction to Ceramics," John Wiley & Sons, Inc., 1976
6. A. E. McHale, R. S. Roth, "Phase Equilibria Diagrams, Volume XII, Oxides," The American Ceramic Society, 1996
7. S.C. Hansen, D.S.Phillips, "Grain Boundary Microstructure in a Liquid-Phase Sintered Alumina (α-Al_2O_3)," Philosophical Magazine A, Vol.47, No.2, 209-234 (1983)
8. R. Brydson, S. C. Chen, F. L. Riley, S. J. Milne, "Microstructure and Chemistry of Intergranular Glassy Films in Liquid-Phase-Sintered Alumina," J. Am. Ceram. Soc., 81 [2] 369-79 (1998)
9. Sunggi Baik, Calvin. L. White "Anisotropic Calcium Segregation to the Surface of Al_2O_3," J. Am. Ceram. Soc.,70 [9] 682-88 (1987)
10. S. M. Mukhopadhyay, A.P. Jardine, J. M. Blakely, S. Baik, "Segregation of Magnesium and Calcium to the ($10\bar{1}0$) Prismatic Surface of Magnesium-Implanted Sapphire," J. Am. Ceram. Soc.,71 [5] 358-62 (1988)
11. Wayne D. Kaplan, Harald Müllejans, Manfred Rühle, "Ca Segregation to Basal Surfaces in α-Alumina," J. Am. Ceram. Soc.,78 [10] 2841-44 (1995)

12. Robert F. Cook and A. G. Schrott, "Calcium Segregation to Grain Boundaries in Alumina," J. Am. Ceram. Soc.,71 [1] 50-58 (1988)
13. So Ik Bae, Sunggi Baik, "Determination of Critical Concentrations of Silica and/or Calcia for Abnormal Grain Growth in Alumina," J. Am. Ceram. Soc.,76 [4] 1065-67 (1993)
14. I. J. Bae, S. Baik, "Abnormal Grain Growth in Alumina," Materials Science Forum Vols. 204-206 pp. 485-490 (1996)
15. C. W. Park, D. Y. Yoon, "Effects of SiO_2, CaO and MgO Additions on the Grain Growth of Alumina," J. Am. Ceram. Soc., 83 [10] 2605-609 (2000)
16. Y.-M. Kim, S. H. Hong, D.-Y. Kim, "Anisotropic Abnormal Grain Growth in TiO_2/SiO_2-Doped Alumina," J. Am. Ceram. Soc., 83 [11] 2809-12 (2000)
17. A. Kebbede, A. H. Carim, "Segregation of Si and Ti in α-alumina," Materials Letters, 41, 198-203 (1999)
18. S. J. Bennison, M. P. Harmer, "A History of the Role of MgO in the Sintering of α-Al_2O_3, " Ceramic Transactions, Vol. 7, pp. 13ff, 1990
19. R. L. Coble, "Sintering of Crystalline Solids-II. Experimental Test of Diffusion Models in Porous Compacts, " J. Appl. Phys., 32[5], 793-99, 1961
20. A. H. Heuer, "The Role of Magnesia in the Sintering of Alumina," J. Am. Ceram. Soc., 62 [5-6], 317-18 (1979)
21. A. H. Heuer, "Reply, " J. Am. Ceram. Soc., 63 [3-4], 230-31 (1980)
22. W. C. Johnson, R. L. Coble, "A Test of the Second Phase and Impurity Segregation Models for MgO Enhanced Densificaiton of Sintered Alumina," J. Am. Ceram. Soc., 61[3-4], 110 (1978)
23. S. J. Bennison and M. P. Harmer, "Grain Growth Kinetics for Alumina in the Absence of a Liquid Phase," J. Am. Ceram. Soc, 68[1], C22-24 (1985)
24. K. A. Berry and M. P. Harmer, "Effect of MgO Solute on Microstructure Development in Al_2O_3," J. Am. Ceram. Soc, 69[2], 143-49 (1986)
25. C. A. Handwerker, J. M. Dynys, R. M. Cannon, R. L. Coble, "Dihedral Angles in MgO and Al_2O_3," J. Am. Ceram. Soc., 73, 1371 (1990)
26. K. L. Gavrilov, S. J. Bennison, K. R. Mikeska, J. M. Chabala, R. Levi-Setti, "Silica and Magnesia Dopant Distributions in Alumina by High-Resolution Scanning Secondary Ion Mass Spectrometry," J. Am. Ceram. Soc. 82[4] 1001-1008 (1999)

27. C. A. Handwerker, P. A. Morris, R. L. Coble, "Effects of Chemical Inhomogeneities on Grain Growth and Microstructure in Al_2O_3," J. Am. Ceram. Soc., 72[1] 130-36 (1989)
28. I. Sakaguchi, H. Haneda, V. Srikanth, T. Ikegami, "An Effect of Second Phase on Oxygen Grain Boundary Diffusion in MgO-Doped Polycrystalline Alumina," Materials Research Bulletin, Vol. 31, No. 7, pp 837-843, 1996
29. C. A. Bateman, S. J. Bennison, M. P. Harmer, "Mechanisms for the Role of Magnesia in the Sintering of Alumina Containing Small Amounts of a Liquid Phase," J. Am. Ceram. Soc., 72[7] 1241-44 (1989)
30. J. Zhao, M. P. Harmer, "Sintering of Ultra-High-Purity Alumina Doped Simultaneously with MgO and FeO," J. Am. Ceram. Soc., 70[12] 860-66 (1987)
31. M. A. Gülgün, R. Voytovych, I. Maclaren, M. Rühle, "Cation Segregation in an Oxide Ceramic with Low Solubility: Yttrium doped α-alumina," Interface Science, 40, pp 99-110 (2002)
32. C. M. Wang, G. S. Cargill III, H. M. Chan, M. P. Harmer, "Structural Features of Y-Saturated and Supersaturated Grain Boundaries in Alumina," Acta Materialia, Vol.48, pp. 2579-2591, 2000
33. J. Cho, C. M. Wang, H. M. Chan, J. M. Rickman, M. P. Harmer, "Role of Segregating Dopants on the Improved Creep Resistance of Aluminum Oxide," Acta Materialia, Vol. 47, Nos 15, pp 4197-4207, 1999
34. J. Bruley, J. Cho, H. M. Chan, M. P. Harmer, J. M. Rickman, "Scanning Transmission Electron Microscopy Analysis of Grain Boundaries in Creep-Resistant Yttrium- and Lanthanum- Doped Alumina Microstructures," J. Am. Ceram. Soc. 82[10] 2865-70 (1999)
35. M. A. Gülgün, V. Putlayev, M. Rühle, "Effects of Yttrium Doping α-Alumina:I, Microstructure and Microchemistry, " J. Am. Ceram. Soc. 82[7] 1849-56 (1999)
36. R. Voytovych, I. MacLaren, M. A. Gülgün, R. M. Cannon, M. Rühle, "The effect of Yttrium on Densification and Grain Growth in α-Alumina, " in press
37. H. Yoshida, Y. Ikuhara, T.Sakuma, "High Temperature Creep Resistance in Rare-Earth Doped, Fine Grained Al_2O_3," Journal of. Material Research, 13, 2597 (1998)
38. H. Yoshida, Y. Ikuhara, T.Sakuma, "Transient Creep in Fine Grained Polycrystalline Al_2O_3 with Lu^{3+} Ion Segregation at the Grain Boundaries," Journal of. Material Research., 16, 716 (2001)

APPENDIX A

A.1. Grain Size Measurement

A.1a. Average Grain Size Measurement by Mean Linear Intercept Method

Total number of grains intersected the lines that were drawn randomly on the given micrograph are 200 (Figure A.1a.1.). Each line is 26.8 cm and totally there are 7 lines. Therefore;

26.8 × 7 = 187.6 cm total length of the lines
187.6 / 200 = 0.938 cm/cut

From the SEM micrograph:

5 microns = 4.2 cm

Then;

$\overline{L} = 0.938 \times (5 / 4.2) = 1.12$ microns

Grain size = $\overline{L} \times 1.5 = 1.68$ microns

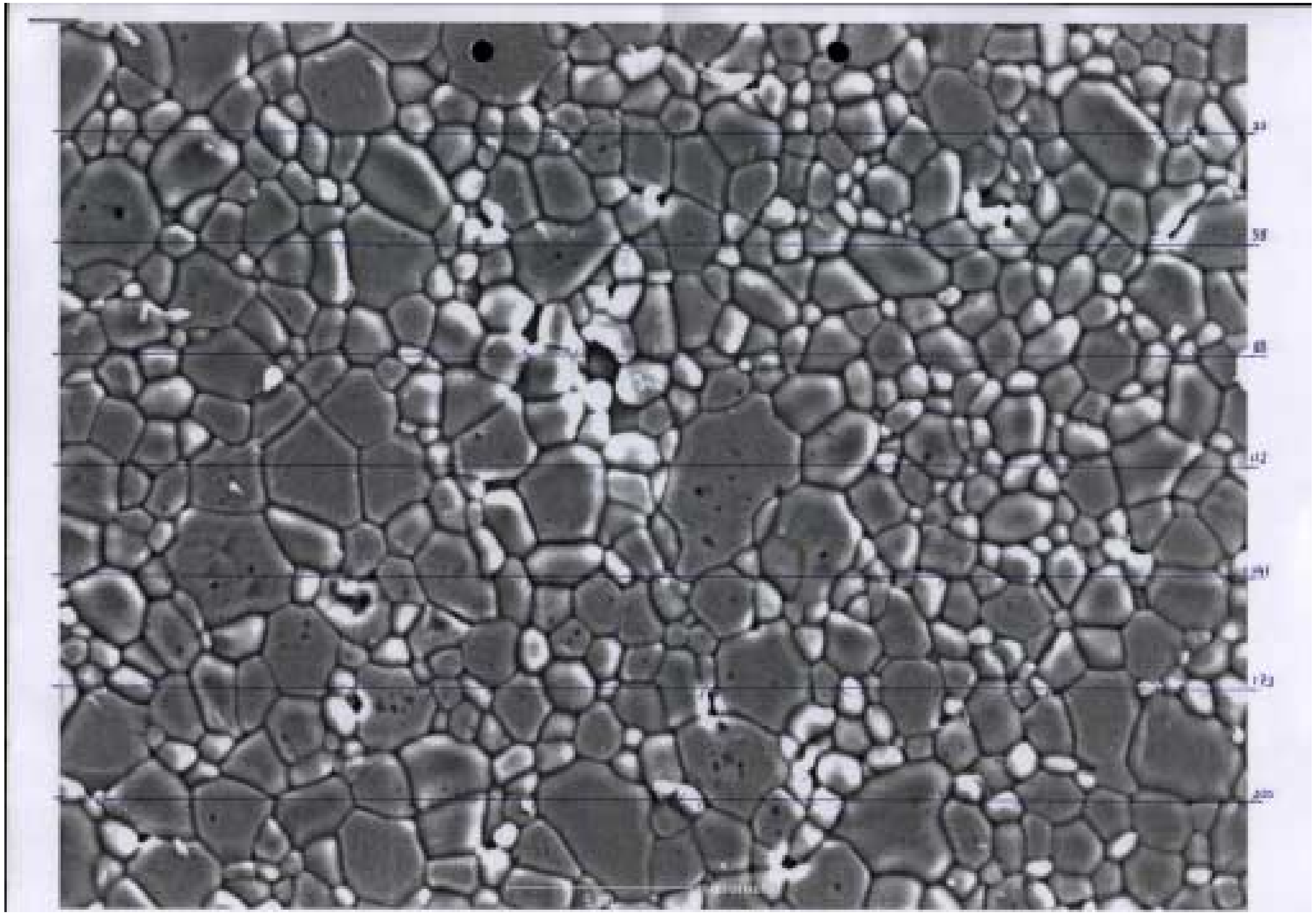

Figure A.1a.1. Measurement of the average grain size of 60 ppm Ca doped sample sintered at 1500^{0}C for 12 hours

A.1b. Average Grain Size Measurement of Small and Large Grains

The average grain size of small grains was calculated by mean linear intercept method as described in Appendix A.1a. From the Figure A.1b.1. total number of small grains intersected the lines that were drawn randomly on the given micrograph are 364. Total length of the lines is 303.7 cm. Therefore;

303.7 / 364 = 0.834 cm / cut

From the SEM micrograph:

5 microns = 4.2 cm

Then;

$\overline{L}_{\text{small grains}} = 0.834 \times (5 / 4.2) = 0.99$ microns

Average grain size$_{\text{small grains}} = \overline{L} \times 1.5 = 1.49$ microns

The grain sizes of large grains were measured one by one and the arithmetic average was taken. Always the largest dimension of the anisotropic grains was taken as the grain size of large grains. As can be seen in Figure A.1b.1., there are 16 large grains and the total grain size of these grains is 93.9 cm. Therefore;

93.9 / 16 =5.87 cm / large grain

From the SEM micrograph:

5 microns = 4.2 cm

Average grain size$_{\text{large grains}} = 5.87 \times (5 / 4.2) = 6.99$ microns

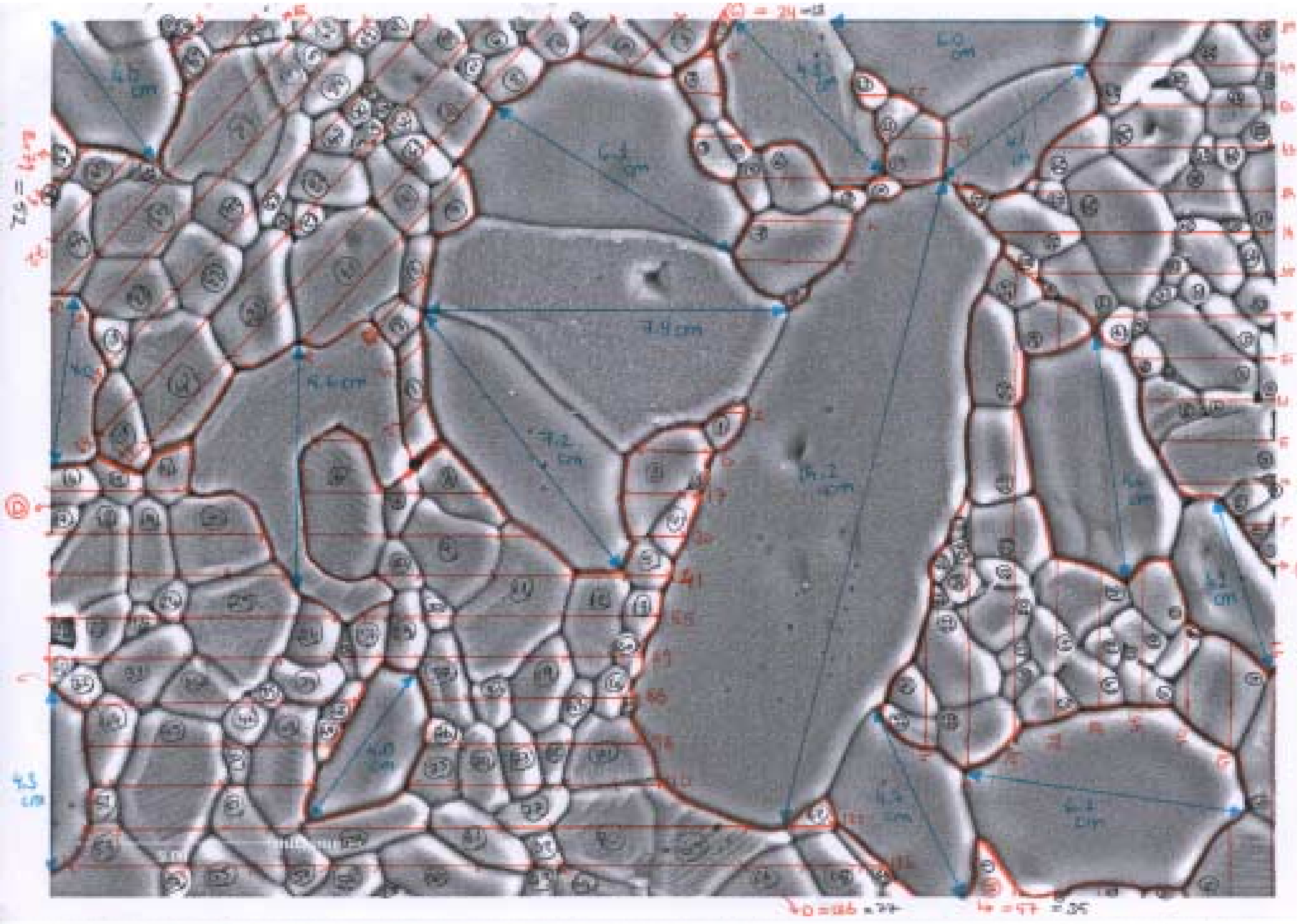

Figure A.1b.1. Measurement of the average grain sizes of small and large grains in 133 ppm Ca doped sample sintered at 1500^0C for 12 hours

A.2. Density Measurement

The size, shape, distribution, and amount of the total porosity can be determined from the microstructure. The total porosity can also be measured by determining the apparent density $\rho_{apparent}$ of a sample (total weight/total volume, including pores) and comparing this with the true density ρ_{true} (total weight/volume of solids).

The true density can be determined readily for a single-phase material but not so easily for a polyphase material. For a crystalline solid the density can be calculated from the crystal structure and lattice constant, since the atomic weight for each constituent is known. True density can also be determined by comparing pore free samples with a liquid of a known density. For glasses and single crystals this can be done by weighing the material in air and then suspended in a liquid, determining the volume by Archimedes' method; it can be done more precisely by adjusting the composition or temperature of a liquid column just to balance the density of the solid so that it neither sinks nor rises but remains suspended in the liquid. For complex mixtures and porous solids the sample must be pulverized until there are no residual closed pores and the density is then determined by the pycnometer method. The sample is put in a known-volume pycnometer bottle and weighed; then the liquid is added to give a known volume of liquid plus solid and another weight is taken. To ensure penetration of the solid among all particles, the sample and liquid should be boiled or heated under vacuum. The differences in weights obtained give the liquid volume to give the solid sample volume from which the density can be calculated.

The apparent density of porous bodies requires determination of the total volume of solid plus pores. For samples such as bricks this can be done by measuring the sample dimensions and calculating the volume. For smaller samples apparent density can be determined by measuring the weight of mercury (or of any other non-wetting liquid that does not penetrate the pores) displaced by the sample with a mercury volumeter, or the force required to submerge the sample (Archimedes' method). For small samples apparent density can also be determined by coating the sample with an impermeable film such as paraffin. The weight of the film is measured by difference so that the film volume is known. Then the volume of the sample plus film can be determined by Archimedes' method and the sample volume measured by difference. The total porosity can be determined at the same time the open-pore volume is measured by first weighing a sample in air W_a and then heating in boiling water for 2 hr to fill the open pores completely with water. After cooling, the weight of the saturated piece is determined (1) suspended in water W_{sus} and (2) in air W_{sat}. The difference between these last two values gives the sample volume and allows calculation of the apparent density. The difference between saturated and dry weights gives the open-pore volume [5].

The densities of the samples were measured by Archimedes' method. Distilled water at 21^0C was used as the wetting liquid. The weights of the compacts were measured first in air then in distilled water and the densities were calculated according to the following formula:

$$\rho_{apparent} = \frac{mass_{air} \times \rho_{\ water}}{mass_{air} - mass_{water}} \qquad (A.2.1)$$

then the %theoretical densities (%TD) were found

$$\%TD = \frac{\rho_{true} - \rho_{apparent}}{\rho_{true}} * 100 \qquad (A.2.2)$$

APPENDIX B

B.1. Micrographs of the different calcium doped α-Al_2O_3 samples sintered at 1400^0C for 1 hour

a)

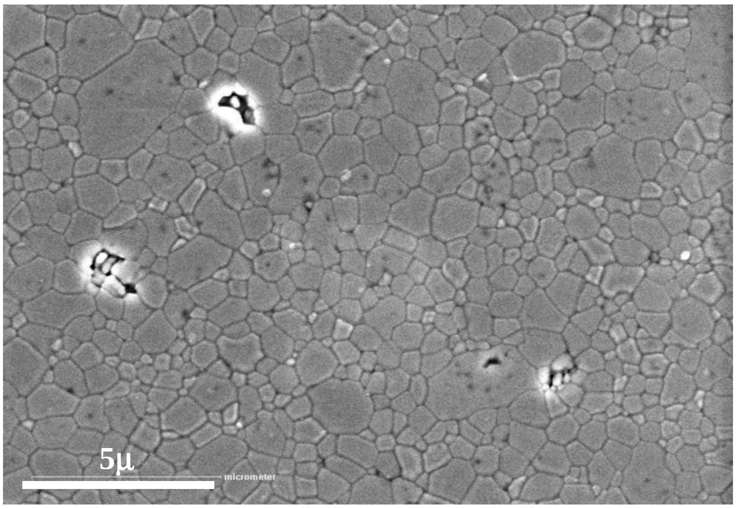

b)

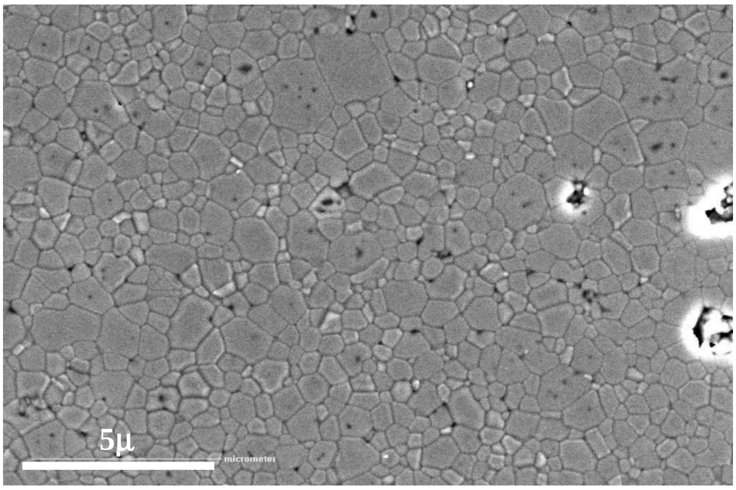

Figure B.1.1. a) Undoped α-Al_2O_3 b) 7.1 ppm Ca doped α-Al_2O_3

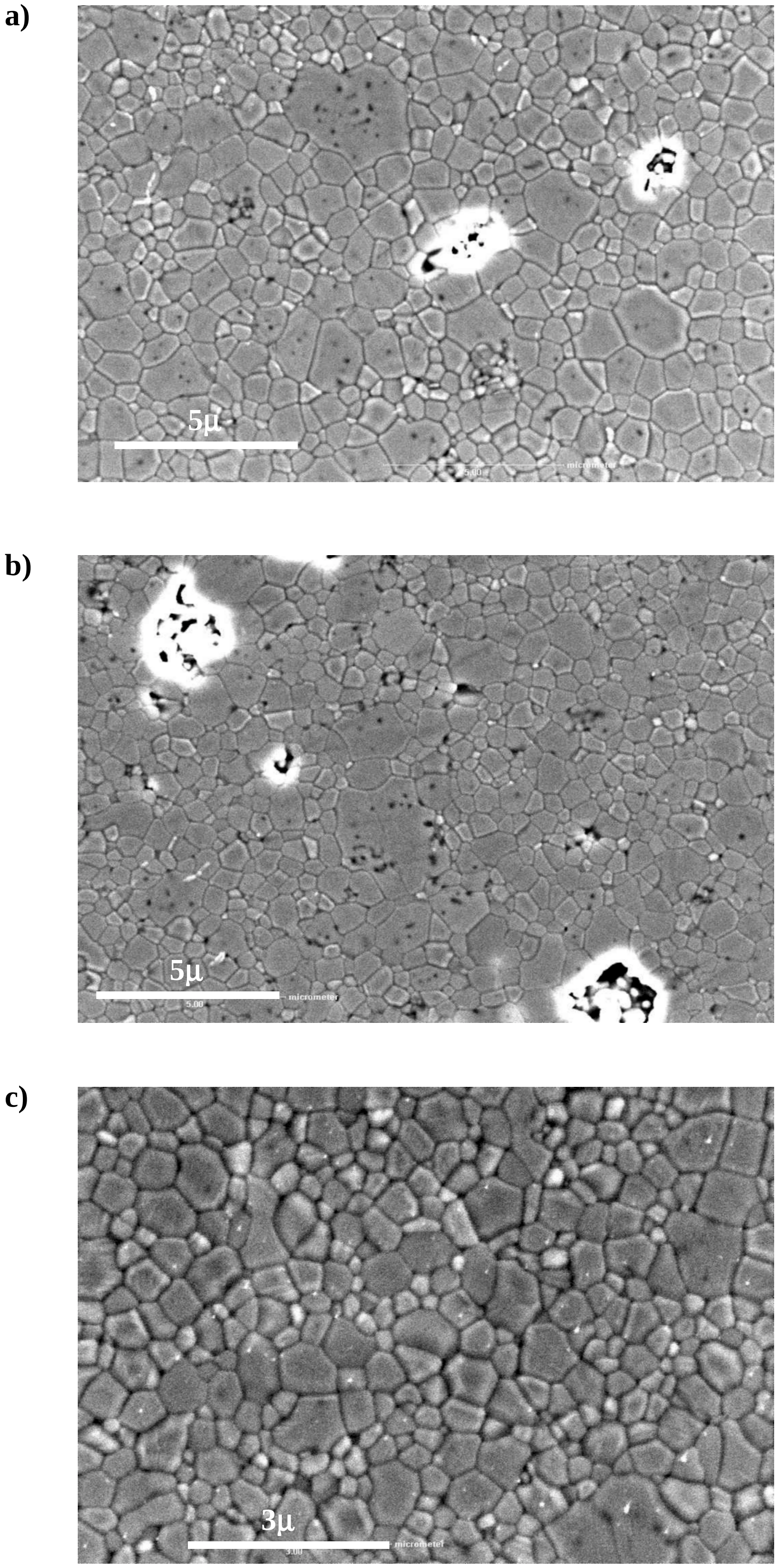

Figure B.1.2. a) 10.8 ppm Ca doped α-Al_2O_3 b) 23 ppm Ca doped α-Al_2O_3 c) 60 ppm Ca doped α-Al_2O_3

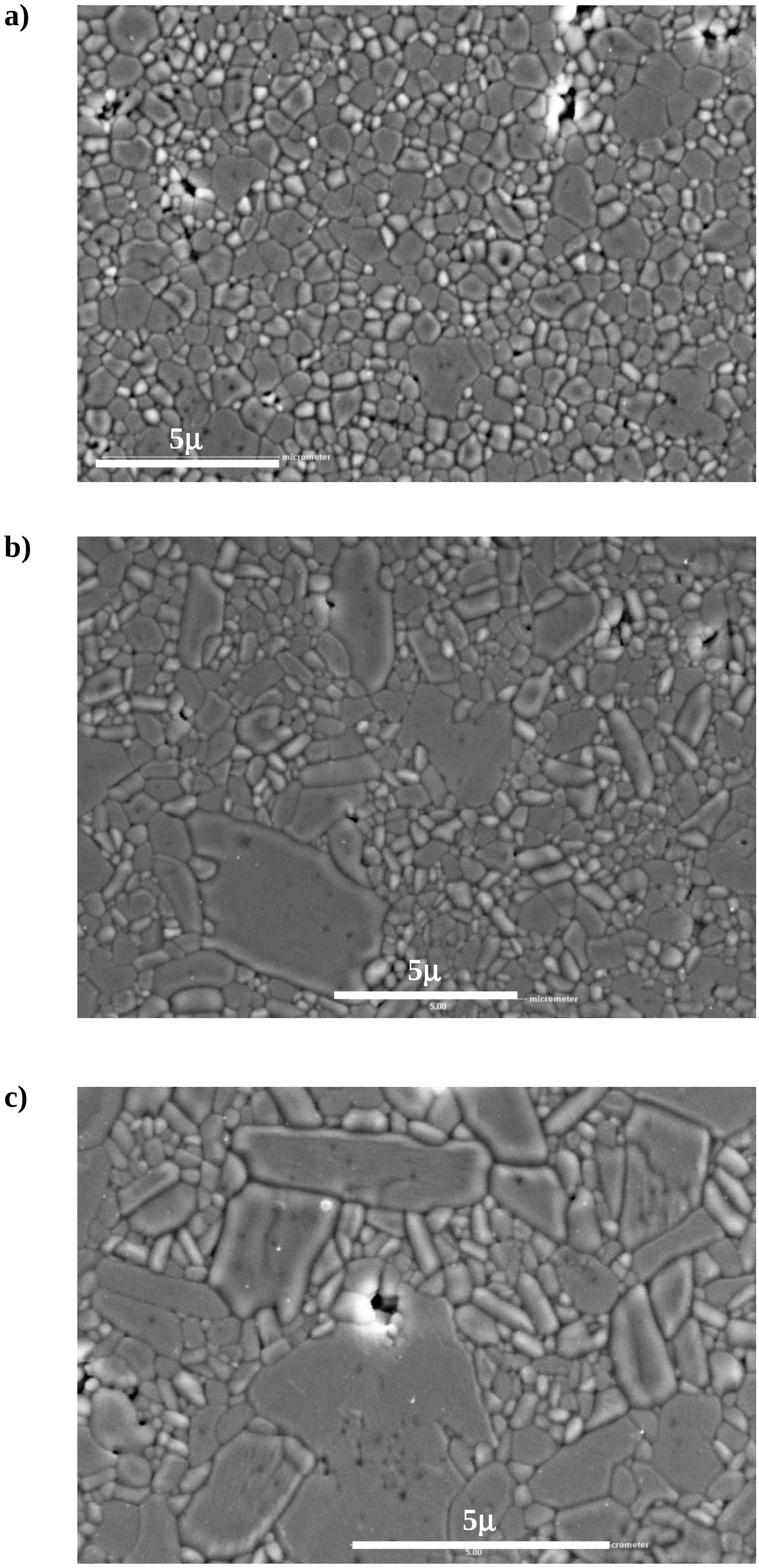

Figure B.1.3. a) 133 ppm Ca doped α-Al_2O_3 b) 344 ppm Ca doped α-Al_2O_3 c) 650 ppm Ca doped α-Al_2O_3

B.2. Micrographs of the different calcium doped α-Al_2O_3 samples sintered at 1500^0C for 1 hour

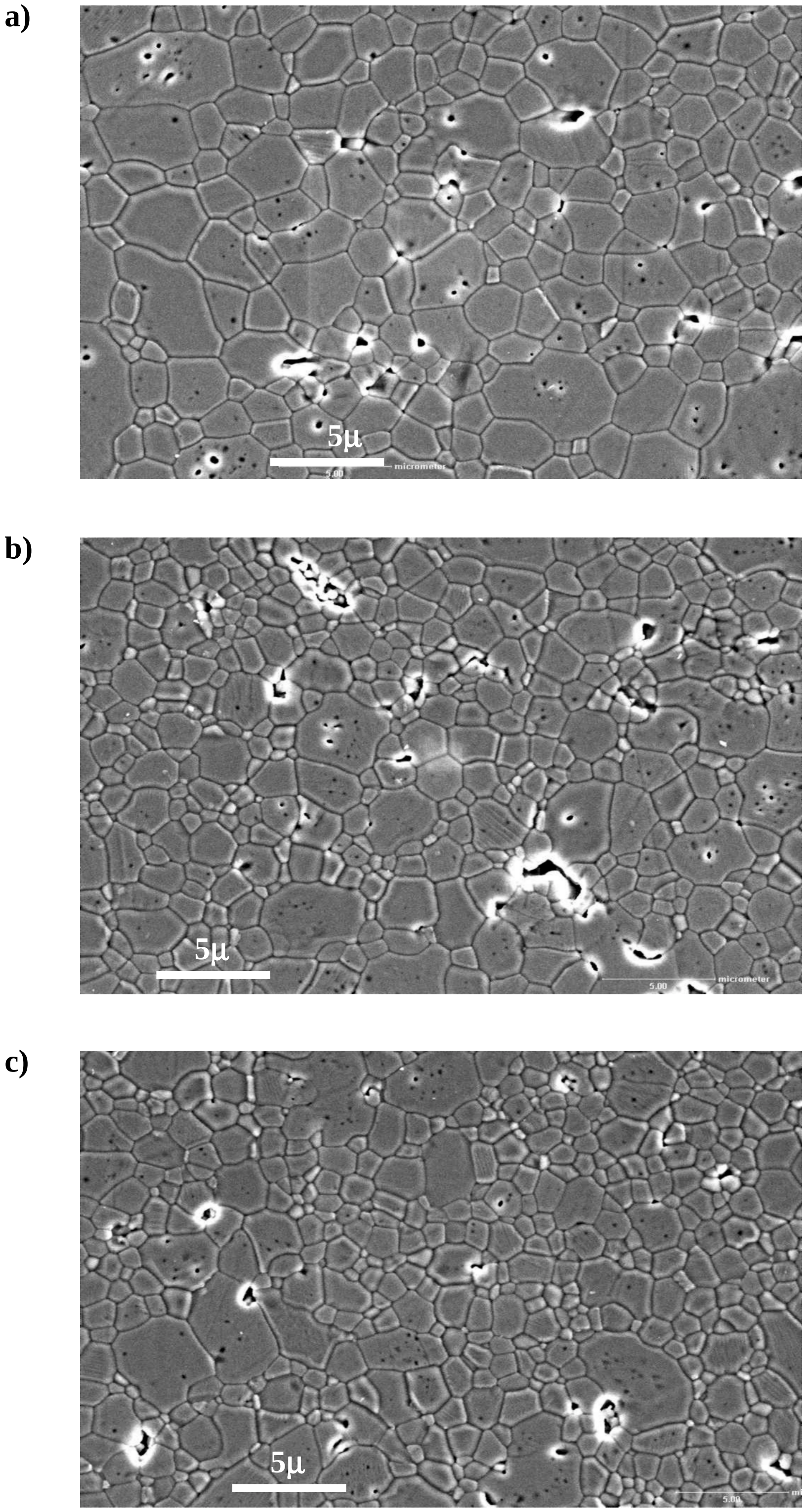

Figure B.2.1. a) Undoped α-Al_2O_3 b) 7.1 ppm Ca doped α-Al_2O_3
c) 10.8 ppm Ca doped α-Al_2O_3

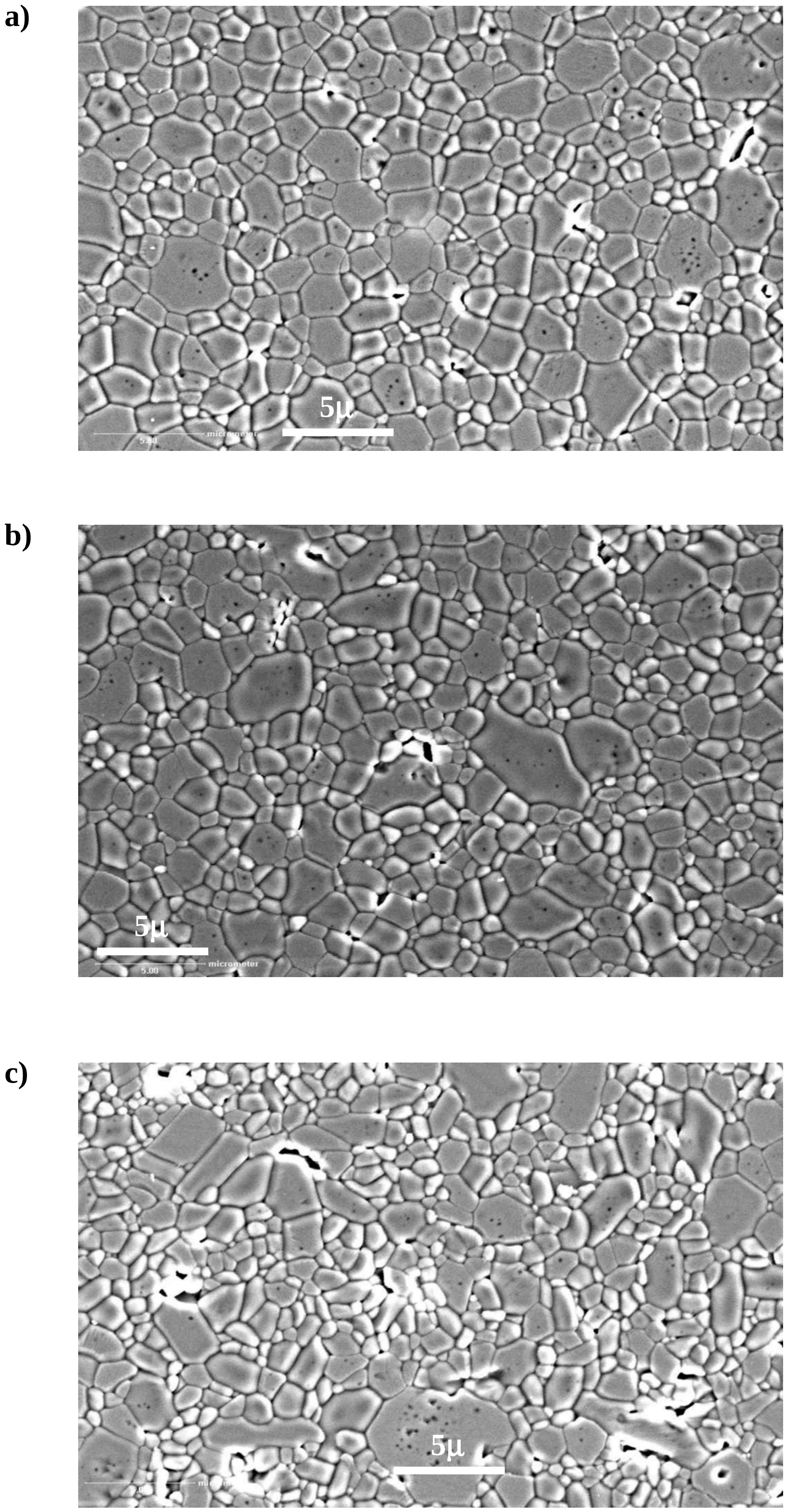

Figure B.2.2. a) 23 ppm Ca doped α-Al_2O_3 b) 60 ppm Ca doped α-Al_2O_3 c) 133 ppm Ca doped α-Al_2O_3

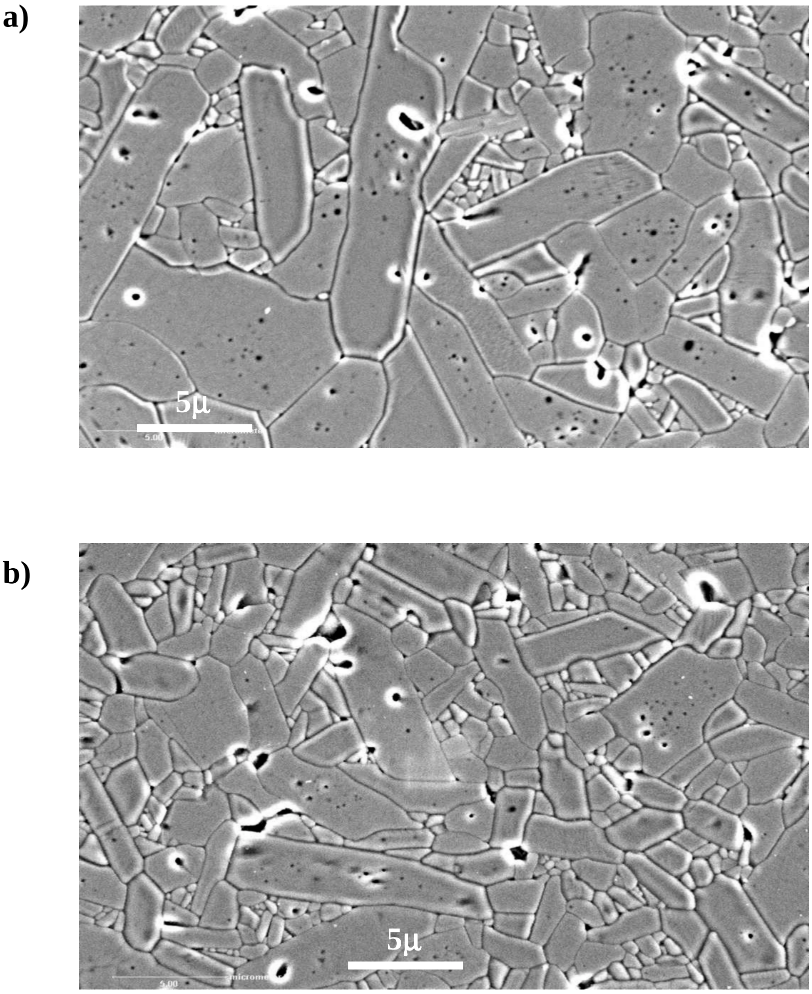

Figure B.2.3. a) 344 ppm Ca doped α-Al_2O_3 b) 650 ppm Ca doped α-Al_2O_3

B.3. Micrographs of the different calcium doped α-Al_2O_3 samples sintered at 1500^0C for 12 hours

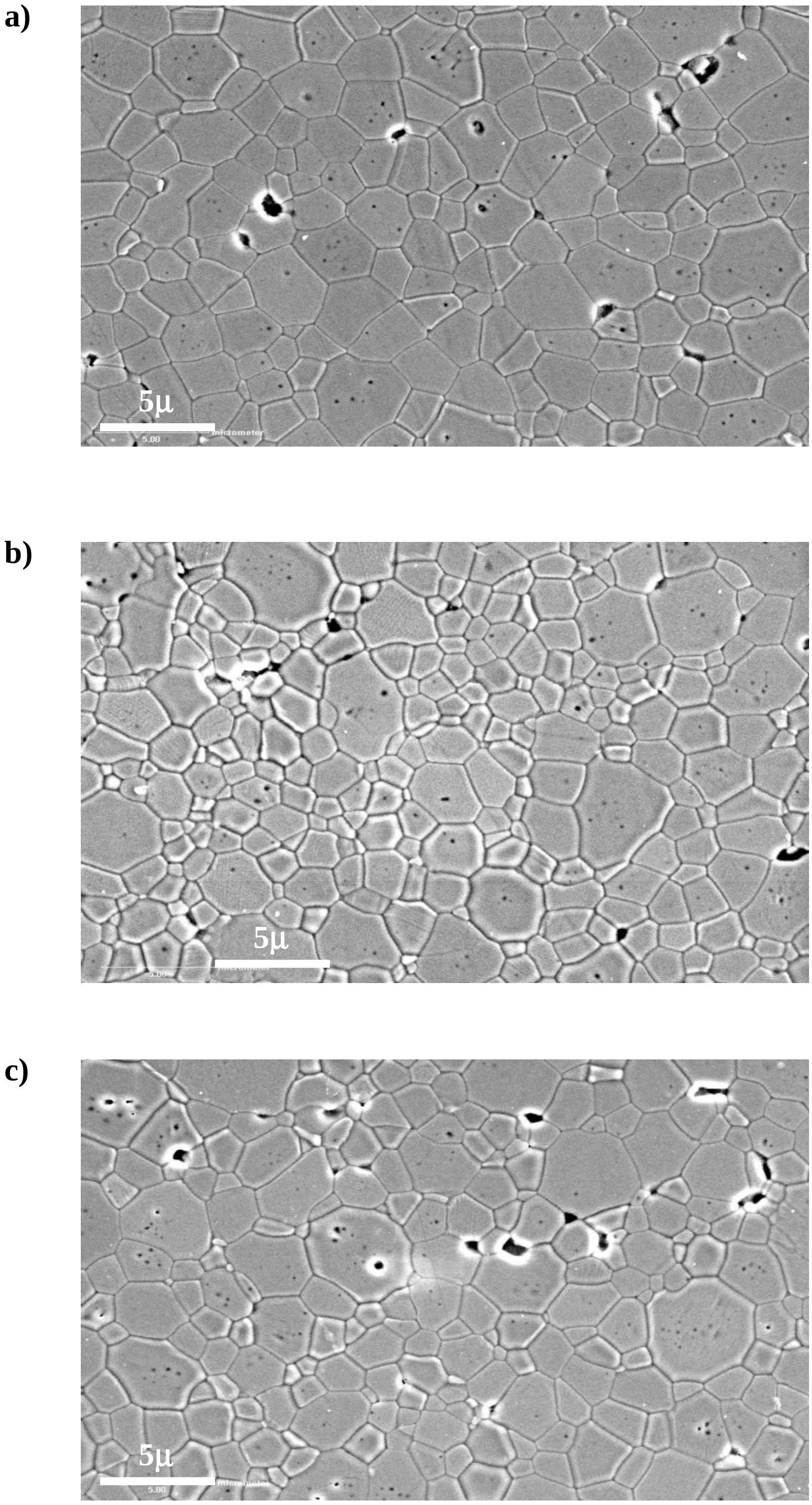

Figure B.3.1. a) Undoped α-Al_2O_3 b) 7.1 ppm Ca doped α-Al_2O_3 c) 10.8 ppm Ca doped α-Al_2O_3

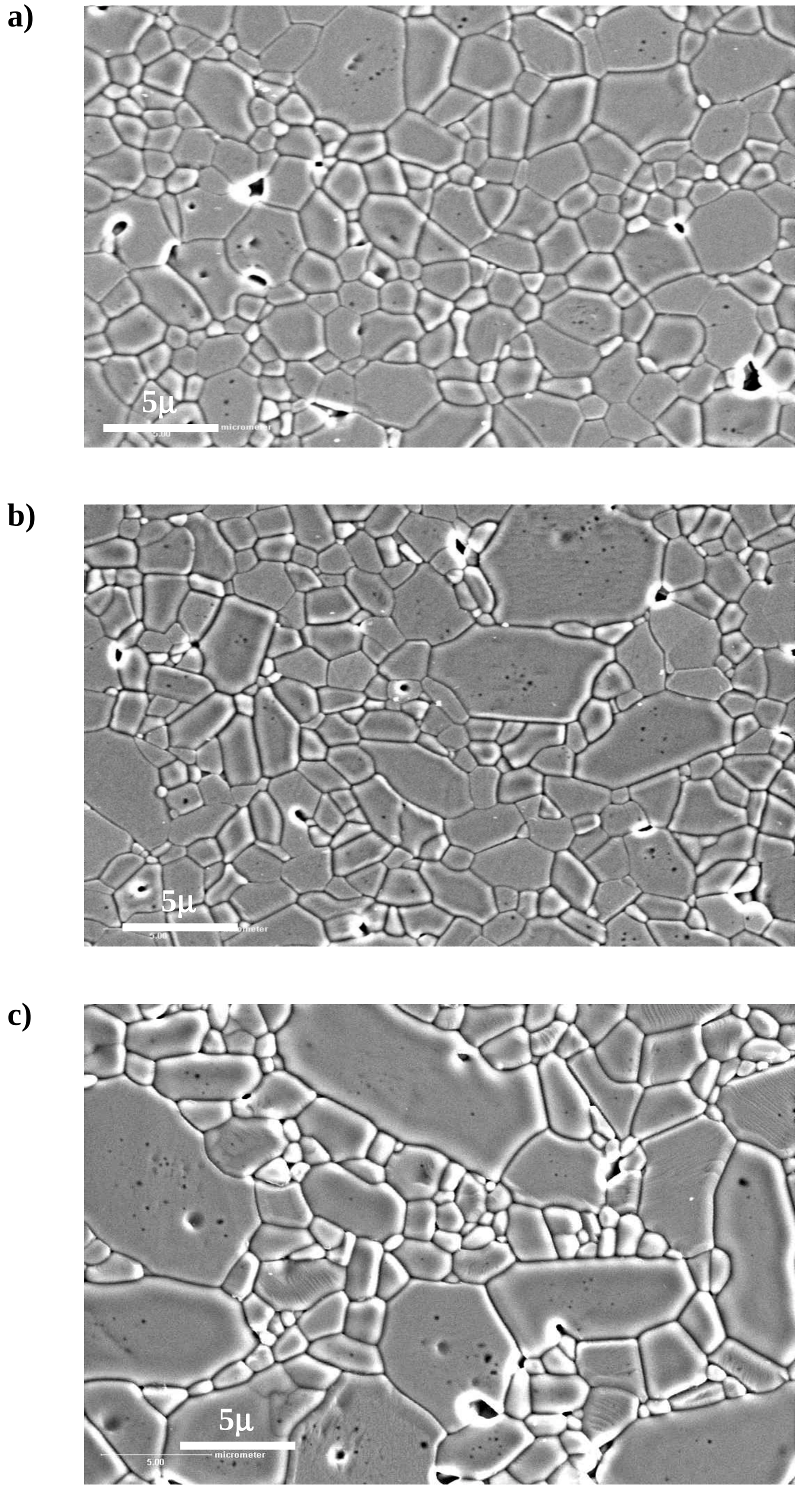

Figure B.3.2. a) 23 ppm Ca doped α-Al_2O_3 b) 60 ppm Ca doped α-Al_2O_3 c) 133 ppm Ca doped α-Al_2O_3

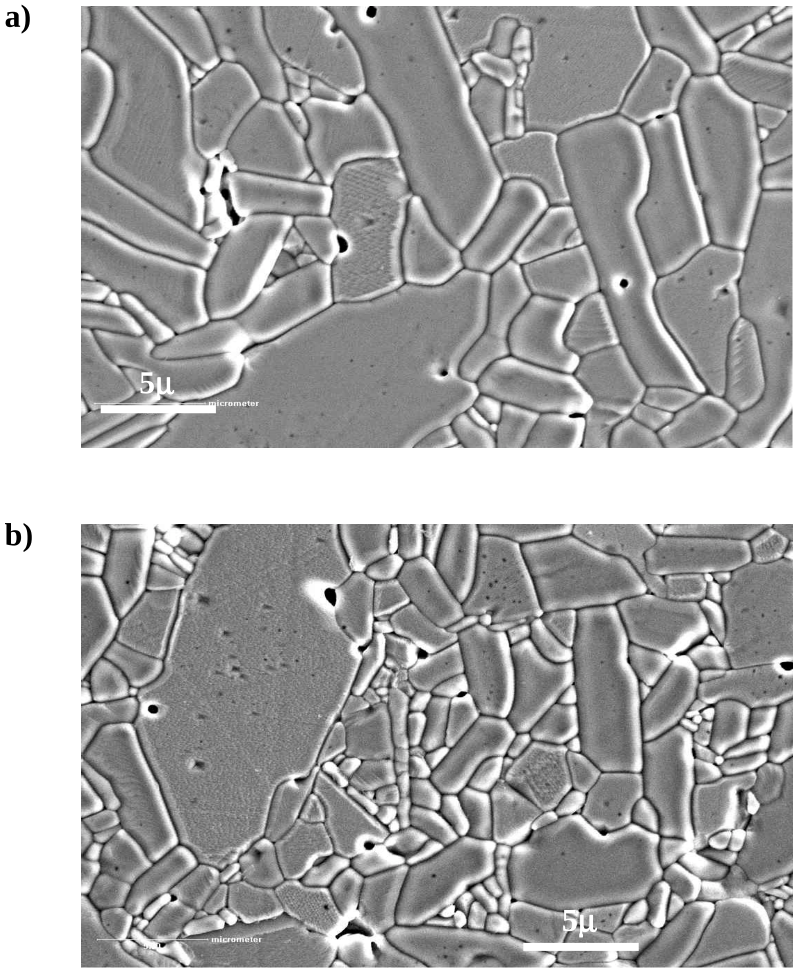

Figure B.3.3. a) 344 ppm Ca doped α-Al_2O_3 b) 650 ppm Ca doped α-Al_2O_3

B.4. Micrographs of the different calcium doped α-Al_2O_3 samples sintered at 1600^0C for 1 hour

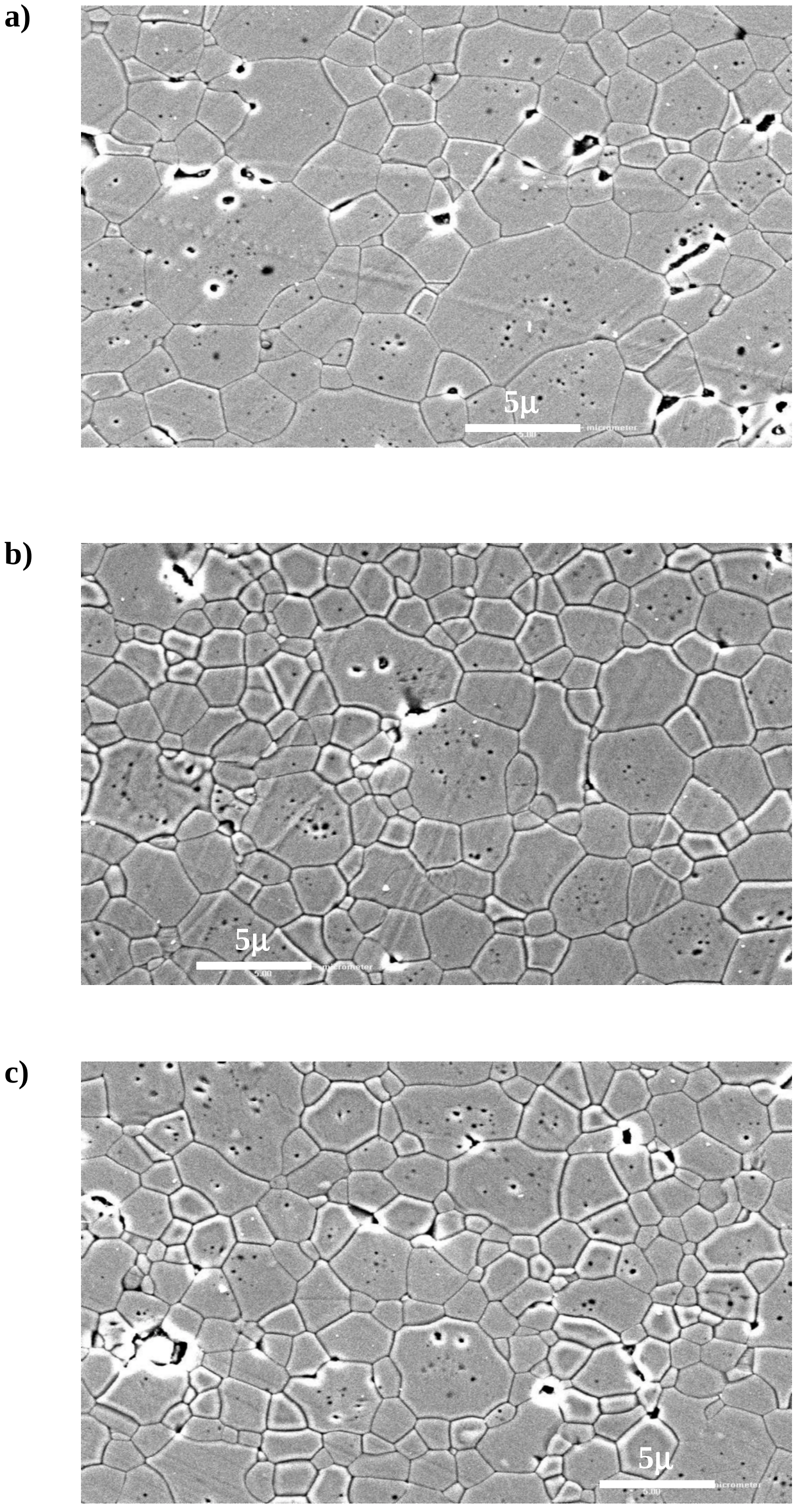

Figure B.4.1. a) Undoped α-Al_2O_3 b) 7.1 ppm Ca doped α-Al_2O_3
c) 10.8 ppm Ca doped α-Al_2O_3

a)

b)

c)

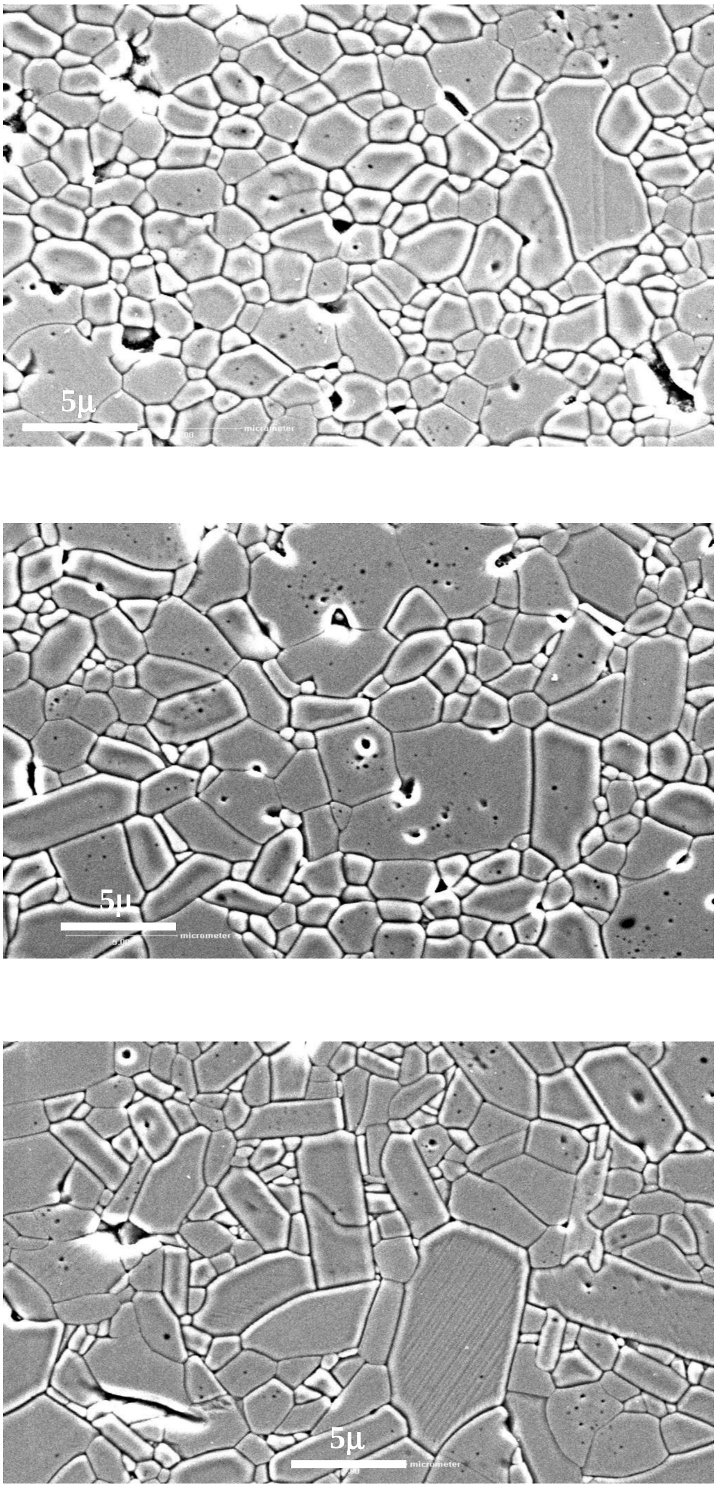

Figure B.4.2. a) 23 ppm Ca doped α-Al_2O_3 b) 60 ppm Ca doped α-Al_2O_3 c) 133 ppm Ca doped α-Al_2O_3

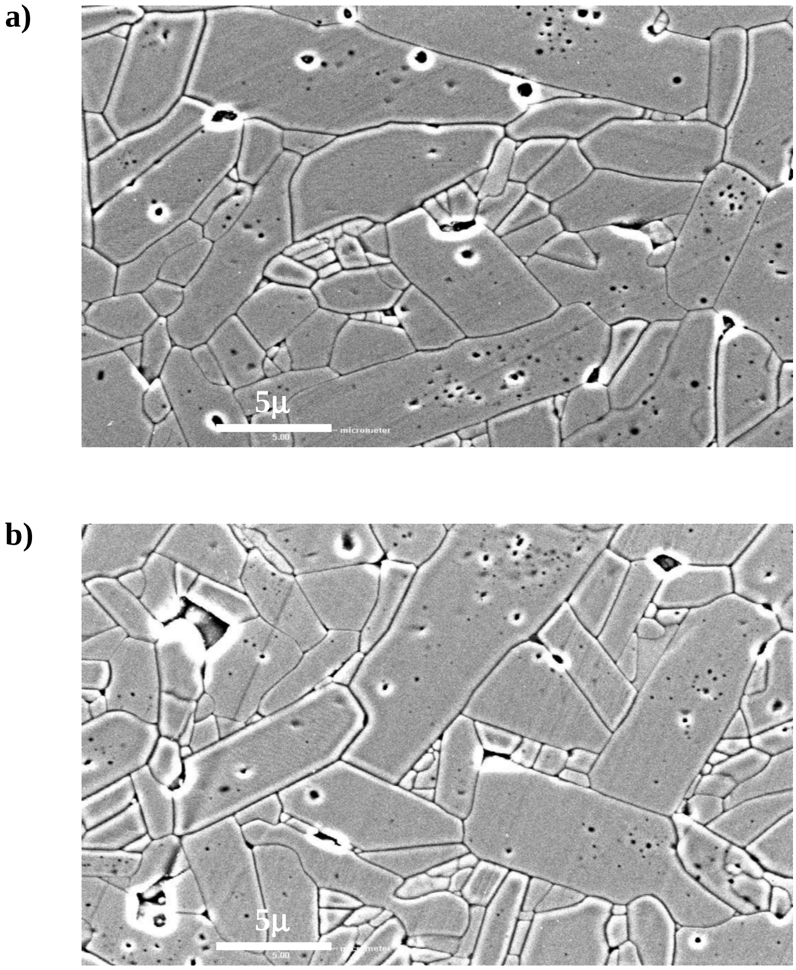

Figure B.4.3. a) 344 ppm Ca doped α-Al_2O_3 b) 650 ppm Ca doped α-Al_2O_3

REFERENCES

1. W. E. Lee, K.P.D. Lagerlof "Structural and Electron Diffraction Data for Sapphire (α-Al_2O_3)," J. of Electron Microscopy Technique, 2:247-258 (1985)
2. M. Barsoum, "Fundamentals of Ceramics," The McGraw-Hill Companies, Inc.,USA, 1997
3. Y.-M. Chiang, D. Birnie III, W. D. Kingery, "Physical Ceramics," John Wiley & Sons, Inc., 1997
4. G. E. Dieter, "Mechanical Metallurgy, " The McGraw-Hill Companies, Inc., USA 1988
5. W. D. Kingery, H. K. Bowen, D. R. Uhlmann, "Introduction to Ceramics," John Wiley & Sons, Inc., 1976
6. A. E. McHale, R. S. Roth, "Phase Equilibria Diagrams, Volume XII, Oxides," The American Ceramic Society, 1996
7. S.C. Hansen, D.S.Phillips, "Grain Boundary Microstructure in a Liquid-Phase Sintered Alumina (α-Al_2O_3)," Philosophical Magazine A, Vol.47, No.2, 209-234 (1983)
8. R. Brydson, S. C. Chen, F. L. Riley, S. J. Milne, "Microstructure and Chemistry of Intergranular Glassy Films in Liquid-Phase-Sintered Alumina," J. Am. Ceram. Soc., 81 [2] 369-79 (1998)
9. Sunggi Baik, Calvin. L. White "Anisotropic Calcium Segregation to the Surface of Al_2O_3," J. Am. Ceram. Soc.,70 [9] 682-88 (1987)
10. S. M. Mukhopadhyay, A.P. Jardine, J. M. Blakely, S. Baik, "Segregation of Magnesium and Calcium to the $(10\bar{1}0)$ Prismatic Surface of Magnesium-Implanted Sapphire," J. Am. Ceram. Soc.,71 [5] 358-62 (1988)
11. Wayne D. Kaplan, Harald Müllejans, Manfred Rühle, "Ca Segregation to Basal Surfaces in α-Alumina," J. Am. Ceram. Soc.,78 [10] 2841-44 (1995)

12. Robert F. Cook and A. G. Schrott, "Calcium Segregation to Grain Boundaries in Alumina," J. Am. Ceram. Soc.,71 [1] 50-58 (1988)
13. So Ik Bae, Sunggi Baik, "Determination of Critical Concentrations of Silica and/or Calcia for Abnormal Grain Growth in Alumina," J. Am. Ceram. Soc.,76 [4] 1065-67 (1993)
14. I. J. Bae, S. Baik, "Abnormal Grain Growth in Alumina," Materials Science Forum Vols. 204-206 pp. 485-490 (1996)
15. C. W. Park, D. Y. Yoon, "Effects of SiO_2, CaO and MgO Additions on the Grain Growth of Alumina," J. Am. Ceram. Soc., 83 [10] 2605-609 (2000)
16. Y.-M. Kim, S. H. Hong, D.-Y. Kim, "Anisotropic Abnormal Grain Growth in TiO_2/SiO_2-Doped Alumina," J. Am. Ceram. Soc., 83 [11] 2809-12 (2000)
17. A. Kebbede, A. H. Carim, "Segregation of Si and Ti in α-alumina," Materials Letters, 41, 198-203 (1999)
18. S. J. Bennison, M. P. Harmer, "A History of the Role of MgO in the Sintering of α-Al_2O_3, " Ceramic Transactions, Vol. 7, pp. 13ff, 1990
19. R. L. Coble, "Sintering of Crystalline Solids-II. Experimental Test of Diffusion Models in Porous Compacts, " J. Appl. Phys., 32[5], 793-99, 1961
20. A. H. Heuer, "The Role of Magnesia in the Sintering of Alumina," J. Am. Ceram. Soc., 62 [5-6], 317-18 (1979)
21. A. H. Heuer, "Reply, " J. Am. Ceram. Soc., 63 [3-4], 230-31 (1980)
22. W. C. Johnson, R. L. Coble, "A Test of the Second Phase and Impurity Segregation Models for MgO Enhanced Densificaiton of Sintered Alumina," J. Am. Ceram. Soc., 61[3-4], 110 (1978)
23. S. J. Bennison and M. P. Harmer, "Grain Growth Kinetics for Alumina in the Absence of a Liquid Phase," J. Am. Ceram. Soc, 68[1], C22-24 (1985)
24. K. A. Berry and M. P. Harmer, "Effect of MgO Solute on Microstructure Development in Al_2O_3," J. Am. Ceram. Soc, 69[2], 143-49 (1986)
25. C. A. Handwerker, J. M. Dynys, R. M. Cannon, R. L. Coble, "Dihedral Angles in MgO and Al_2O_3," J. Am. Ceram. Soc., 73, 1371 (1990)
26. K. L. Gavrilov, S. J. Bennison, K. R. Mikeska, J. M. Chabala, R. Levi-Setti, "Silica and Magnesia Dopant Distributions in Alumina by High-Resolution Scanning Secondary Ion Mass Spectrometry," J. Am. Ceram. Soc. 82[4] 1001-1008 (1999)

27. C. A. Handwerker, P. A. Morris, R. L. Coble, "Effects of Chemical Inhomogeneities on Grain Growth and Microstructure in Al_2O_3," J. Am. Ceram. Soc., 72[1] 130-36 (1989)
28. I. Sakaguchi, H. Haneda, V. Srikanth, T. Ikegami, "An Effect of Second Phase on Oxygen Grain Boundary Diffusion in MgO-Doped Polycrystalline Alumina," Materials Research Bulletin, Vol. 31, No. 7, pp 837-843, 1996
29. C. A. Bateman, S. J. Bennison, M. P. Harmer, "Mechanisms for the Role of Magnesia in the Sintering of Alumina Containing Small Amounts of a Liquid Phase," J. Am. Ceram. Soc., 72[7] 1241-44 (1989)
30. J. Zhao, M. P. Harmer, "Sintering of Ultra-High-Purity Alumina Doped Simultaneously with MgO and FeO," J. Am. Ceram. Soc., 70[12] 860-66 (1987)
31. M. A. Gülgün, R. Voytovych, I. Maclaren, M. Rühle, "Cation Segregation in an Oxide Ceramic with Low Solubility: Yttrium doped α-alumina," Interface Science, 40, pp 99-110 (2002)
32. C. M. Wang, G. S. Cargill III, H. M. Chan, M. P. Harmer, "Structural Features of Y-Saturated and Supersaturated Grain Boundaries in Alumina," Acta Materialia, Vol.48, pp. 2579-2591, 2000
33. J. Cho, C. M. Wang, H. M. Chan, J. M. Rickman, M. P. Harmer, "Role of Segregating Dopants on the Improved Creep Resistance of Aluminum Oxide," Acta Materialia, Vol. 47, Nos 15, pp 4197-4207, 1999
34. J. Bruley, J. Cho, H. M. Chan, M. P. Harmer, J. M. Rickman, "Scanning Transmission Electron Microscopy Analysis of Grain Boundaries in Creep-Resistant Yttrium- and Lanthanum- Doped Alumina Microstructures," J. Am. Ceram. Soc. 82[10] 2865-70 (1999)
35. M. A. Gülgün, V. Putlayev, M. Rühle, "Effects of Yttrium Doping α-Alumina:I, Microstructure and Microchemistry, " J. Am. Ceram. Soc. 82[7] 1849-56 (1999)
36. R. Voytovych, I. MacLaren, M. A. Gülgün, R. M. Cannon, M. Rühle, "The effect of Yttrium on Densification and Grain Growth in α-Alumina, " in press
37. H. Yoshida, Y. Ikuhara, T.Sakuma, "High Temperature Creep Resistance in Rare-Earth Doped, Fine Grained Al_2O_3," Journal of. Material Research, 13, 2597 (1998)
38. H. Yoshida, Y. Ikuhara, T.Sakuma, "Transient Creep in Fine Grained Polycrystalline Al_2O_3 with Lu^{3+} Ion Segregation at the Grain Boundaries," Journal of. Material Research., 16, 716 (2001)

APPENDIX A

A.1. Grain Size Measurement

A.1a. Average Grain Size Measurement by Mean Linear Intercept Method

Total number of grains intersected the lines that were drawn randomly on the given micrograph are 200 (Figure A.1a.1.). Each line is 26.8 cm and totally there are 7 lines. Therefore;

$26.8 \times 7 = 187.6$ cm total length of the lines
$187.6 / 200 = 0.938$ cm/cut

From the SEM micrograph:

5 microns = 4.2 cm

Then;

$\overline{L} = 0.938 \times (5 / 4.2) = 1.12$ microns

Grain size = $\overline{L} \times 1.5 = 1.68$ microns

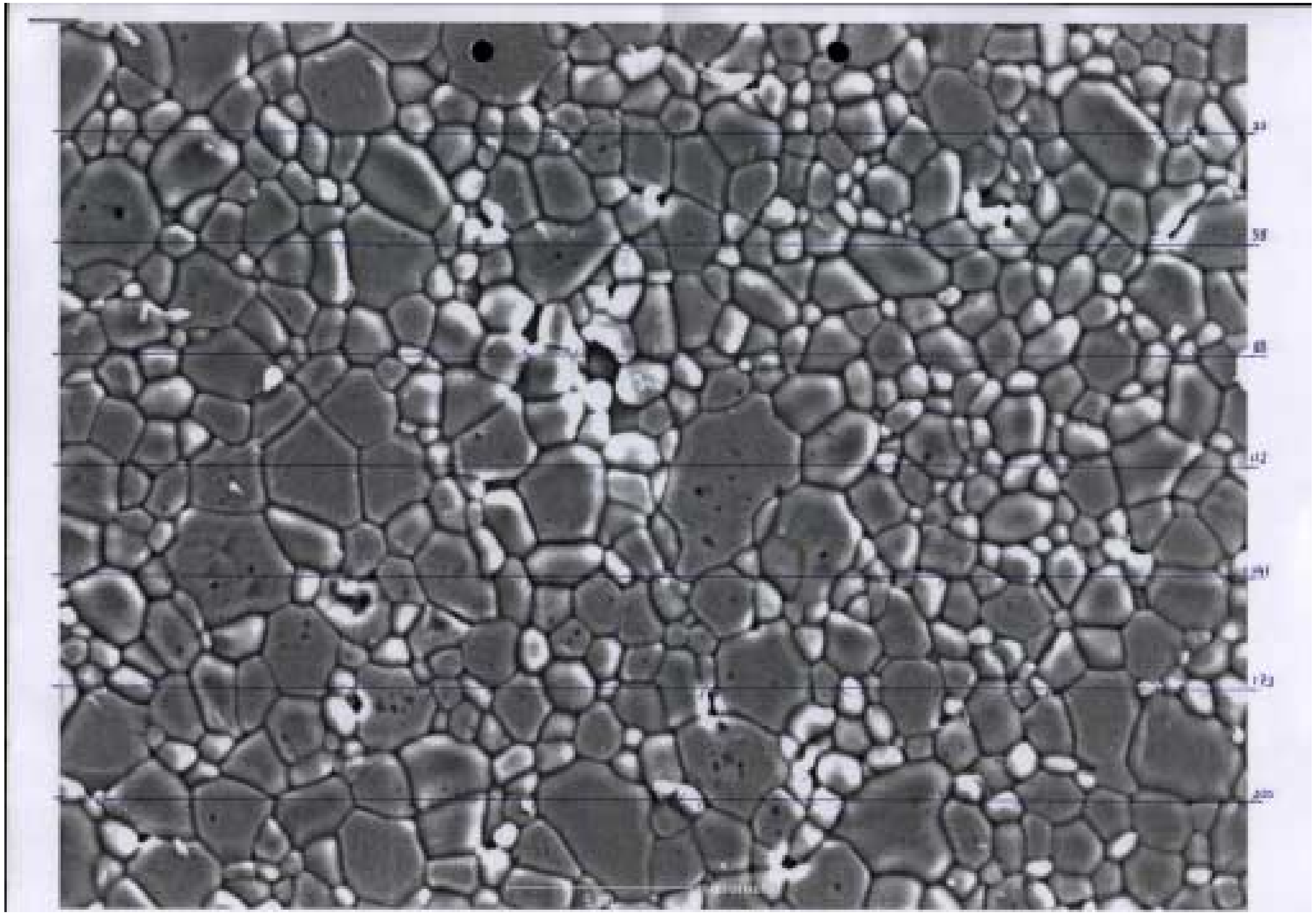

Figure A.1a.1. Measurement of the average grain size of 60 ppm Ca doped sample sintered at 1500^0C for 12 hours

A.1b. Average Grain Size Measurement of Small and Large Grains

The average grain size of small grains was calculated by mean linear intercept method as described in Appendix A.1a. From the Figure A.1b.1. total number of small grains intersected the lines that were drawn randomly on the given micrograph are 364. Total length of the lines is 303.7 cm. Therefore;

303.7 / 364 = 0.834 cm / cut

From the SEM micrograph:

5 microns = 4.2 cm

Then;

$\overline{L}_{\text{small grains}} = 0.834 \times (5 / 4.2) = 0.99$ microns

Average grain size$_{\text{small grains}}$ = $\overline{L} \times 1.5 = 1.49$ microns

The grain sizes of large grains were measured one by one and the arithmetic average was taken. Always the largest dimension of the anisotropic grains was taken as the grain size of large grains. As can be seen in Figure A.1b.1., there are 16 large grains and the total grain size of these grains is 93.9 cm. Therefore;

93.9 / 16 =5.87 cm / large grain

From the SEM micrograph:

5 microns = 4.2 cm

Average grain size$_{\text{large grains}}$ = $5.87 \times (5 / 4.2) = 6.99$ microns

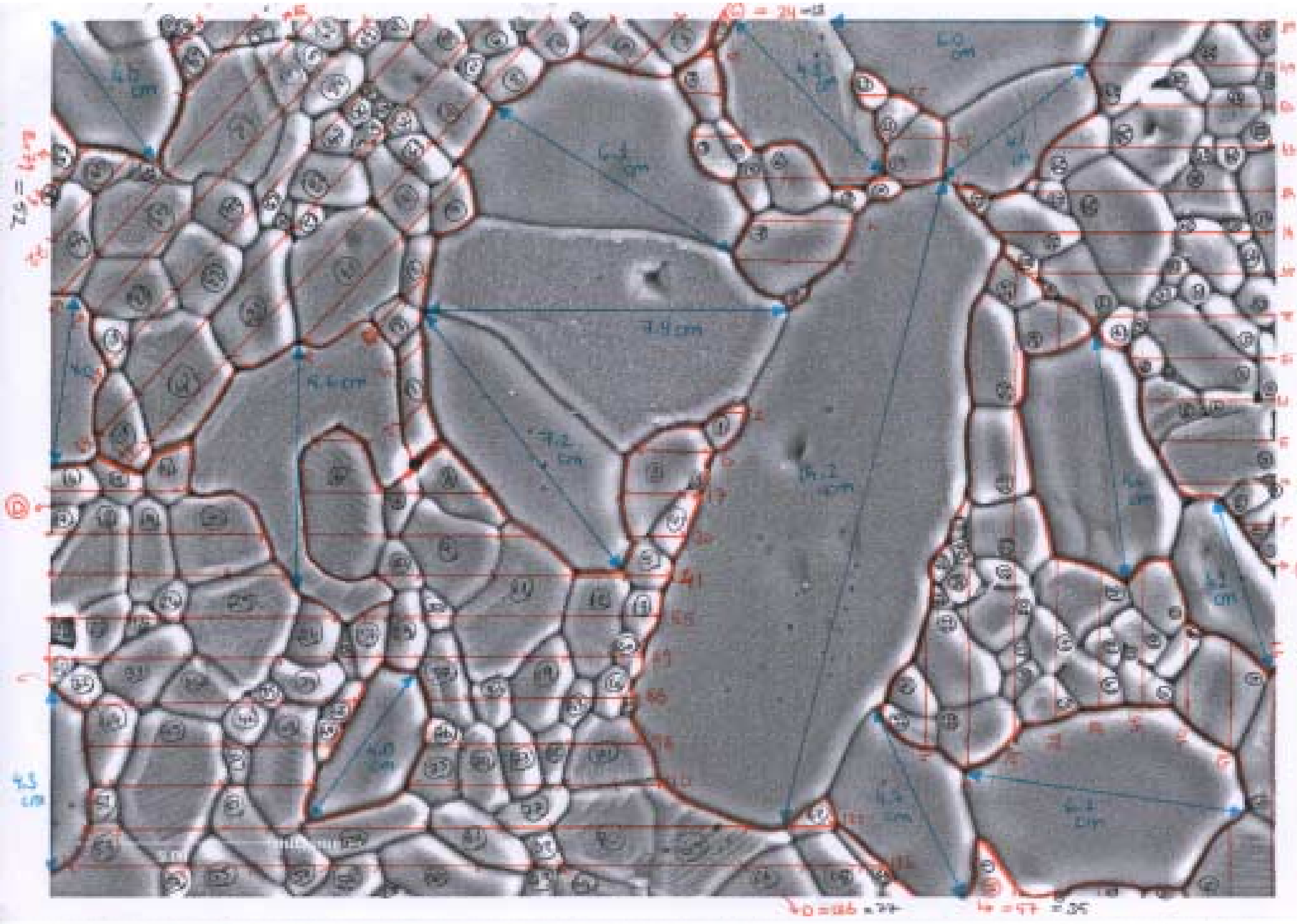

Figure A.1b.1. Measurement of the average grain sizes of small and large grains in 133 ppm Ca doped sample sintered at 1500^0C for 12 hours

A.2. Density Measurement

The size, shape, distribution, and amount of the total porosity can be determined from the microstructure. The total porosity can also be measured by determining the apparent density $\rho_{apparent}$ of a sample (total weight/total volume, including pores) and comparing this with the true density ρ_{true} (total weight/volume of solids).

The true density can be determined readily for a single-phase material but not so easily for a polyphase material. For a crystalline solid the density can be calculated from the crystal structure and lattice constant, since the atomic weight for each constituent is known. True density can also be determined by comparing pore free samples with a liquid of a known density. For glasses and single crystals this can be done by weighing the material in air and then suspended in a liquid, determining the volume by Archimedes' method; it can be done more precisely by adjusting the composition or temperature of a liquid column just to balance the density of the solid so that it neither sinks nor rises but remains suspended in the liquid. For complex mixtures and porous solids the sample must be pulverized until there are no residual closed pores and the density is then determined by the pycnometer method. The sample is put in a known-volume pycnometer bottle and weighed; then the liquid is added to give a known volume of liquid plus solid and another weight is taken. To ensure penetration of the solid among all particles, the sample and liquid should be boiled or heated under vacuum. The differences in weights obtained give the liquid volume to give the solid sample volume from which the density can be calculated.

The apparent density of porous bodies requires determination of the total volume of solid plus pores. For samples such as bricks this can be done by measuring the sample dimensions and calculating the volume. For smaller samples apparent density can be determined by measuring the weight of mercury (or of any other non-wetting liquid that does not penetrate the pores) displaced by the sample with a mercury volumeter, or the force required to submerge the sample (Archimedes' method). For small samples apparent density can also be determined by coating the sample with an impermeable film such as paraffin. The weight of the film is measured by difference so that the film volume is known. Then the volume of the sample plus film can be determined by Archimedes' method and the sample volume measured by difference. The total porosity can be determined at the same time the open-pore volume is measured by first weighing a sample in air W_a and then heating in boiling water for 2 hr to fill the open pores completely with water. After cooling, the weight of the saturated piece is determined (1) suspended in water W_{sus} and (2) in air W_{sat}. The difference between these last two values gives the sample volume and allows calculation of the apparent density. The difference between saturated and dry weights gives the open-pore volume [5].

The densities of the samples were measured by Archimedes' method. Distilled water at 21^0C was used as the wetting liquid. The weights of the compacts were measured first in air then in distilled water and the densities were calculated according to the following formula:

$$\rho_{\text{apparent}} = \frac{\text{mass}_{\text{air}} \times \rho_{\text{ water}}}{\text{mass}_{\text{air}} - \text{mass}_{\text{water}}} \qquad \text{(A.2.1)}$$

then the %theoretical densities (%TD) were found

$$\%\text{TD} = \frac{\rho_{\text{true}} - \rho_{\text{apparent}}}{\rho_{\text{true}}} * 100 \qquad \text{(A.2.2)}$$

APPENDIX B

B.1. Micrographs of the different calcium doped α-Al_2O_3 samples sintered at 1400^0C for 1 hour

a)

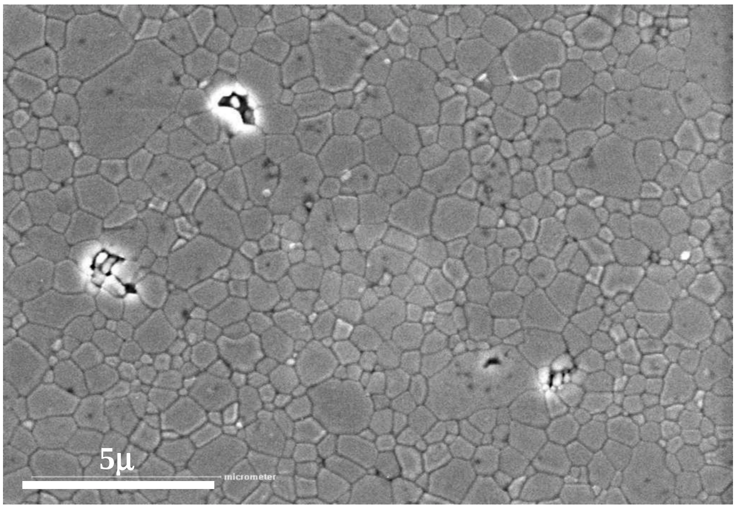

b)

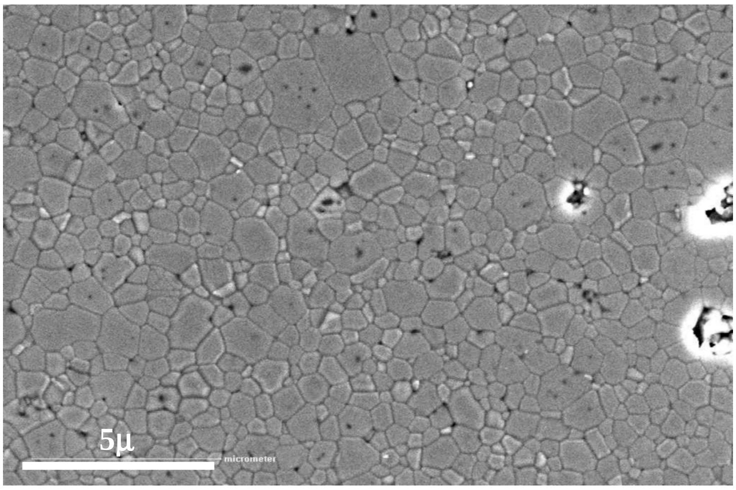

Figure B.1.1. a) Undoped α-Al_2O_3 b) 7.1 ppm Ca doped α-Al_2O_3

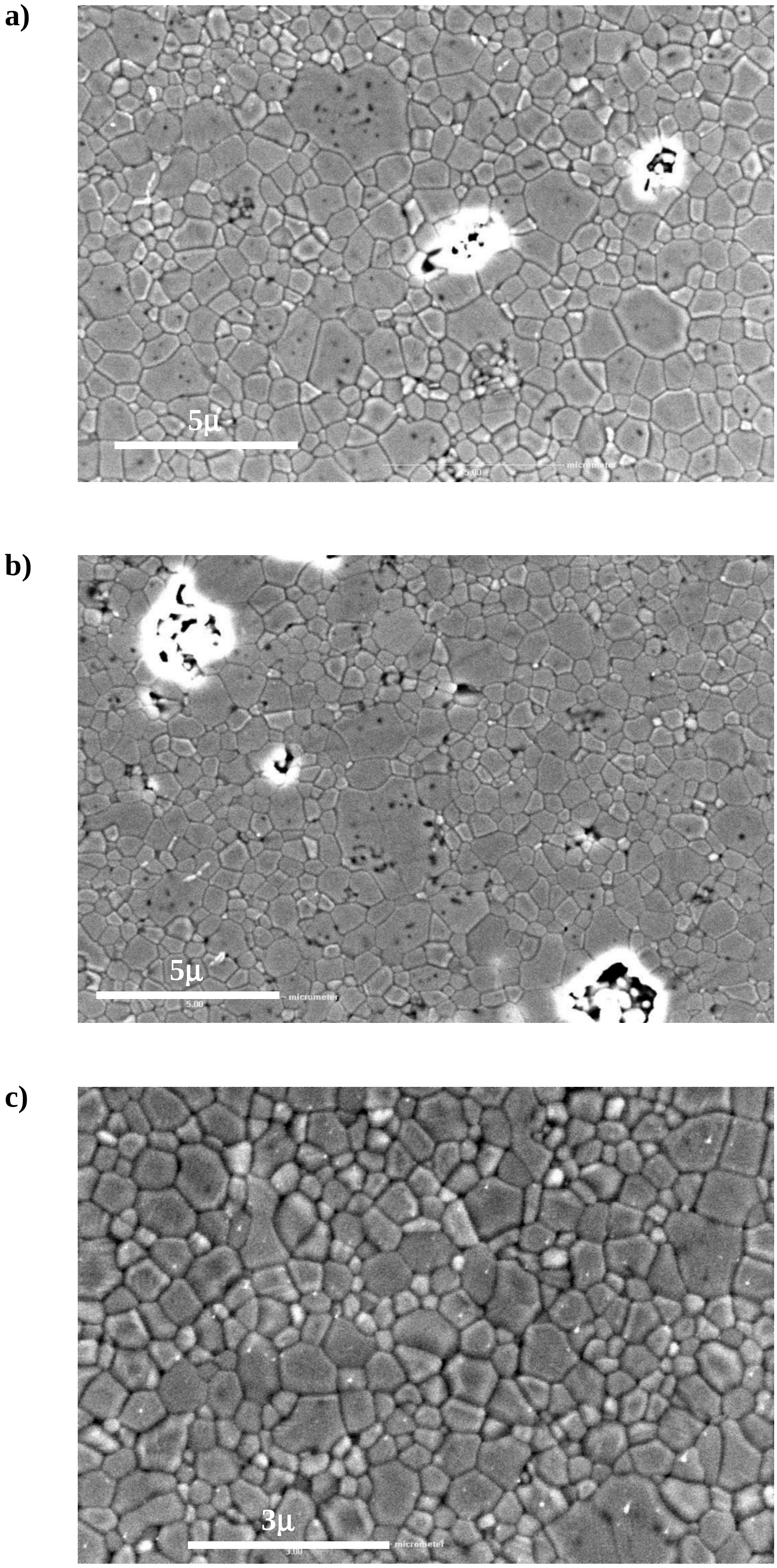

Figure B.1.2. a) 10.8 ppm Ca doped α-Al_2O_3 b) 23 ppm Ca doped α-Al_2O_3 c) 60 ppm Ca doped α-Al_2O_3

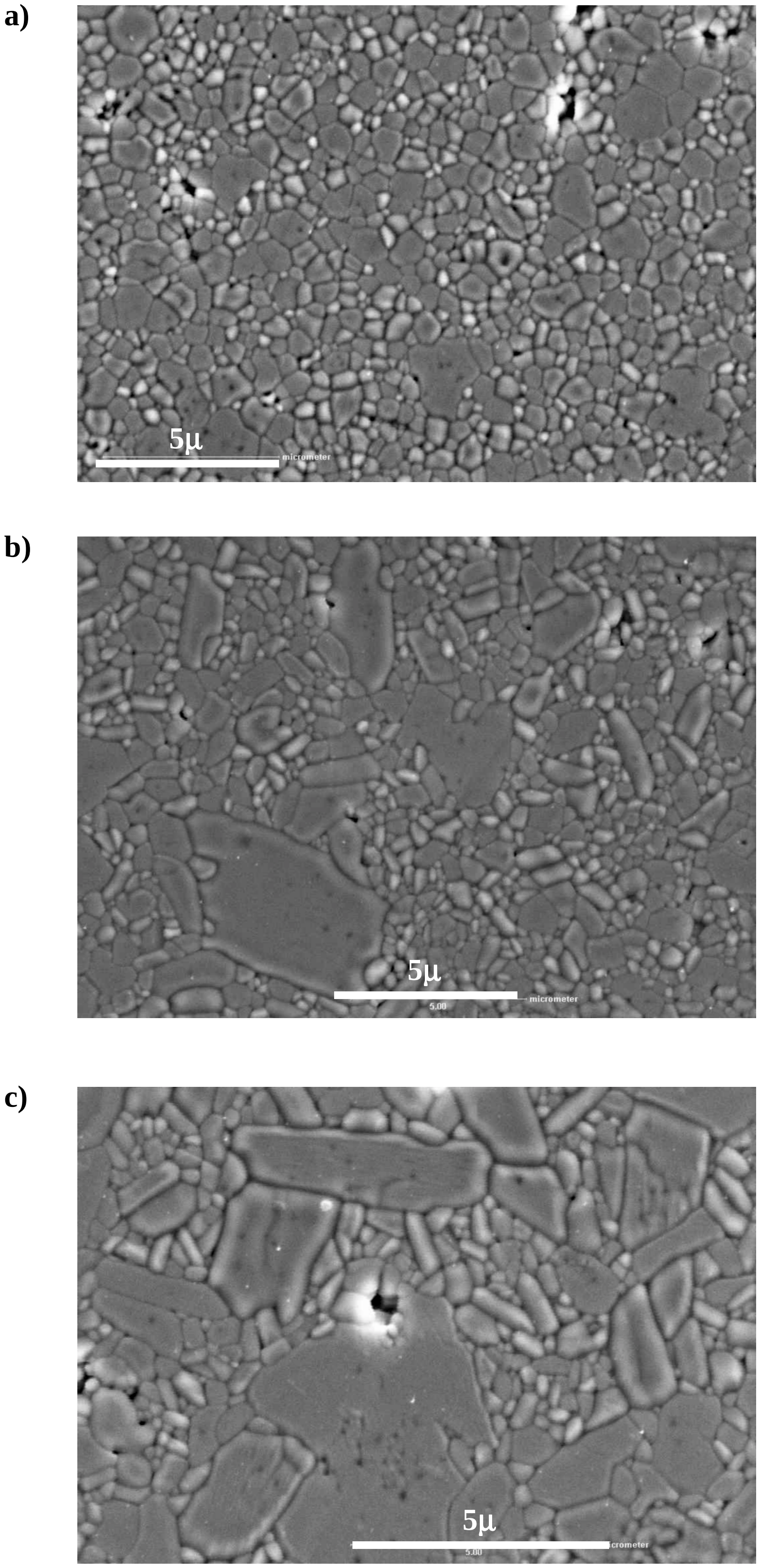

Figure B.1.3. a) 133 ppm Ca doped α-Al_2O_3 b) 344 ppm Ca doped α-Al_2O_3 c) 650 ppm Ca doped α-Al_2O_3

B.2. Micrographs of the different calcium doped α-Al_2O_3 samples sintered at 1500^0C for 1 hour

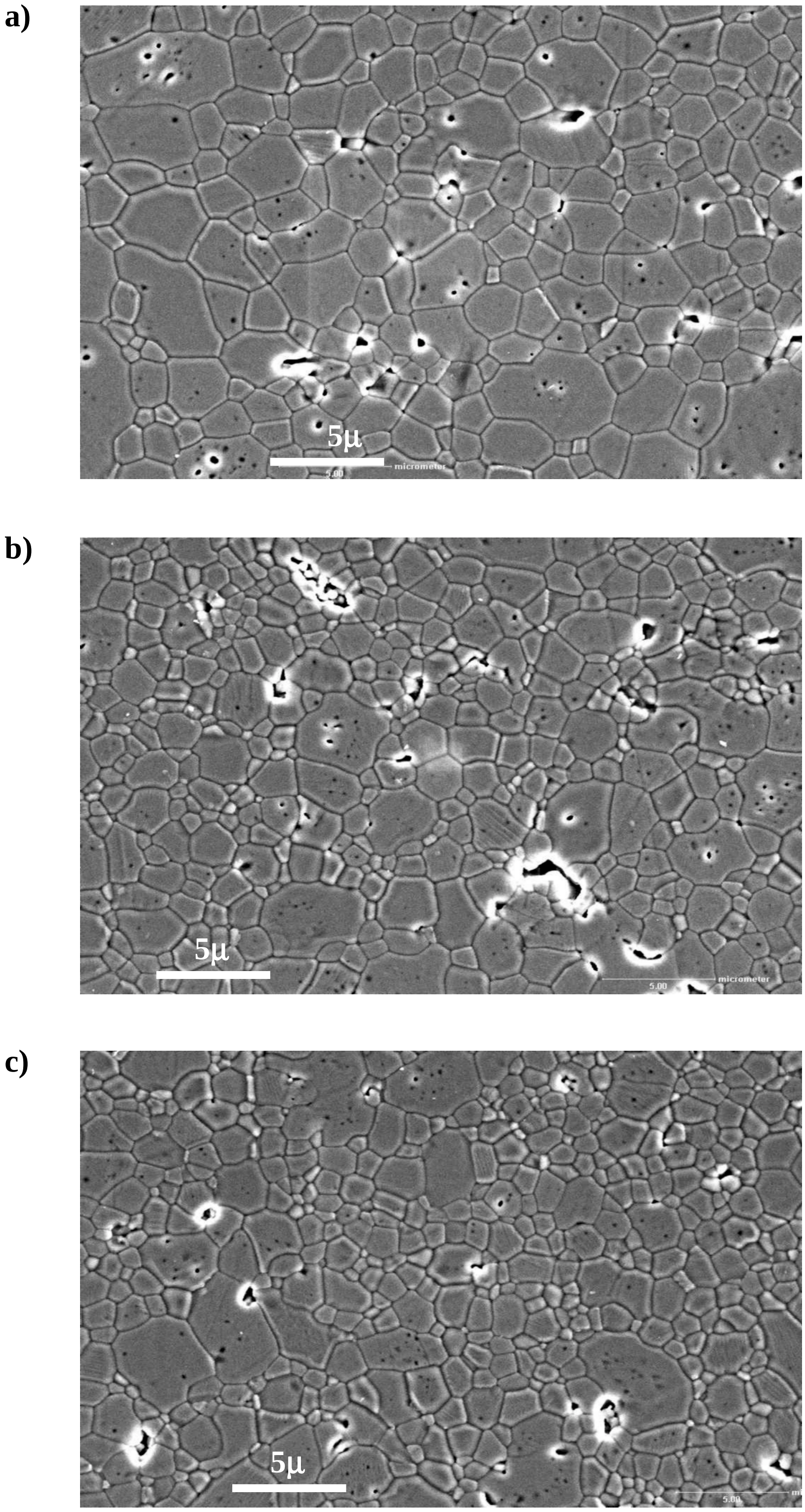

Figure B.2.1. a) Undoped α-Al_2O_3 b) 7.1 ppm Ca doped α-Al_2O_3

c) 10.8 ppm Ca doped α-Al_2O_3

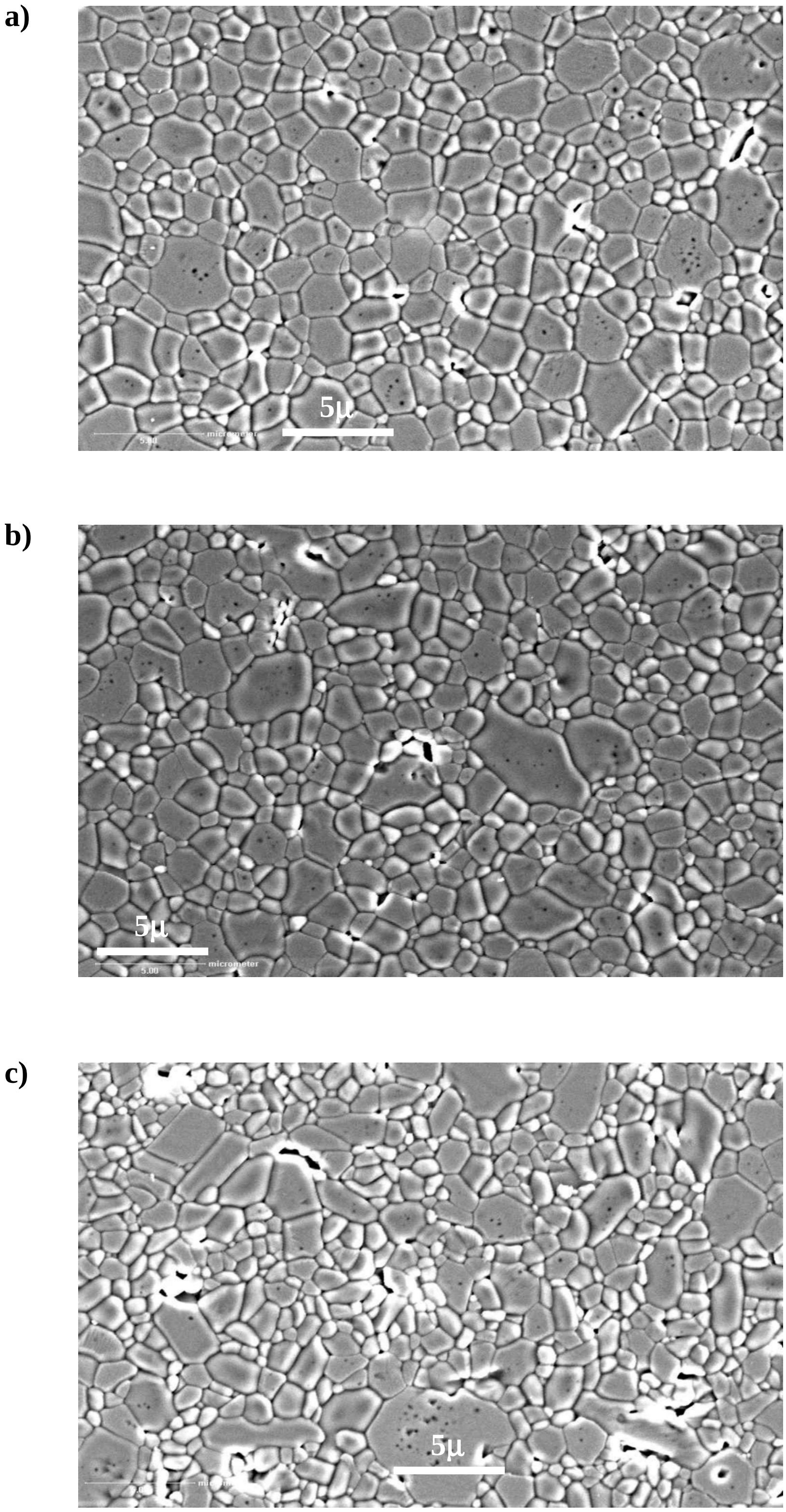

Figure B.2.2. a) 23 ppm Ca doped α-Al_2O_3 b) 60 ppm Ca doped α-Al_2O_3 c) 133 ppm Ca doped α-Al_2O_3

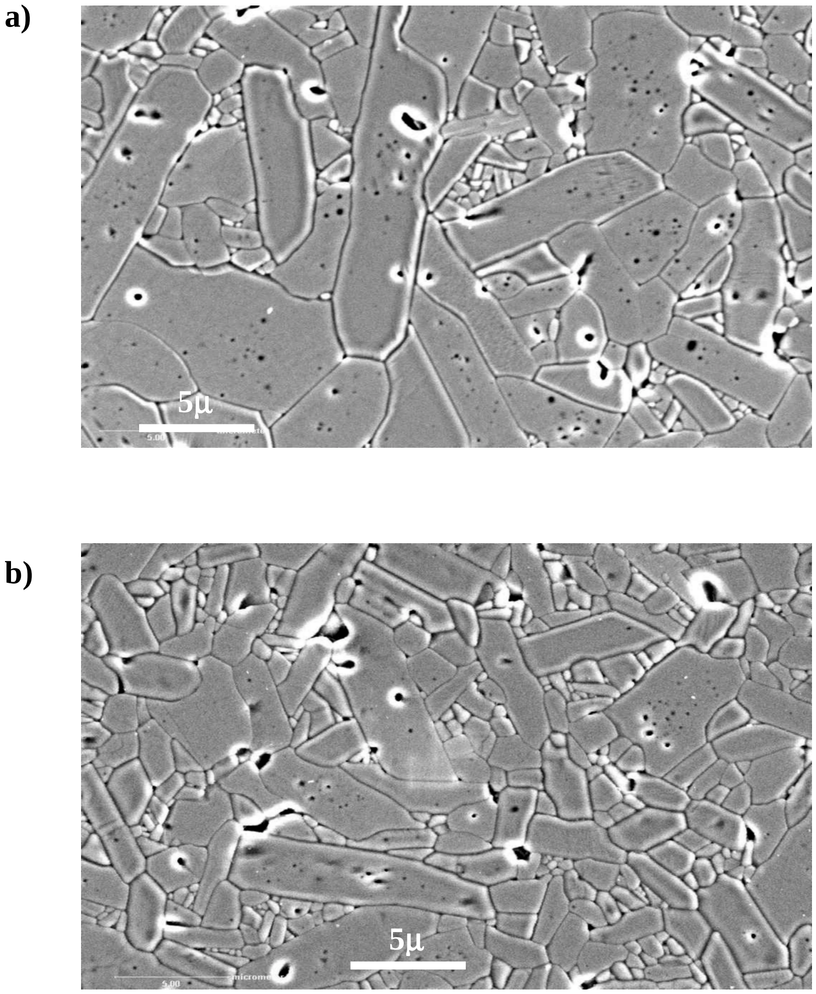

Figure B.2.3. a) 344 ppm Ca doped α-Al_2O_3 b) 650 ppm Ca doped α-Al_2O_3

B.3. Micrographs of the different calcium doped α-Al_2O_3 samples sintered at 1500^0C for 12 hours

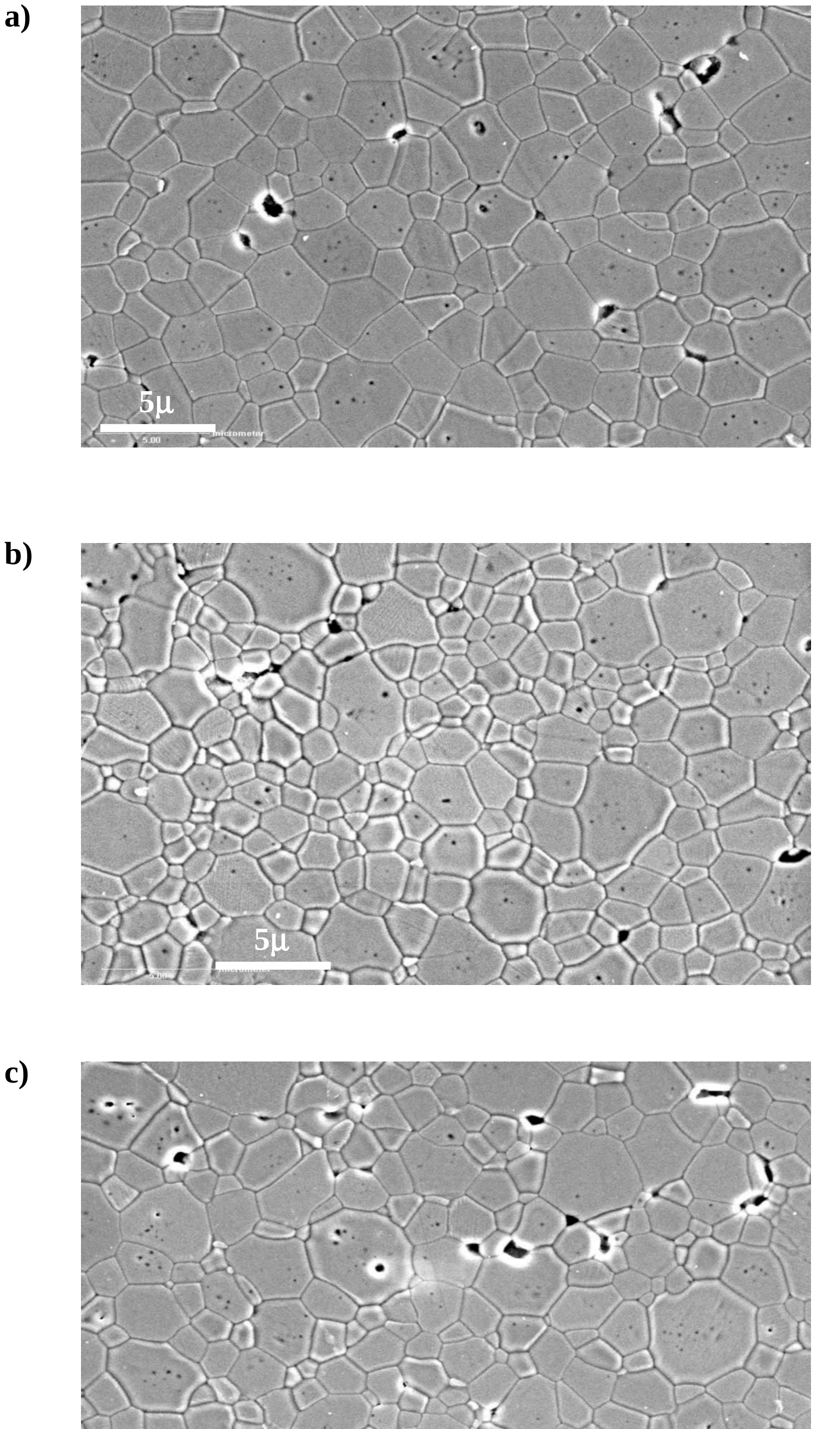

Figure B.3.1. a) Undoped α-Al_2O_3 b) 7.1 ppm Ca doped α-Al_2O_3 c) 10.8 ppm Ca doped α-Al_2O_3

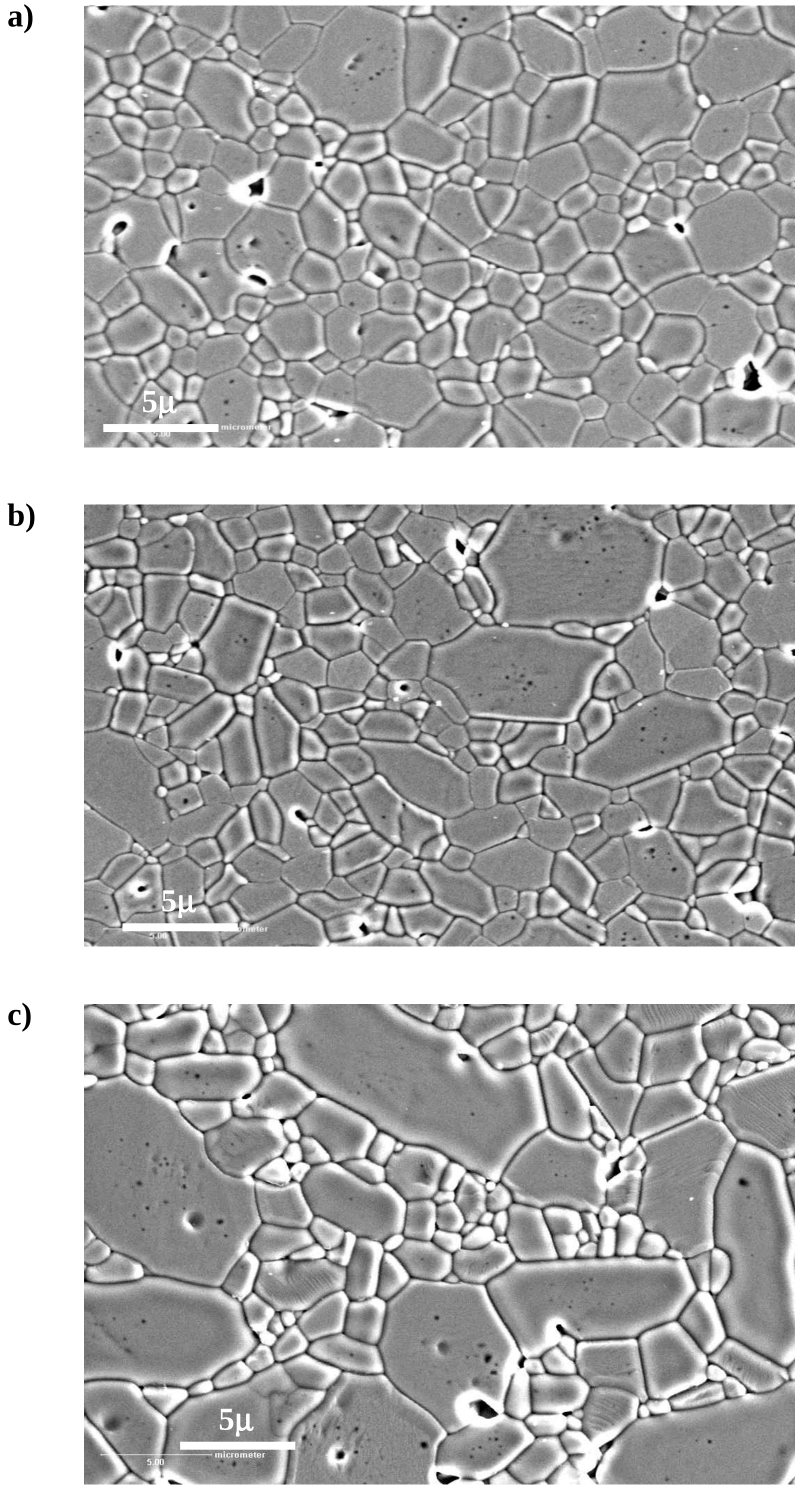

Figure B.3.2. a) 23 ppm Ca doped α-Al_2O_3 b) 60 ppm Ca doped α-Al_2O_3 c) 133 ppm Ca doped α-Al_2O_3

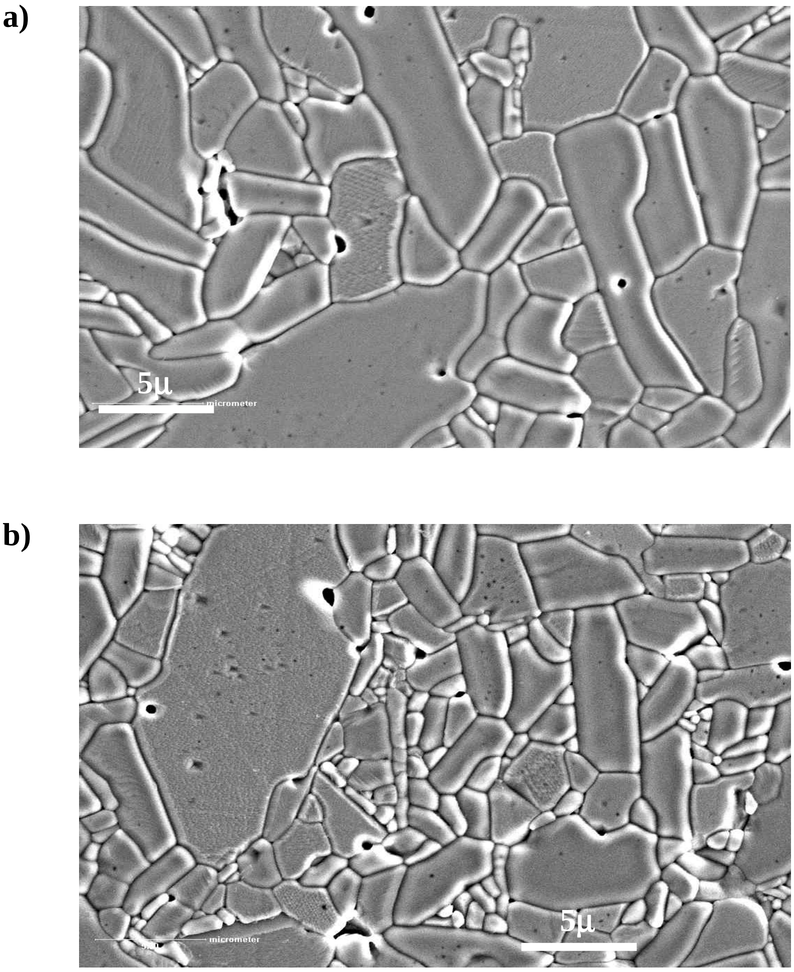

Figure B.3.3. a) 344 ppm Ca doped α-Al_2O_3 b) 650 ppm Ca doped α-Al_2O_3

B.4. Micrographs of the different calcium doped α-Al_2O_3 samples sintered at 1600^0C for 1 hour

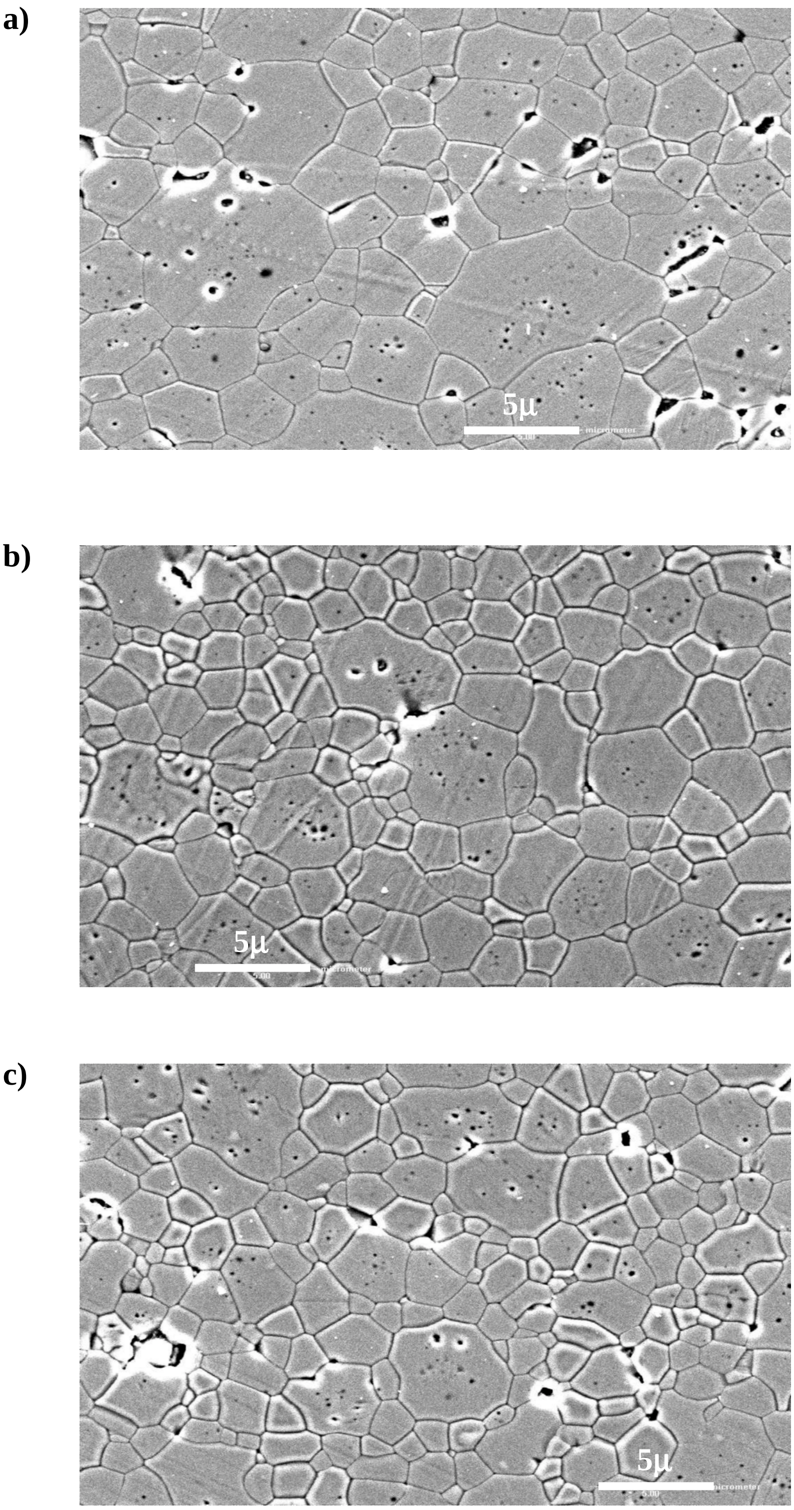

Figure B.4.1. a) Undoped α-Al_2O_3 b) 7.1 ppm Ca doped α-Al_2O_3 c) 10.8 ppm Ca doped α-Al_2O_3

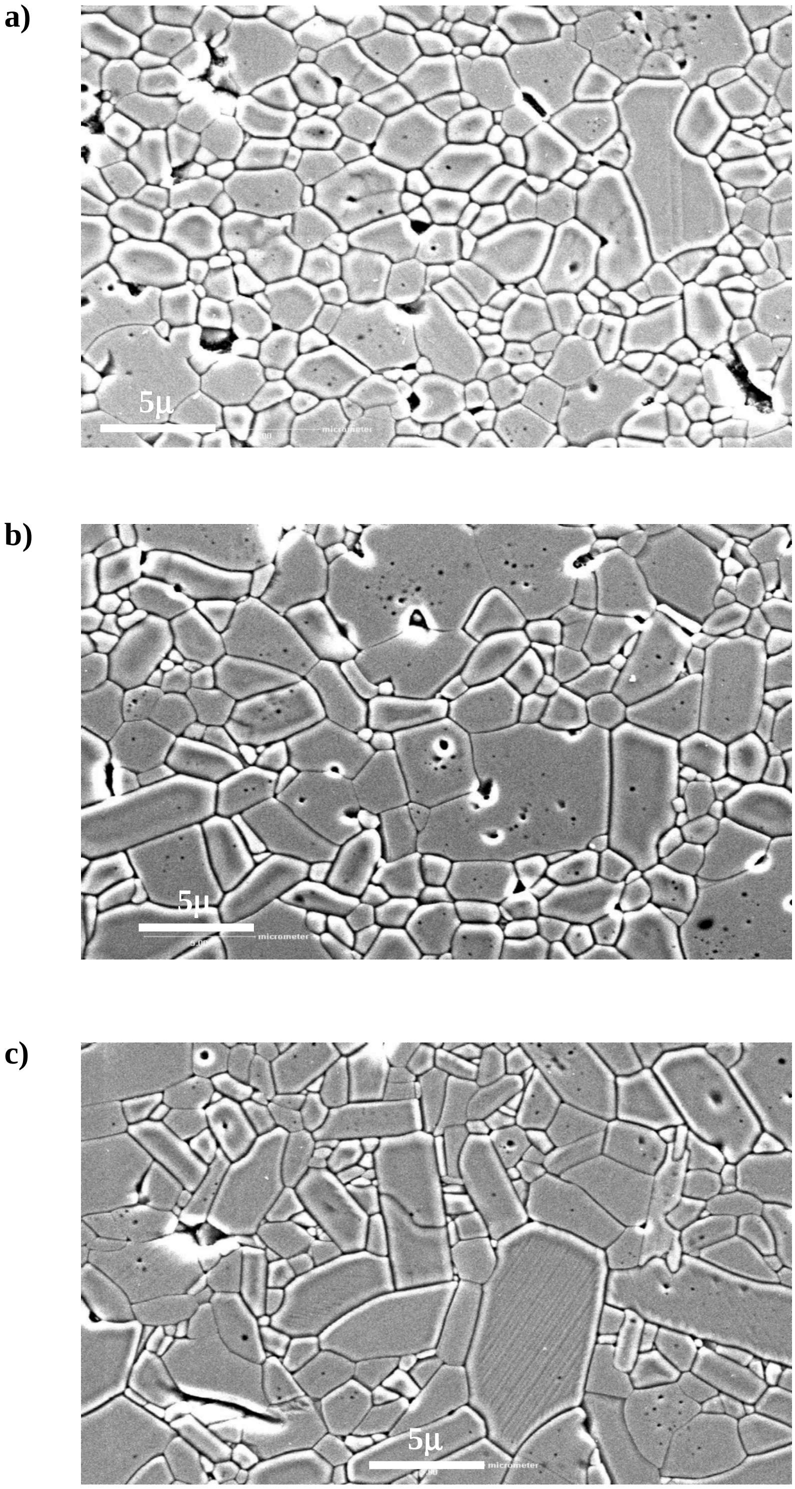

Figure B.4.2. a) 23 ppm Ca doped α-Al_2O_3 b) 60 ppm Ca doped α-Al_2O_3 c) 133 ppm Ca doped α-Al_2O_3

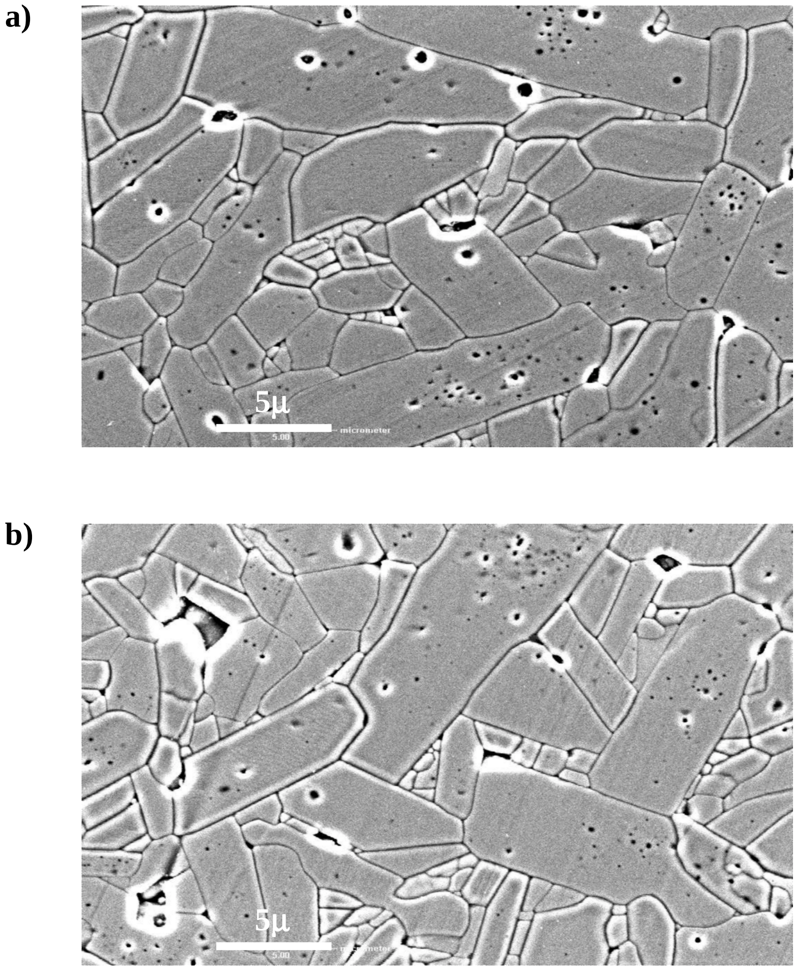

Figure B.4.3. a) 344 ppm Ca doped α-Al_2O_3 b) 650 ppm Ca doped α-Al_2O_3